University of Cyprus

Department of Physics

Optical Properties of
Multinary Chalcogenide Semiconductor Nanostructures
for Light Emission and Light Harvesting Applications

DOCTOR OF PHILOSOPHY DISSERTATION

Anna M. Zacharia

2020

University
of Cyprus

Department of Physics

Optical Properties of
Multinary Chalcogenide Semiconductor Nanostructures
for Light Emission and Light Harvesting Applications

Anna M. Zacharia

A dissertation submitted to the University of Cyprus in partial fulfillment of the
requirements for the degree of Doctor of Philosophy

September 2020

VALIDATION PAGE

Doctoral Candidate: Anna M. Zacharia

Doctoral Thesis Title: Optical Properties of Multinary Chalcogenide Semiconductor Nanostructures for Light Emission and Light Harvesting Applications

*The present Doctoral Dissertation was submitted in partial fulfillment of the requirements for the degree of Doctor of Philosophy at the **Department of Physics** and was approved on the 1st of September 2020 by the members of the **Examination Committee.***

Examination Committee:

Research Supervisor: Itskos Grigorios. Associate Prof……………………………,......................

Committee Member: Andreas Othonos, Prof.…………………………………..……………….

Committee Member: Spiros Skourtis, Associate Prof……………………………..……………….

Committee Member: Theodora Kyratsi, Prof…………………………………………………

Committee Member: Juan Cabanillas González, Prof……………………………..………….

DECLARATION OF DOCTORAL CANDIDATE

The present doctoral dissertation was submitted in partial fulfillment of the requirements for the degree of Doctor of Physics of the University of Cyprus. It is a product of original work of my own, unless otherwise mentioned through references, notes, or any other statements.

Anna M. Zacharia

Περίληψη

Οι σύνθετοι ημιαγωγοί χαλκογονιδίων (MCS) έχουν αναδειχθεί ως ελκυστικά οπτοηλεκτρονικά υλικά, προσφέροντας ευελιξία σύνθεσης και στοιχειομετρίας, χαμηλή τοξικότητα και έντονη οπτική απορρόφηση με ενεργειακά χάσματα κατάλληλα για τη συλλογή ηλιακού φωτός. Με τη μορφή κολλοειδών κβαντικών τελειών (CQDs), οι MCS εμφανίζουν, ρυθμιζόμενη από το μέγεθος των τελειών, φωταύγεια στο ορατό έως σχεδόν υπέρυθρο, με υψηλή κβαντική απόδοση εκπομπής όταν παθητικοποιούνται με κέλυφος, καθιστώντας τις υποσχόμενες για εφαρμογές σε φωτισμό, βιο-απεικόνιση και συγκεντρωτές φωταύγειας (luminescent concentrators). Τα MCS CQDs παρουσιάζουν επίσης ενδιαφέρουσες πλασμονικές, καταλυτικές και μη γραμμικές οπτικές ιδιότητες.

Η φωτοφυσική των MCS είναι πολύπλοκη, επηρεάζεται από διακυμάνσεις της σύνθεσης, της χωρικής και ενεργιακής αταξίας και ένα ευρύ φάσμα κρυσταλλικών ατελειών. Τα πρωτότυπα συστήματα MCS όπως τα λεπτά υμένια $CuInGaS_2$ και τα $CuInS_2$ CQDs έχουν υπάρξει στο επίκεντρο εντατικών μελετών, ωστόσο πτυχές της σύνθετης ηλεκτρονικής δομής και δομής των ατελειών τους δεν είναι ακόμη πλήρως κατανοητές. Από την άλλη πλευρά, υπάρχουν άλλα υλικά της οικογένειας MCS που είναι σημαντικά λιγότερο ανεπτυγμένα και μελετημένα με πρόοδο που παρεμποδίζεται από την απαιτητική σύνθεσή τους ή/και την εξαιρετικά πλούσια σε ατέλειες φύση τους.

Με κίνητρο τέτοιες προκλήσεις, παρουσιάζουμε εδώ φασματοσκοπικές μελέτες τριών τύπων ημιαγωγών πολλαπλών χαλκογονιδίων που είναι πολλά υποσχόμενες για εφαρμογές συλλογής και εκπομπής φωτός. Δύο από τα κεφάλαια περιλαμβάνουν μελέτες σε τριμερή CQDs του συστήματος $CuInS_2$ (CIS) και AgInSe (AISe), αντίστοιχα. Το κίνητρο για μελέτη κβαντικών τελειών τέτοιων υλικών έγκειται στα ακόλουθα:

1. Η παρουσία των αποτελεσμάτων κβαντικού περιορισμού που επιτρέπει την ρύθμιση του ενεργειακού χάσματος χωρίς αλλαγή της σύνθεσης. Στη μελέτη μας, έχουν χρησιμοποιηθεί μεγέθη τελειών στην λεγόμενη περιοχή ισχυρού περιορισμού και για τα δύο συστήματα που μελετήθηκαν CQD και οι οπτικές ιδιότητες που εξαρτώνται από το μέγεθος έχουν διερευνηθεί εντός της περιοχής μεγέθους ~ 2 έως $\sim 3,5$ nm.

2. Με τη μορφή CQDs, τα υλικά ανέχονται μεγάλες αποκλίσεις της στοιχειομετρίας χωρίς μεταβατικές φάσεις. Με βάση αυτό, έχουν διερευνηθεί υψηλής ποιότητας μη στοχειομετρικά AISe CQDs.

3. Η παθητικοποίηση της επιφάνειας από ένα κέλυφος αυξάνει την κβαντική απόδοση εκπομπής σε τιμές σημαντικά υψηλότερες από τις αντίστοιχες τιμές των bulk υλικών. Στη μελέτη μας, οι CIS CQD χρησιμοποιούν ένα τέτοιο Zn-κέλυφος το οποίο παθητικοποιεί τις επιφανειακές καταστάσεις και οδηγεί σε μείωση των μη ακτινοβολούσων αποδιεγέρσεων. Μελέτες CQD πυρήνα / κελύφους μελετώνται επίσης στη σειρά δειγμάτων AISe CQD για συγκριτικές μελέτες των ιδιοτήτων φωταύγειας με τις αντίστοιχες CQD που διαθέτουν μόνο τον πυρήνα.

4. Οι CQD μπορούν εύκολα να ενσωματωθούν σε ευπροσάρμοστα και λειτουργικά μείγματα ή ετερο-διατάξεις με άλλους ημιαγωγούς επεξεργασμένους σε διάλυμα.

Επιπλέον, αξίζει να σημειωθεί ότι το μεγαλύτερο μέρος της προσπάθειας σε CQDs έχει πραγματοποιηθεί μέχρι στιγμής σε συστήματα που βασίζονται σε Cd και Pb που φαίνονται ελκυστικά για οπτικοηλεκτρονικές και φωτονικές εφαρμογές αλλά περιέχουν τα βαρέα μέταλλα Cd και Pb. Από την άλλη πλευρά, τα προαναφερθέντα δύο υλικά CQD που μελετήθηκαν περιέχουν σημαντικά λιγότερο τοξικά στοιχεία που δεν επιβάλλουν όρια στην πιθανή εμπορική τους χρήση.

Η διατριβή ολοκληρώνεται με μια τρίτη μελέτη σε υλικά MCS, που σχετίζεται με φασματοσκοπικές μελέτες λεπτών υμενίων $CuIn_{0.7}Ga_{0.3}Se_2$ (CIGS). Τα λεπτά υμένια CIGS έχουν προσελκύσει μεγάλο ενδιαφέρον λόγω της χρήσης τους σε αποδοτικά ηλιακά κύτταρα λεπτών υμενίων. Η καινοτομία της μελέτης είναι ότι τα υμένια δεν παράχθηκαν μέσω των τυπικών μεθόδων εξάτμισης (evaporation) ή διασκόρπισης (sputtering), αλλά εναποτέθηκαν μέσω εναπόθεσης παλμικού λέιζερ (Pulsed Laser Deposition, PLD), μιας καθιερωμένης αλλά σπάνια χρησιμοποιούμενης μεθόδου ανάπτυξης στη βιβλιογραφία για το CIGS. Ακόμη λιγότερα είναι γνωστά για τις οπτικές ιδιότητες των CIGS που παράγονται με PLD και για την σύγκρισή τους με τις ιδιότητες των καλά μελετημένων CIGS υμενίων που εναποτίθενται μέσω εξάτμισης ή διασκόρπισης. Με κίνητρο αυτό, πραγματοποιήσαμε μια διεξοδική φασματοσκοπική έρευνα υμενίων CIGS που έχουν αναπτυχθεί με PLD, διερευνώντας την επίδραση της θερμοκρασίας εναπόθεσης για να αναλύσουμε την συνεισφορά ηλεκτρονικών και σταθμών και καταστάσεων ατελειών στην φωταύγειά τους. Η μελέτη ολοκληρώνεται με

φασμαοσκοπία υμενίων CdS που έχουν αναπτυχθεί με PLD με σκοπό την αξιολόγηση της προοπτικής πλήρως αναπτυγμένων δομών ηλιακών κυττάρων με PLD.

Abstract

Multinary chalcogenide semiconductors (MCS) have emerged as attractive optoelectronic materials, offering versatility of composition and stoichiometry, low toxicity and intense optical absorption with energy gaps suitable for solar light harvesting. In the form of colloidal quantum dots (CQDs), MCS exhibit tunable, size-dependent luminescence in the visible to near-infrared, with high emission quantum yield when passivated with protective shells making them promising for lighting, bio-imaging and luminescent concentrators; MCS CQDs exhibit also interesting plasmonic, catalytic and non-linear optical properties.

The photophysics of MCS alloys is complex, being affected by compositional fluctuations, spatial and energetic disorder and a wide range of defects. Prototype MCS systems such as $CuInGaS_2$ thin films and $CuInS_2$ CQDs have been the focus of intense studies, however aspects of their complex electronic and defect structure are still not fully understood. On the other hand, there are other materials of the MCS family that are significantly less developed and studied with progress hindered by their demanding synthesis and/or their highly defected nature.

Motivated by such challenges, we present herein spectroscopic studies of three types of multinary chalcogenide semiconductors that are promising for light harvesting and light emission applications. Two of the projects involve work on ternary CQDs of the $CuInS_2$ (CIS) and AgInSe (AISe) system, respectively. The motivation to study QDs of such materials lies on the following:

1. The presence of quantum confinement effects, increasing the exciton oscillator strength and allowing tuning of the energy gap without variation of the composition. In our study, dot sizes in the so-called strong confinement regime have been employed for both CQD studied systems and the size-dependent optical properties have been investigated within the ~2 to ~3.5 nm range.

2. In the form of CQDs, the materials tolerate broad deviations of the stoichiometry without structural phase transitions. Based on this, high quality non-stochiometric AISe CQDs have been investigated.

3. Surface passivation by a shell increases the emission quantum yield to values significant higher than the respective values of the bulk material analogues. In our study, the CIS CQDs

employ such a passivating Zn-shell to quench surface in favor of radiative recombination. Core/shell CQDs are also studied in the AISe CQD samples series for comparative studies against the luminescent properties of core only analogues.

4. CQDs can be easily integrated in versatile and functional assemblies or heterojunctions with other solution-processed semiconductors.

As an additional motivation, it is worth mentioning that most of the effort in CQDs has been performed thus far in Cd- and Pb-based systems that appear highly attractive for optoelectronic and photonic applications but contain the heavy metals Cd and Pb. On the other hand, the aforementioned two CQD materials studied contain significant less toxic elements that do not impose limits in their potential commercial use.

The thesis is completed by a third project on MCS, associated with spectroscopic studies of $CuIn_{0.7}Ga_{0.3}Se_2$ (CIGS) polycrystalline thin films. CIGS thin films have attracted considerable attention due to their proven potential as active region absorbers for efficient thin film solar cells. The novelty of the project is that the studied films were not produced via the standard evaporation or sputtering methods but instead they were deposited via pulsed laser deposition (PLD), an established but rarely used method in the literature for CIGS. Even less is currently known for the optical properties of PLD-grown CIGS and how they compare with the respected properties of the well-studied evaporated or sputtered films. Motivated by this, we have carried out a thorough spectroscopic investigation of PLD-grown CIGS films, probing the influence of deposition temperature to unravel the electronic and defect contributions in the films luminescence. The study is concluded by spectroscopic studies of PLD-grown CdS with a view of evaluating the prospect of fully PLD-grown solar cell structures.

Acknowledgments

First and foremost I want to thank my supervisor, Prof. Grigorios Itskos, for the patient guidance, encouragement and advice he has provided throughout my time as his student. He has taught me, both consciously and unconsciously, how good experimental physics is done. I appreciate all his contributions of time and ideas to make my Ph.D. experience productive and stimulating. The joy and enthusiasm he has for his research was contagious and motivational for me, even during tough times in the Ph.D. pursuit. I have been extremely lucky to have a supervisor who cared so much about my work. His advice on both research as well as on my career have been invaluable.

Besides my advisor, I would like to thank the rest of my dissertation committee members for their great support and invaluable advice. Thank you for investing time and providing interesting and valuable feedback. I feel proud and honoured that you have accepted to be on my committee.

Special thanks should also be given to Dr. Paris Papagiorgis for his valuable guidance and consistent encouragement I received throughout the research work.

Prof. Gerasimos Konstantatos at ICFO, Institute of Photonic Sciences, Barcelona for providing the high quality CIS quantum dot material without which interesting work in this project would not have been achieved. I would also like to thank Ph.D student Christiana Nicolaou and Prof. Ioannis Giapitzakis at Department of Mechanical Engineering of the University of Cyprus for the perfect collaboration and the provision of CIGS samples. My sincere thanks also goes to the group of Dr. Maksym Yarema at ETH Zurich for our effective, inspiring and pleasant collaboration and for providing the AgInSe material.

I also want to thank all of my friends who supported me, and incented me to strive towards my goal. A special thanks to my parents, brother, sister and grandparents for believing in me and being there for practical support in all those things of life beyond doing a PhD. Words can not express how grateful I am to my mother, and father for all of the sacrifices that you've made on my behalf.

This thesis is dedicated to my parents.

For their endless love, support and encouragement.

Published work related to the thesis

1. «Probing the Origin of Absorbing and Luminescent Species in Silver Indium Selenide Nanocrystals», **A. Zacharia**, O. Yarema, P. Papagiorgis, A. Moser, A. Othonos, M. Yarema, V. Wood, G. Itskos, in preparation, estimated submission September 2020

2. «Luminescence properties of pulsed laser deposited $CuIn_xGa_{1-x}Se_2$ films», **A. Zacharia**, C. Nicolaou, J. Giapintzakis, G. Itskos, J. Phys. Commun., 2020, 4, 045001

3. «Single-step growth of high quality CIGS/CdS heterojunctions using Pulsed Laser Deposition», C. Nicolaou, **A. Zacharia**, A. Delimitis, G. Itskos, J. Giapintzakis, Applied Surface Science, 2020, 511, 145547

4. «Influence of Process Parameters on the Properties of Pulsed Laser Deposited $CuIn_{0.7}Ga_{0.3}Se_2$ Thin Films», C. Nicolaou, **A. Zacharia**, G. Itskos, J. Giapintzakis, Solar Energy, 2018, 174, 793-802

Published work related to other characterization studies

1. «Dual Emission in a Ligand and Metal Co-Doped Lanthanide-Organic Framework: Color Tuning and Temperature Dependent Luminescence», D. Andriotou, S. A. Diamantis, **A. Zacharia**, G. Itskos, N. Panagiotou, A. J. Tasiopoulos, T. Lazarides, Molecules 2020, 25, 523

2. «Temperature-dependent Interchromophoric Interaction in a Fluorescent Pyrene-based Metal–organic Framework», A. Gładysiak, Tu N. Nguyen, R. Bounds, **A. Zacharia**, G. Itskos, J. A. Reimer, K. Stylianou, Chem. Sci., 2019, 10, 6140

3. «Selective, Fast-response and Regenerable Metal–organic Framework for Sampling Excess Fluoride Levels in Drinking Water», F.Ebrahim, T.N Nguyen, S. Shyshkanov, A. Gładysiak, P. Favre, **A. Zacharia**, G. Itskos, P. Dyson, K. Stylianou, JACS, 2019, 141, 3052-3058

Table of Contents

List of Figures

List of Tables

Acronyms

CQDs	Semiconductor colloidal quantum dots
EMA	Effective mass approximation
CNCs	Colloidal semiconductor nanocrystals
PLD	Pulsed laser deposition
O. D	Optical density
PMT	Photomultiplier tube
PL	Photoluminescence
PLE	Excitation photoluminescence
Cw	Continuous wave
TR-PL	Time-resolved PL
TCSPC	Time correlated single photon counting
TRES	Time-resolved emission spectra
OPA	Optical Parametric Amplifier
CIS	Copper indium sulfide
CP	Chalcopyrite
HW	Hexagonal wurtzite
ZB	Zinc blende
DAP	Donor-to-acceptor
CB	Conduction Band
VB	Valence Band
XPS	X-Ray photoemission
CIGS	Copper indium gallium (di) selenide
Mo	Molybdenum
AZO	Al-doped ZnO
SLG	Soda-lime glass
GIXRD	Grazing incidence X-ray diffraction
Eg	Energy gap
FWHM	Full with half maximum
NC	Nanocrystal
AISe	Silver indium selenide
QY	Quantum yield

HRTEM	High-resolution Transmission electron microscopy
RW	Relative Weight
PIA	Photo-induced absorption

1   Theoretical Background

1.1   Semiconductor colloidal quantum dots (CQDs)

Quantum dots are tiny nanocrystals of a semiconducting material with a typical diameter of 2-10 nm. QDs have unique electronic properties, due to their high surface-to-volume ratios and their small size that result in new quantum phenomena. A characteristic such quantum dot property is that their energy levels are strongly dependent on the structure's size, a phenomenon known as quantum confinement. For example, CdSe quantum dot light absorption/emission can be tuned from red (~5 nm diameter) to the violet region (~1.5 nm diameter) via the size-dependent energy levels of the dots. Therefore, quantum dots can absorb or emit in a wide spectral range using the same material composition, by simply varying the dot size. [1] The quantum dot can typically be composed of three main parts: core, shell, and ligands. The semiconductor core is coated by ligand molecules, while in certain occasions a shell is grown to provide spatial separation between the surface and the core states. [2]
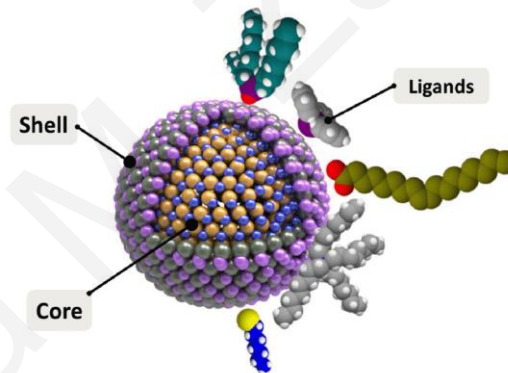
Figure 1.1 Typical structure of a quantum dot showing its three main features: core, shell and ligands. [3]

Quantum dots are promising for optical applications due to the high absorption, the inexpensive and simple construction and the efficient light emission throughout the visible and near-infrared. Varying the size of quantum dots provides a facile method to tune the optical bandgap and the electronic density of states **(Figure 1.2).** All of the above makes semiconductor quantum dots highly promising for lighting, display, bio-imaging and other photonic applications such as photodetectors and solar cells. CQDs exhibit also interesting plasmonic, catalytic and non-linear optical properties. *[2]*
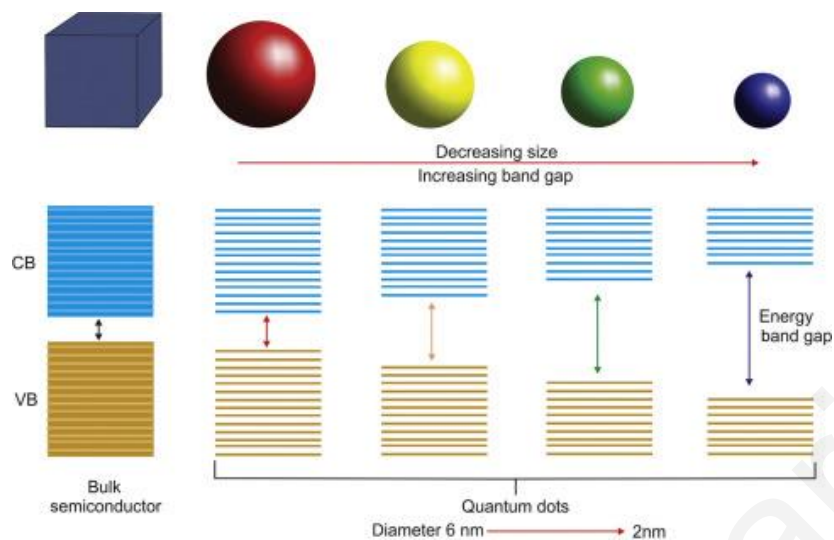
Figure 1.2 The influence of particle size on the band gap and photoluminescence emission wavelength of quantum dots [4]

1.1.1 Synthesis

CQDs are synthesized from solutions, much like traditional chemical processes, by chemical reactions of appropriate molecular precursors. Synthesis is typically achieved with the hot-injection technique, where the precursors are rapidly injected into a hot solvent with subsequent temperature drop. [5] [6] Heating the solution at high temperature, results in decomposition of the precursors, that form monomers which then nucleate and produce seeds. The colloidal synthesis involves three distinct stages which can be roughly recognized in **Figure 1.3**. Nucleation from the initial solution, is the first stage of any crystallization process. In the second step, a seed is formed through atom-by-atom addition to the initial nuclei. In the final step, the seeds grow mainly in size reaching the desired size from the reaction mixture. Nucleation and growth of CQDs occurs in the solution phase in the presence of organic surfactant molecules. The reaction is terminated at the desired stage and can be finely calibrated to deliver monodisperse nanocrystals of the desirable size. The size of CQDs can be further tuned via the reaction temperature, concentration, type of capping molecules and molar ratios of precursors. One approach is that the size of the particles may be adjusted by first making small nanoparticles, which are used as seeds for growth adding controlled quantities of molecular precursors. Another approach is based on adjusting the growth rate of the nanocrystals. If the total amount precursors used in the reaction is fixed, the fast nucleation provides high

2

concentration of the nuclei and yields smaller CQDs and the slow nucleation provides low concentration and yields greater QDs. [2]
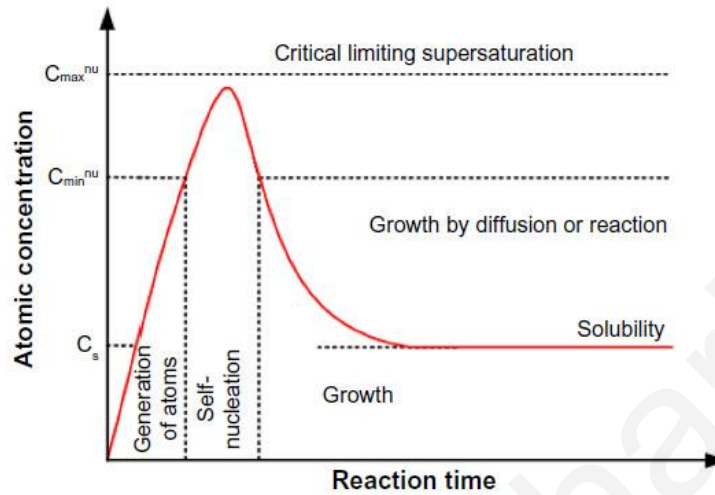
Figure 1.3 Plot of atomic concentration against time, illustrating the generation of atoms, nucleation, and subsequent growth. [7]

1.2   Electronic states

In this subsection we discuss the electronic properties of quantum-confined semiconductors in which the electrons and holes are confined to one or more directions.

1.2.1   Quantum Confinement

The optical properties of macroscopic crystals do not generally depend on the crystal size. For nanoscale crystals though a size-dependence can be indeed obtained as a result of quantum physics. In a simplistic model based on the Heisenberg uncertainty principle, if an electron is confined within a length of Δx, then the uncertainty in its momentum will be given by:

$$\Delta p_\chi \sim \frac{\hbar}{\Delta x}$$ 1.1

The electron with mass m, and confinement at x direction has then an additional kinetic energy of:

$$E_{confinement} = \frac{(\Delta p_x)^2}{2m} \sim \frac{\hbar^2}{2m(\Delta x)^2} \qquad\qquad 1.2$$

If the confinement energy is comparable or greater than the kinetic energy of the electron due to thermal motion then it becomes important. This condition can be written:

$$E_{confinement} \sim \frac{\hbar^2}{2m(\Delta x)^2} > \frac{k_B T}{2} \qquad\qquad 1.3$$

And tells us that quantum confinement effects become important when

$$\Delta x \lesssim \sqrt{\frac{\hbar^2}{m k_B T}} \qquad\qquad 1.4$$

This is equivalent to saying that Δx should be comparable to the de Broglie wavelength $\lambda_{deB} \sim h/p_x$ of the electron at a finite temperature T. This criterion gives a rough estimation of the physical dimensions of solids in order for quantum confinement effects to become important [1].

1.2.2   Density of Electronic States

Structures are classified according to the dimensions in which quantum confinement effects are observable, as shown in the following table:

Structure	Quantum confinement	Number of free degrees of freedom	Density of states
Bulk	None	3	$\sim E^{1/2}$
Quantum well	1-D	2	$\sim E^0$
Quantum wire	2-D	1	$\sim E^{-1/2}$
Quantum dot	3-D	0	Discrete

Table 1.1 Solids according to the quantum confinement dimensionality

The number of degrees of freedom is related to the type of quantum confinement. Electrons and holes in bulk semiconductors are free to move within their respective bands in all three directions, giving them three degrees of freedom. In a quantum well, electrons and holes are

4

confined in one direction, and thus have only two degrees of freedom. This means that materials behave as 2-D materials. The quantum wire exhibit carrier confinement in 2 dimensions (1-D materials) while a 3-D localization of electrons and holes is obtained in quantum dots (0-D materials). The quantization of the motion of electrons and holes has two main consequences. The energy of a particle increases from the quantum confinement effects and the energetic functional form of density of states is changed as shown in Table 1.1. [1]

The density of states (DOS) is the number of energy states per unit volume in the energy region (E, E + dE), or the number of electrons or orbitals per unit of energy. DOS influences the concentration of carriers and the optical, thermal and transport properties of the materials. The dimensionality of the structure on the other hand results in a different DOS, as observed in **Figure 1.4**. For quantum dots, DOS, is composed of a series of delta-functions in each quantized level. In this sense, quantum dots behave as artificial atoms [1].

$$f(E)dE = 2\delta(E - Ec) \hspace{4cm} 1.5$$
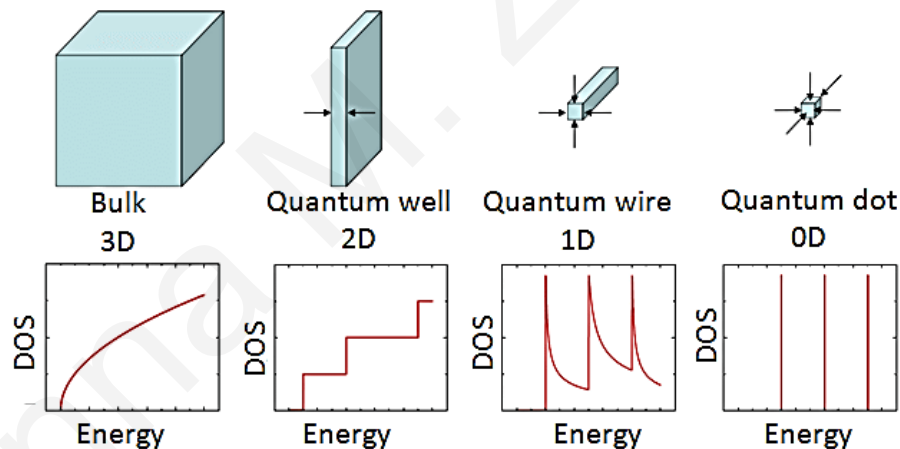
Figure 1.4 The shape of the density of states function for electrons in the conduction band of a semiconductor for each type of structure. [8]

1.2.3 Electronic Levels

Simple models of CQD electronic levels in the strong confinement regime, such as the CIS and AISe QDs studied in this thesis, are discussed next. CQDs are typically spherical, so a simple

strong confinement model assumes a 3-D potential with spherical symmetry. The Hamiltonian in spherical coordinates is then given by the following relationship

$$H = -\frac{\hbar^2 \nabla^2}{2m} + U(r) = -\frac{\hbar^2}{2mr^2}\frac{\partial}{\partial r}\left(r^2\frac{\partial}{\partial r}\right) - \frac{\hbar^2 \Lambda}{2mr^2} + U(r) \qquad 1.6$$

with

$$\Lambda = \frac{1}{\sin\theta}\left[\frac{\partial}{\partial\theta}\left(\sin\theta\frac{\partial}{\partial\theta}\right) + \frac{1}{\sin\theta}\frac{\partial^2}{\partial\varphi^2}\right] \qquad 1.7$$

The wavefunction solutions can be written as:

$$\psi_{n,l,m}(r,\theta,\varphi) = \frac{u_{n,l}(r)}{r}Y_{l,m}(\theta,\varphi) \qquad 1.8$$

where Y_{lm} are the spherical functions, and u(r) satisfies the following form of the Schrödinger equation

$$-\frac{\hbar^2}{2m}\frac{d^2u}{dr^2} + \left[U(r) + \frac{\hbar^2}{2mr^2}l(l+1)\right]u = Eu \qquad 1.9$$

The solutions of the radial equation can be written as:

$$u(r) = Arj_l(kr) + Brn_l(kr) \qquad 1.10$$

where $j_l(kr)$ are the Bessel functions, finite at the beginning of the axes and $n_l(kr)$ are the Neumann functions, infinite at the beginning of the axes.

Using the boundary conditions R(a) = 0 and R(0) = finite, the k is given by k=x_{nl}/a, where X_{nl} are roots of the spherical Bessel functions.

The state of the system is characterized by the three quantum numbers, the principal number n, the orbital number and the magnetic number m. The orbital quantum number determines the angular momentum value L:

$$L^2 = \hbar^2 l(l+1) \qquad 1.11$$

The magnetic quantum number determines the projection of angular momentum L to the z axis:

$$L_z = \hbar m$$

1.12

Every state with a certain l value is 2l + 1 degenerate. The states corresponding to different l values are usually denoted as s-, p-, d-, f -, and g-states and so forth in alphabetical order

For a spherically symmetric potential well with an infinite barrier, the energy values are expressed as follows

$$E_{n,l} = \frac{\hbar^2 x_{nl}{}^2}{2ma^2}$$

1.13
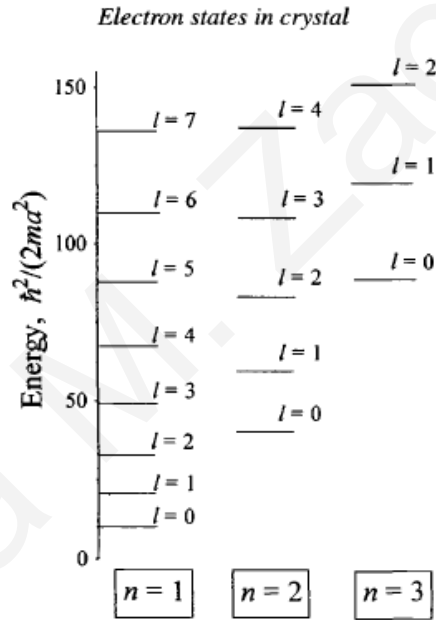
Figure 1.5 Energetic levels in spherical symmetric potential [9]

The de Broglie wavelength and exciton Bohr radius are noticeably larger than the lattice constant for most of the semiconductor crystal. A crystallite with a very large number of atoms can be thus treated as a macroscopic crystal with respect to the lattice properties but should be considered as a quantum box for quasiparticles. This statement provides a definition of a "quantum dot", which describes the electron properties of nanocrystals from the point of view of a particle in a box. Based on the effective mass approximation (EMA), we can consider these

particles as electrons and holes with the same effective masses as the ideal infinite crystal of the same stoichiometry. The quantum confinement effects can be revealed in the simple case of the spherical potential box with infinite walls, and considering electrons and holes with isotropic effective masses. The results can be derived for the two limiting cases, the so-called weak confinement and strong confinement limits.

Weak confinement limits corresponds to the case of a > a_B. and results in the quantization of the exciton center-of-mass motion. In weak confinement regime, the quantum confinement energy is also very negligible in comparison to the Coulomb potential. The energy in this case can be expressed as

$$E_{nml} = E_g - \frac{R_y^*}{n^2} + \frac{\hbar^2 x_{ml}^2}{2Ma^2}$$
1.14

The second term refers to the internal exciton energy due to the Coulomb interaction, characterized by the n principle quantum number and the third term refers to the center-of-mass exciton motion, characterized by the two additional quantum numbers, m and l.

For the lowest energy level we get the expression:

$$E_{1S1s} = E_g - Ry^*[1 - \frac{\mu}{M}\left(\frac{\pi a_B}{a}\right)^2]$$
1.15

where μ is the electron-hole reduced mass. The first exciton resonance experiences a high-energy shift by a value equal to the third term in the above equation. This term is small compared with Ry^* so far as α >> $α_B$ holds. This is the quantitative justification of the term "weak confinement".

Strong confinement limits corresponds to the case of a << a_B. This is the case of the CQDs studied in this thesis. Hence electron and hole are individually confined and their motion movement is also independent. The confined electron and hole have no bound state corresponding to the hydrogenlike exciton as the zero-point kinetic energy of electron and hole is quite larger than the Ry^* value due to confinement. The energy and momentum conservation

laws result in selection rules that allow optical transitions that couple electron and hole states with the same principal and orbital quantum numbers. Therefore, the absorption spectrum reduces to a set of discrete bands peaking at the energies

$$E_{nl} = E_g + \frac{\hbar^2 x_{nl}^2}{2\mu a^2}$$

1.16

For this reason, quantum dots in the strong confinement limit are sometimes referred to as artificial atoms because the quantum dots exhibit a discrete optical spectrum controlled by the size. The derivation of Equation **1.16** is provided in section 1.2.3 below.

A different approach to obtain the electronic structure of CNCs in strong confinement limits, uses a two-particle Hamiltonian with kinetic energy terms, Coulomb potential, and the confinement potential

$$-\frac{\hbar^2}{2m_e}\nabla_e^2 - \frac{\hbar^2}{2m_h}\nabla_h^2 - \frac{e^2}{\varepsilon|r_{e-}r_h|} - U(r) = H$$

1.17

In contrast to the hydrogen-like approach, the confinement potential *U(r)* does not allow the center-of-mass motion and the model of a particle with reduced mass should be considered independently. Several authors have treated this problem with the variational approach [10] [11] [12] and found that the energy of the ground electron-hole pair state (1s 1s) can be expressed in the form:

$$E_{1s1s} = E_g + \frac{\hbar^2\pi^2}{2\mu a^2} - 1.786\frac{e^2}{\varepsilon\alpha}$$

1.18

in which the third term defines the effective Coulomb electron-hole interaction. Comparing this term with the exciton Rydberg energy $Ry^* = e^2/2\varepsilon\alpha$, one can see that Coulomb interaction by no means vanishes in small quantum dots. Moreover, the Coulomb energy of the ground electron-hole pair state is even greater than in bulk crystals. [9]

1.2.4 Surface states – ligands

In the case of CQDs, the surfaces are disordered terminations of single crystal lattices, which lead to the formation of surface states. We can imagine the surface having the same band diagram, but with the abundance of additional states in the energy gap which can be sketched as shown in **Figure 1.6.** Surface states are energy states formed due to the non-uniform charge distribution between the surface and the inner bulk atoms of the semiconductor. For example such states can be formed due to the presence of unbound atoms with dangling bonds on the surface of a semiconductor. We expect a high density of surface states, because the discontinuity of the crystal lattice on the surface consists of at least one oscillating bond per atom. [13]
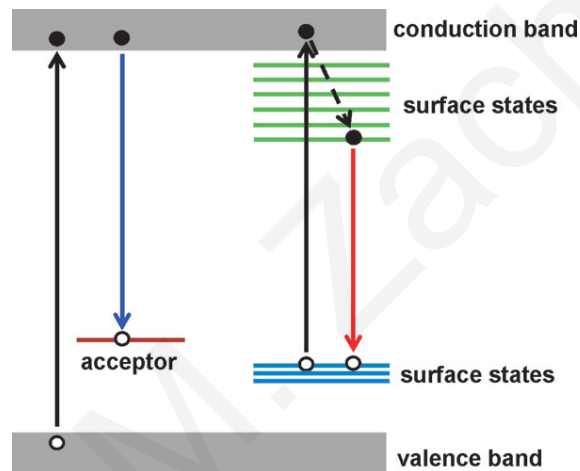
Figure 1.6 Energy model of p-type ZnO nanocrystals that includes the presence of surface states within the gap of ZnO [14]

A simplified model of the periodic crystal potential in one dimension can be sketched as shown in **Figure 1.7**. The potential has periodicity, a, the lattice constant, while near the surface it tends towards the vacuum level. The square potential (solid line) shown in **Figure 1.7** is an oversimplification which is mostly convenient for simple model calculations. An actual surface potential is affected by the charges and the formation of surface dipoles and is better approximated by the dashed line. The periodic crystal potential is subject to change in the solid-vacuum interface, so that the potential to be continuous. The change creates an electric field that traps electrons to sub-gap surface states.
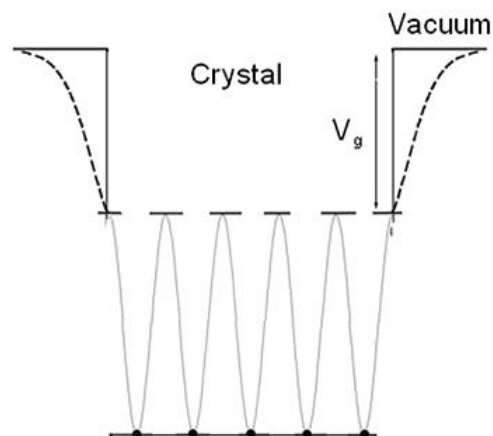
Figure 1.7 Simplified one dimensional model of a periodic crystal potential terminating at an ideal surface. [15]

Because of the high surface-to-volume ratio inherent to nanoscale objects, the surface has a strong influence on physical properties of CQDs including photophysics, charge transport, catalysis, and magnetism. As pointed above, surface states act as trapping sites for core QD carriers. To avoid such carrier losses, it is important that such states are partially or fully passivated. This is typically achieved by the decoration of the surface with organic surfactant molecules that have a multifunctional role in CQDs. They control nucleation, growth, chemical, and colloidal stability in the synthesis of colloidal nanomaterials. Due to steric forces between the ligands, CQD aggregation is avoided maintaining their small size and narrow size distribution, as well as preventing QD solution congealing. In addition, they contribute to the interparticle interactions and determine the spacing between neighboring QDs. The most common ligand coatings are based on long organic hydrocarbon molecules with anchoring end groups that provide the highest chemical flexibility. Most organic ligands act as bulky insulating barriers between QDs, hindering charge transport. Solution and solid-state ligand exchange reactions can replace the bulky surfactant molecules which shorter complexes improving charge transport. This is a widely used approach to fabricate CQD optoelectronic devices, however sometimes the new small ligands are prone to oxidation, leading to instabilities or deterioration of the optoelectronic properties. [2]

1.3 Excitons

Upon photoexcitation of an electron-hole pair in a semiconductor, the oppositely charged particles attract each other through electrostatic Coulomb interaction. This attractive interaction results in the formation of a bound, neutral electron-hole pair known as exciton that increases the oscillator strength and the optical transition rate. Excitons can be categorized into two main types:

• Wannier-Mott excitons, also called free excitons
• Frenkel excitons, also called tightly bound excitons.

(a) Free exciton   (b) Tightly bound exciton
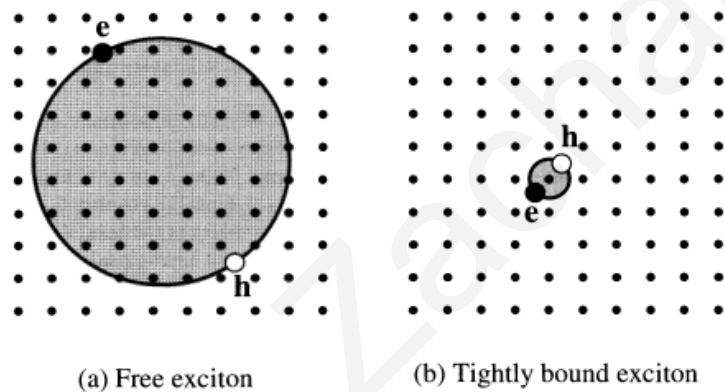
Figure 1.8 Types of excitons: (a) Free exciton (b) Tightly bound exciton [1]

The Wannier-Mott excitons are mainly observed in crystalline inorganic semiconductors and have a large radius that encompasses many atoms and can move freely throughout the crystal. The Frenkel excitons are found in insulator and molecular crystals and have a much smaller radius which is comparable to the size of the unit cell. This makes them highly localized to specific atoms or molecules. Stable excitons will only be formed if the attractive potential is sufficient to protect the exciton against collisions with phonons. Since the maximum energy of a thermally excited phonon at temperature T is ~ kT (kT ~ 0.025 eV at room temperature), this condition will be satisfied if the exciton binding energy is greater than kT. Wannier-Mott excitons have small binding energies of the order of 0.01 eV while Frenkel excitons have much larger binding energies in the range of 0.1-1 eV, which makes them highly stable at room temperature.

1.3.1 Free excitons - Binding energy and radius

It is known from atomic physics that the motion of hydrogenic atoms can be split into the center of mass motion and the relative motion. The center of mass motion describes the kinetic energy of the atom as a whole, while the relative motion determines the internal energy structure. The energies of the bound states can be determined by finding the eigenvalues of the Schrodinger equation for the relative motion. The main results are explained using the Bohr model. In applying the Bohr model to the exciton, it must be emphasized that the electron and hole are moving through a medium with a high dielectric constant ε_r with a reduced mass μ significantly smaller to the reduced mass of the electron-proton system in a hydrogen atom. Having these in mind, a simplified Bohr model can describe the energy spectrum of Wanner-Mott excitons. The bound states are characterized by the principal quantum number n. The energy of the nth level relative to the ionization limit is given by

$$E(n) = -\frac{\mu}{m_0}\frac{1}{\in_r^2}\frac{R_H}{n^2} = -\frac{R_x}{n^2}$$

1.19

where R_H is the Rydberg constant of the hydrogen atom 13.6 eV.

The radius of the electron-hole orbit is given by

$$r_n = \frac{m_0}{\mu} \in_r n^2 a_H = n^2 a_x$$

1.20

In insulators with band gaps greater than about 5 eV, α_x becomes comparable to the unit cell size, and the Wannier model is no longer valid. At the other extreme, R_x is so small in narrow gap semiconductors such as InSb that it is difficult to observe any free exciton effects at all. Hence, free exciton behavior is best observed in semiconductors with medium-sized band gaps in the range of 1-3 eV.

1.4 Point Defects in Semiconductors

It is useful to think about solids in terms of a regular repeating pattern of planes of particles. But it is important to recognize that solids are seldom perfectly ordered. There are basic mechanisms for introducing a point defect into the structure of a solid, as shown in **Figure 1.9**. When a

particle is missing at one or more lattice sites, a defect called vacancy is obtained. The equilibrium number N_u of vacancies is temperature dependent and can be obtained by the equation:

$$N_u = N exp\left(-\frac{Q_u}{KT}\right)$$ 1.21

where N is total number of atomic sites and Q_u is formation energy of the vacancy.

In a compound crystal when an element occupies a lattice site which nominally is occupied by atoms of the other compound element(s), an antisite defect is formed. [13] An interstitial impurity is obtained when an atom is placed in a small void crystal space, not normally occupied in the crystal lattice. Typically, the formation energy of such defect is higher than that of vacancies and thus their concentration is generally significantly lower than that of vacancies. Substitutional impurities result from replacing the particle that should occupy a lattice site with a different element, such as substituting a K^+ ion for a Na^+ ion in NaCl. If an ion with a different charge is substituted, the electrical neutrality of the crystal must be maintained. For example If a Ca^{2+} ion is substituted for a Na^+ ion, a second Na^+ ion must leave the crystal to maintain neutrality. [13]
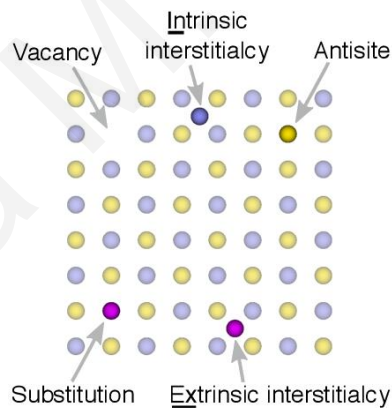
Figure 1.9 Basic mechanisms for introducing a point defect into the structure of a solid [16]

Point defects in crystals result in the following main interactions with the host crystal/intrinsic electronic states:

(i) Introduction of new discrete or band-like states:

Vacancies deprive the crystal from one electron per broken bond and act typically as acceptor states. Interstitials can offer their outer shell electrons and act typically as donors. Vacancies and interstitials can combine to yield donor or acceptor states (D-A pairs). Impurities and anti-sites can act either as donors or acceptors depending on the number of outer shell electrons compared to the lattice atoms they replace.

(ii) Perturbation by the defect deformation potential

Since the impurity is usually larger or smaller than the host crystal atoms, a local mechanical stress is induced. Typically, an interstitial will yield a compressional while a vacancy a dilational strain. [13]

(iii) Coulomb interactions between ionized impurities and electrons/holes

The density of states at conduction band and valence band are not having abrupt ends to create a band gap, but there is always a band tail creeping into the band gap region. An ionized donor exerts an attractive force on the conduction electrons and a repulsive force on the valence holes (acceptor act conversely). Since impurities are distributed randomly in the host crystal, the local interaction will be more or less strong depending on the local crowding of impurities. [13]
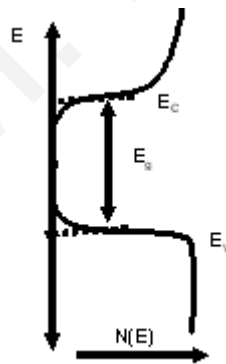
Figure 1.10 Schematic representations of band tail in direct band gap semiconductors [13]

Point defects can influence or mediate optical transitions in semiconductors such as the recombination channels (b), (c) and (d) illustrated in the **Figure 1.11**, with (b) defining a Donor-to-Valence Band (D-VB) transition, (c) being a Conduction Band-to-Acceptor transition (CB-A) and (d) a Donor-to-Acceptor (D-A) transition.

15
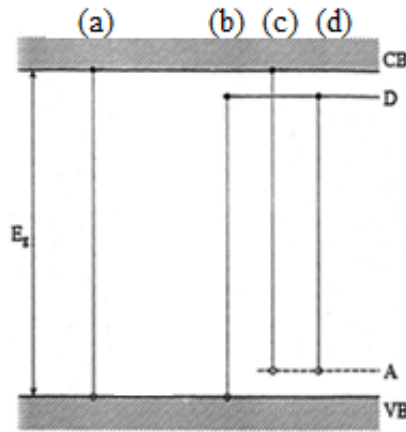
Figure 1.11 Schematic illustration of recombination channels after a high-energy impact. (a) Conduction Band-to-Valence Band transition, (b) Donor-to-Valence Band transition, (c) Conduction Band-to-Acceptor transition, (d) Donor-to-Acceptor (D-A) transition. [13]

In D-A transitions, due to the spacing-dependent D-A Coulomb interaction a large range of optical transitions is possible, given by the following energies: $hv = E_g - E_a - E_d + \frac{q^2}{\varepsilon r}$, where E_g is energy gap, E_α is acceptor energy and E_d is donor energy. For distant pairs the Coulomb term is negligible and the lowest possible transition is obtained. For larger distances transitions require a tunnelling process and become less probable as r increases. At the same time though the number of interacting pairs decreases with r, so there is an optimum distance where the emission intensity goes through a maximum.
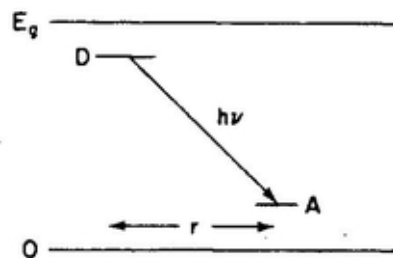
Figure 1.12 Schematic of a Donor-Acceptor transition in a Semiconductor [13]

Transitions can also be obtained between band tail states. Band tails are formed as explained above and exhibit an exponential density of states, known as Urbach tail. The exponential tail contributes to the interband absorption below the gap. Radiative transitions (PL) between tail states can also occur. However as the local energy gap is constant, the electron or hole has to

16

tunnel or relax to a neighbouring tail state with lower energy to detect a distinct (from the band-to-band) lower energy tail-to-tail emission. [13]

1.5   Recombination in Semiconductors

1.5.1   Radiative Recombination

Radiative recombination is one of the dominant processes in direct bandgap semiconductors. When a photon is absorbed by a semiconductor, an electron is excited from the valence band to the conduction band leaving a hole in the valence band. The electron-hole pair recombines releasing a photon. (**Figure 1.13 b**) When the electron is promoted from the valence band to higher energy states, then it relaxes to the band edge while releasing the excess energy as heat via interactions with phonons. After relaxation the electron and hole recombine by emitting a photon. (**Figure 1.13 a**)
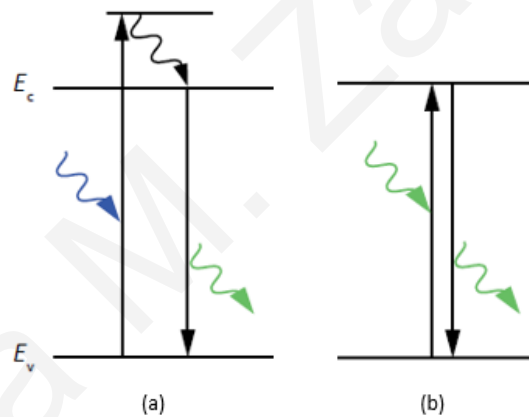
Figure 1.13 Radiative Recombination (a) exciting from the valence band to a higher energy states (b) exciting from the valence band to the conduction band.

1.5.2   Non - Radiative Recombination

There are three basic types of non–radiative recombination in CQDs, namely: (i) band to band recombination, (ii) recombination through defect levels that was discussed in section 1.4 and (iii) Auger recombination. In non-radiative band to band recombination, an electron from the conduction band directly recombines with a hole in the valence band while releasing energy as heat when coupled to lattice vibrations (**Figure 1.14 a**). Defect recombination is mediated by donor and/or acceptor states, as elaborated previously (**Figure 1.14 b**).

17

Auger recombination is the most important recombination channel at high carrier densities, as it involves at least three carriers. An electron and a hole recombine, but rather than emitting the energy as heat or as a photon, the energy is given to a third carrier, electron or hole. Such carrier becomes hot via the energy transfer from the electron-hole pair and it can become ionized, trapped or thermalizes back down to the conduction/valence band edge.
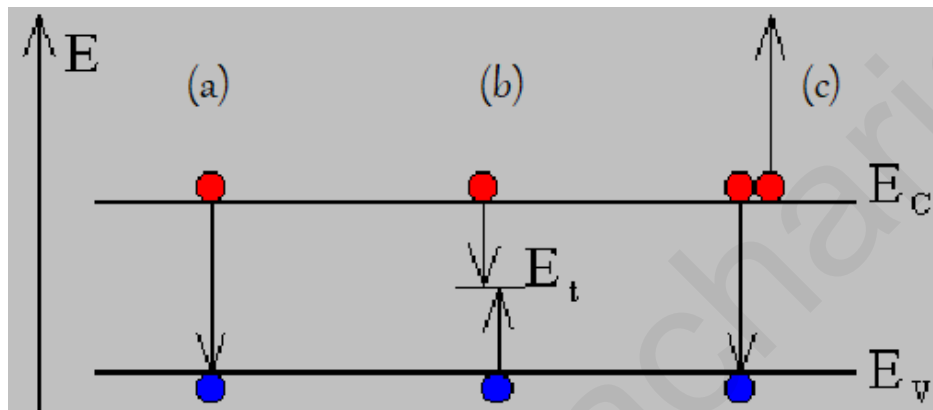
Figure 1.14 Non - Radiative Recombination of electron-hole pairs produced via: (a) Band to Band Recombination (b) Recombination through Defect Levels (c) Auger Recombination [17]

2 Experimental Methods

2.1 Film Deposition Techniques

There is a variety of solution-processed thin film deposition methods that include different versions of casting, printing and coating techniques such as those shown in **Figure 2.1** each having its own advantages and limitations. For the purposes of this thesis the two main techniques used for film deposition has been spin-coating and drop-casting.
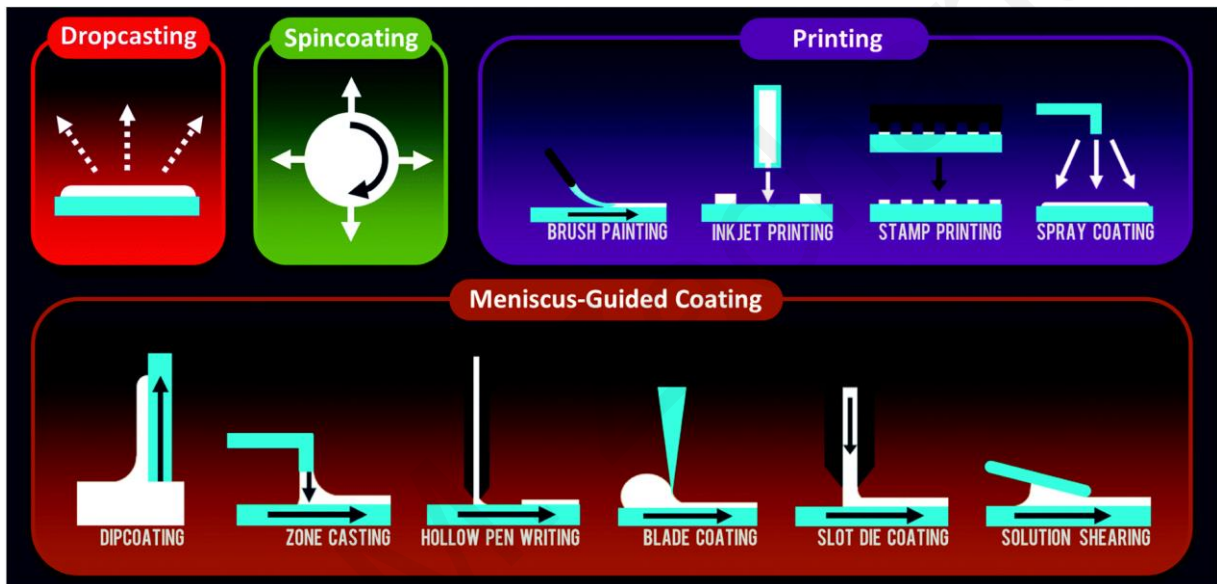
Figure 2.1 Schematic of various solution-processed thin film deposition techniques [18]

2.1.1 Spin Coating

Spin coating is most-widely used technique to produce uniform thin films with thickness of the order of micrometers to few nanometers. Due to many advantages, such as low cost, simplicity and quite high uniformity of solid produced, the spin coating process has been extensively studied and applied in various fields. [19] The technique is based on depositing a small amount of liquid on a substrate and using the centrifugal force of the spinning surface to drive the liquid radically outward. Viscous force and surface tension are the main causes for the flat deposition on surface. When the substrate is spinning at a constant rate, fluid viscous forces dominate fluid

thinning behavior. The last step is the drying, in which the solvent is evaporated and the liquid layer of the material solidifies to form a film. [20]
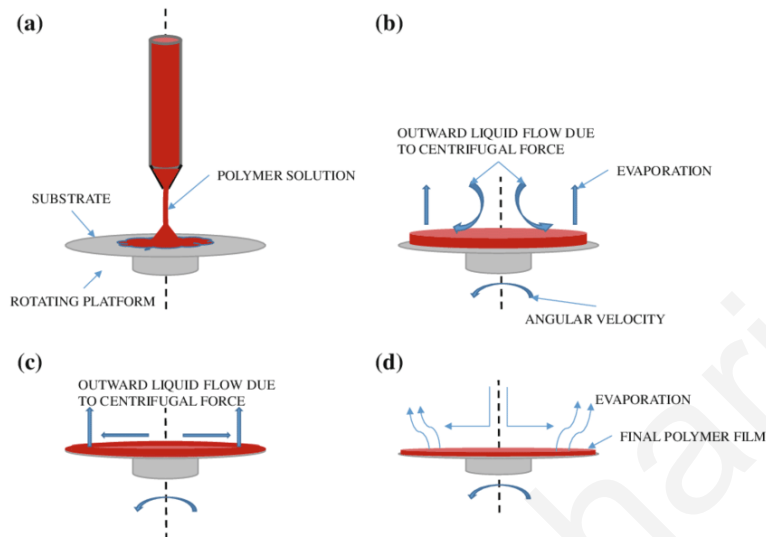
Figure 2.2 Spin coating process for the fabrication of thin films [19]

2.1.2   Drop- Casted Deposition

Drop casting is the simpler method for the processing of films out of solutions. This technique is similar to spin coating, with the difference that no substrate spinning is required. In such technique, control over the film thickness is provided by the volume and concentration of the dispersion. Other variables which affect the film structure are the rate of evaporation, the drying conditions and substrate wetting. In this method, one of the advantages is less material wastage. On the other hand, there are various disadvantages, including non-uniform film formation and difficulty in controlling film thickness. [21]
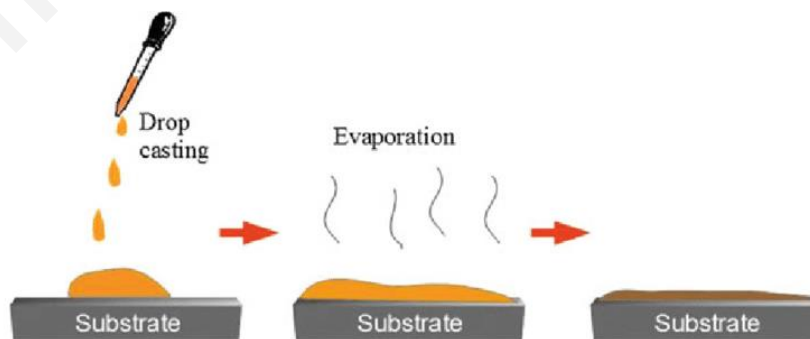
Figure 2.3 Film deposition using drop-casting technique [21]

2.1.3   Pulsed Laser Deposition (PLD)

Pulsed laser deposition (PLD) is established as an efficient deposition method for multi-component films due to the stoichiometric transfer of the target material to the deposited film. PLD stands out from other deposition techniques as crystalline films can be produced at low deposition temperatures, due to the non-equilibrium process occurring during PLD growth. Along with the high deposition rates and its simplicity of use, PLD can be considered a fast, simple and low cost method for depositing films. For solar cell applications, a single-step, fast process is important to reduce the manufacturing time and cost. The advantageous figures of PLD could bring the technique in the forefront as an excellent tool to fabricate solar cells. [22]

PLD is based on a high-power pulsed laser beam that focuses on a material target, placed inside a vacuum chamber. The target material is vaporized by a laser beam in the form of a plasma plume and deposited on the substrate as a thin film. PLD can achieve good transfer of stoichiometry of the target composition [23]. **Figure 2.4** shows the PLD mechanism of operation. The possibility to tune various experimental parameters (laser pulse fluence, target to substrate distance, substrate temperature, background gas pressure, etc.) allows finding optimal conditions for the growth of high-quality films of complex materials. Laser fluence and substrate temperature are two critical parameters, influencing the purity and stoichiometry of the resulting films. [24]
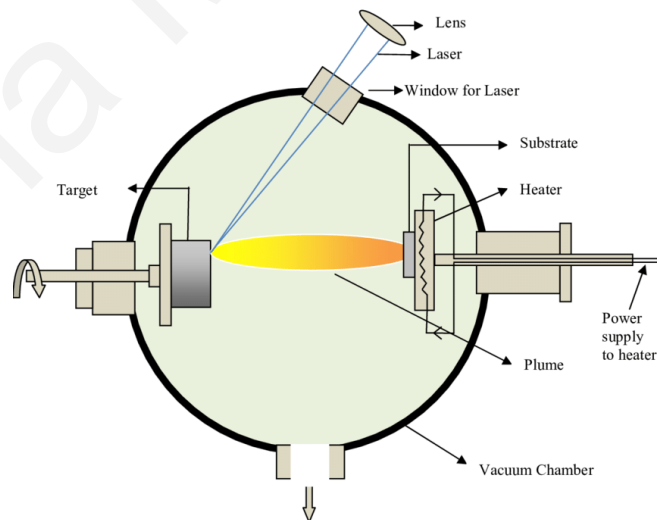
Figure 2.4 A schematic diagram of the pulsed laser deposition setup. [25]

2.2 Optical Absorption

Electrons are excited from valence band to conduction band by making optical transitions across the fundamental band gap of the material, in a process called interband absorption. [1] The opposite process in which electrons relax from excited state bands by emitting photons, is called interband luminescence and will be discussed in section 2.3. An energy diagram of two separated bands in a solid is displayed in **Figure 2.5**. An electron is excited between the bands of a solid it by absorbing a photon. This can only happen if there is an electron in the initial state in the lower band and the final state in the upper band is empty. (Pauli exclusion principle). A photon excites an electron from the filled valence band to the empty conduction band. By applying the law of conservation of energy to the interband transition, it is obtained that:

$$E_f = E_i + \hbar\omega \qquad\qquad 2.1$$

Where E_i is the energy of the electron of the initial state in the lower band, E_f is the energy of the final state in the upper band, and $\hbar\omega$ is the photon energy. Interband transitions are not possible unless $\hbar\omega >$ Eg and a continuous absorption spectrum from the low energy threshold at Eg to an upper value set by the extreme limits of the participating bands is observed. When an electron is excited then leaves the initial state in the lower band a vacancy. This vacancy is called hole. The interband absorption process creates a hole in the initial state and an electron in the final state, so it generates an electron-bole pair. [1]
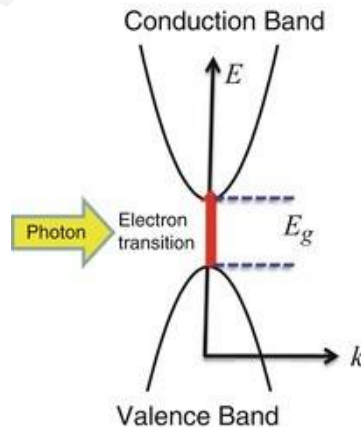
Figure 2.5 Energy Diagram of two separated bands, an initial state in an occupied lower band and a final state in an empty upper band. [26]

Absorption is quantified by the absorption coefficient α, determined by the quantum mechanical transition rate $W_{i\rightarrow f}$ for the excitation of an electron from an initial quantum state ψ_i to a final quantum state ψ_f. The transition rate is given by Fermi's Golden Rule:

$$W_{i\rightarrow f} = \frac{2\pi}{\hbar}|M|^2 g(\hbar\omega)$$

2.2

The quantum mechanical transition depends on the matrix element M and the joint density of states $g(\hbar\omega)$. The matrix element describes the effect of the perturbation introduced by the electromagnetic field and is given by:

$$M = \langle f|H'|i\rangle = \int \psi_f^* H'(r)\psi_i^* d^3r$$

2.3

Where H' is the perturbation related with the light wave and r is the electon's position vector. The electric field E causes a shift in energy of a charged particle equal to -p·E, where p is the electric dipole moment of the particle. The perturbation interaction describes the electric dipole interaction between electron and light is given by:

$$H' = -p_e \cdot E_{photon}$$

2.4

where p_e is the electron dipole moment. The electromagnetic wave is given by:

$$E_{photon}(r) = -E_o e^{ikr}$$

2.5

and thus the perturbation takes the form:

$$H' = -eE_o \cdot r e^{ikr}$$

2.6

The electron states in a crystalline solid are described by Bloch functions, which allow us to write the initial and final state:

$$\psi_i(r) = \frac{1}{\sqrt{V}} u_i(r) e^{ik_i r}$$

2.7

$$\psi_f(r) = \frac{1}{\sqrt{V}} u_f(r) e^{ik_f r}$$

2.8

where u_i and u_f are the envelope functions for the initial and final band respectively, V the normalization volume, while k_i and k_f the wave vectors of the initial and final electron states. By combining equations (**2.3**),(**2.6**),(**2.7**) and (**2.8**) we get:

$$M = \frac{e}{V} \int u_f^*(r) e^{-ik_f r} (E_o \cdot r e^{ikr}) u_i(r) e^{ik_i r} \, d^3 r$$

2.9

Here the limits of the integral are over the whole crystal. The momentum conservation, $\hbar k_f$ - $\hbar k_i$ = $\hbar k$, leads to the conclusion that the phase factor is equal to zero. According to Bloch's theorem, the u_i and u_f are periodic functions with periodicity identical to the lattice and we can separate the integral of the whole crystal into a sum over the unit cells. Thus considering that unit cells are equivalent then we obtain:

$$M \propto \int u_i^*(r) z u_f(r) d^3 r$$

2.10

The light is polarized along the z-axis. This matrix element represents the electric-dipole moment of the transition. The second factor in equation (**2.2**), namely the density of states function was discussed in Section 1.2.2. By evaluating the density of states at E_i and E_f, one can obtain the joint density of states.

If we consider the simplified parabolic band structure model, shown in **Figure 2.6**, the frequency dependence of the absorption coefficient can be calculated analytically. The dispersion of the bands is determined by their respective effective masses, namely m_e^* for the electrons, m_{hh}^* for the heavy hole, m_{lh}^* for the light hole and m_{so}^* for the split-off holes.

The band dispersion is given by the expressions:

$$E_e(k) = E_g + \frac{\hbar^2 k^2}{2m_e^*} \qquad\qquad 2.11$$

$$E_{hh}(k) = -\frac{\hbar^2 k^2}{2m_{hh}^*} \qquad\qquad 2.12$$

$$E_{lh}(k) = -\frac{\hbar^2 k^2}{2m_{lh}^*} \qquad\qquad 2.13$$

$$E_{so}(k) = -\Delta - \frac{\hbar^2 k^2}{2m_{so}^*} \qquad\qquad 2.14$$

Conservation of energy during a heavy or a light hole optical transition requires that:

$$\hbar\omega = E_g + \frac{\hbar^2 k^2}{2m_e^*} + \frac{\hbar^2 k^2}{2m_h^*} \qquad\qquad 2.15$$

where $m_h^* = m_{hh}^*$ or m_{lh}^* for the heavy and light hole transition respectively.

By defining the reduced electron-hole mass μ:

$$\frac{1}{\mu} = \frac{1}{m_e^*} + \frac{1}{m_h^*} \qquad\qquad 2.16$$

and by combining Eq. (**2.15**) and (**2.16**) we get

$$\hbar\omega = E_g + \frac{\hbar^2 k^2}{2\mu} \qquad\qquad 2.17$$

So by substituting Eq. (**2.17**) into $g(E) = \frac{2g(k)}{dE/dK}$ where $g(k)dk = \frac{4\pi k^2 dk}{(2\pi)^3}$, the joint density of states can be evaluated:

For $\hbar\omega < Eg, g(\hbar\omega) = 0$

$$\text{For } \hbar\omega \geq Eg, g(\hbar\omega) = \frac{1}{2\pi^2}\left(\frac{2\mu}{\hbar^2}\right)^{3/2}(\hbar\omega - Eg)^{1/2}$$

2.18

Therefore the density of states factor rises as (ħω-Eg) $^{1/2}$ for photons with energy greater than the energy gap of a direct gap semiconductor material.

By substituting the expression for the joint density of states in the Fermi's Golden rule expression, the energy dependence of the absorption coefficient is obtained:

$$\text{For } \hbar\omega < Eg, \ a(\hbar\omega) = 0$$
$$\text{For } \hbar\omega \geq Eg, a(\hbar\omega) \propto (\hbar\omega - Eg)^{1/2}$$

2.19

Photons with energy smaller than the gap don't induce absorption; absorption increases as (ħω-Eg)$^{1/2}$ for photons with higher energy, while according to Eq.(**2.18**) stronger absorption is obtained in semiconductors exhibiting increased reduced electron-hole mass .
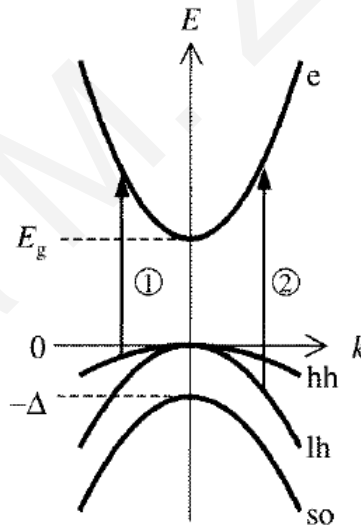
Figure 2.6 Band structure of a four-valent semiconductor with a typical direct gap. The light hole (lh), the heavy hole (hh), the split-off hole (so) and the electron (e) band are displayed.

In the above, rather simplistic model various contributions have been neglected. Coulomb interactions can enhance the absorption rate and create an exciton. Moreover a semiconductor

contains impurity, defect states that give rise to absorption transitions with smaller energies than that of the energy gap.

The absorption of light by an optical medium is quantified by its absorption coefficient α. If the beam is propagating in the z direction, and the intensity at position z is I(z), then the absorbed intensity dI is:

$$dI = -\alpha dz \; x \; I(z)$$
2.20

where dz is thickness of a slice. By integration, Beer's law is obtained:

$$I(z) = I_0 \, e^{-\alpha z}$$
2.21

where I_o is the optical intensity at z = 0.

The absorption of an optical medium can also be quantified in terms of the optical density (O.D), defined as:

$$O.D = -log_{10}(\frac{I(l)}{Io})$$
2.22

where l is the length of the absorbing medium. The optical density is related to the absorption coefficient α through: [1]

$$O.D.= \frac{\alpha l}{log_e 10} = 0.434\alpha l$$
2.23

Experimental setup - Perkin Elmer Lambda 1050

A typical setup can be seen in **Figure 2.7**. There are two light sources. For the 300-3300 nm wavelength range, a tungsten-halogen lamp is used, while illumination for the 200-320 nm wavelength range is provided by a deuterium light source. The light is spectrally analyzed by a

monochromator and it is subsequently separated into two quasi-monochromatic beams. One beam transmits through the reference sample with intensity Io. The reference sample is a transparent substrate, identical to that the studied film is deposited on, which is placed within the path of this beam to take into account the deviation from the 100% transmittance due to light scattering or absorption. The second beam transmits through the sample I(z). Both of the beams are measured simultaneously by three photodetectors. Detection at the 250-850 nm wavelength range is provided by a photomultiplier tube (PMT), an InGaAs photodiode is used for the 850-1700 nm range and for longer wavelengths of 1700-3000 nm, the operating detector is a PbS diode (LAMDA 1050). The spectrometer is connected to a computer from which the data are collected for processing. Absorption spectra can give us important information about the nature of energy gap (direct or indirect energy gap), exciton energy and structure of material, the presence of defect or Urbach tail states.
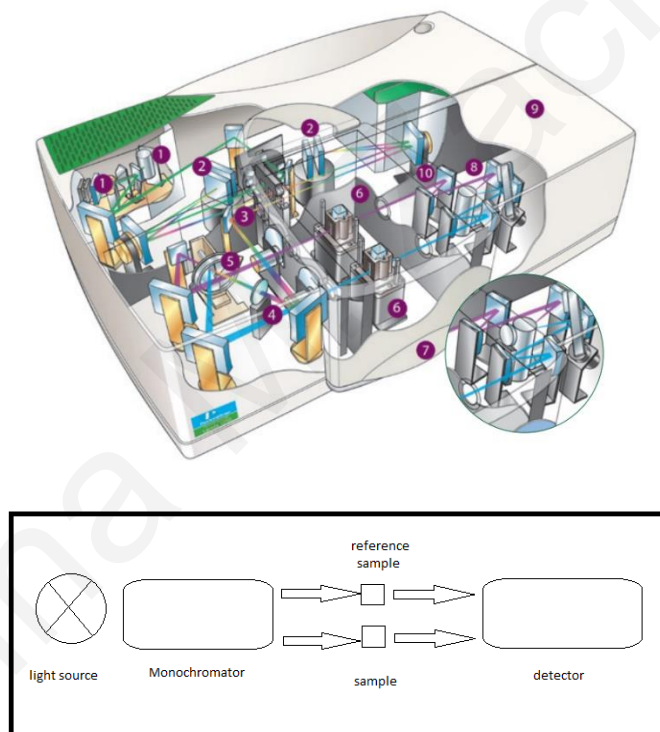
Figure 2.7 Perkin Elmer Lambda 1050 - Schematic diagram of the method used to measure optical density [27]

2.3 Photoluminescence

In a semiconductor, an excited electron can recombine with a hole in the valence band, emitting a photon. This process is called luminescence and can occur via a number of mechanisms. Luminescence can originate from direct light absorption in a process called photoluminescence (PL). This process is more complex than absorption due to the additional activation of carrier relaxation mechanisms that take place before the emission in the solids. Moreover the emission spectrum can be affected by the thermal distribution of the carriers in the bands and the presence of impurity, surface, shallow or deep defect states. An excited electron-hole pair is produced by an interband optical absorption process, relaxes to the bottom of the respective bands via ultrafast interactions with phonons and subsequently recombines with a thermalized hole, emitting a photon. Typically, when a transition has large absorption coefficient, it also exhibits high emission yield and short radiative lifetime i.e. large radiative rate but no light will be emitted unless the upper level is populated and there are empty states (holes) in the ground level. Based on the model used for interband absorption, the luminescence intensity as a function of frequency ν will be given by:

$$I(h\nu) = \propto |M|^2 g(h\nu) \; x \; level \; of \; occupancy \qquad 2.24$$

where the level of occupancy factor gives the probability that the upper level is occupied and the lower level empty. M is the matrix element of the quantum mechanical transition probability derived by Fermi's golden rule and g(hv) the joint density of states function.

The mechanism of photoluminescence in semiconductors is schematically illustrated in **Figure 2.8**, which plots the *E-k* diagrams for a direct band gap material **Figure 2.8 (a)** and an indirect gap material **Figure 2.8 (b)**, where *E* and *k* are respectively the kinetic energy and wave vector of the electron or hole. The direct and indirect gap materials are distinguished by their relative positions of the conduction band minimum and the valence band maximum in the Brillouin zone. During absorption a photon, energy and momentum are conserved. In a direct band gap material, the band edges have the same *k* values ($\hbar \vec{k_i} = \hbar \vec{k_f}$, where k_i and k_f are the wave vectors of the initial and final electron states respectively), conservation of momentum for the photoexcitation of the electron which only involves a photon: $\hbar \vec{k_i} + \hbar \vec{k_{phot}} = \hbar \vec{k_f}$, where $\vec{k_{phot}}$

is the wave vector of the absorbed photon (in the order of $2\pi/\lambda \sim 10^5$ cm^{-1}) which is negligible compared to the electron wave vector (which is related to the size of the Brillouin zone $\pi / a \sim 10^8$ cm^{-1}, where α is the unit cell dimension in the order of a few angstroms).

On the other hand, in an indirect band gap material, the band edges have different k values. For the conservation of momentum besides the photon absorption must be assisted by either absorbing or emitting a phonon, because the electron wave vector must change significantly during excitation from the valence band to the conduction band; the absorption of a photon alone cannot provide in such case the required momentum change since $|\overrightarrow{k_{phot}}| << |\overrightarrow{k_i} - \overrightarrow{k_f}|$. The excited electron and holes relax very rapidly ($\sim 10^{-13}$ s) to the lowest energy states within their respective bands by emitting phonons. When the hole and electron thermalize, they recombine *radiatively* via the emission of a photon, or *nonradiatively* with the emission of phonons or by transferring the carriers energy to impurities or defects in the material or dangling bonds at the surface. The energy separation between the electrons and the holes approximately equals to the energy of the band gap. The luminescence emitted by both types of semiconductors occurs at an energy close to the band gap Eg.

The PL efficiency is determined by the competition between radiative and nonradiative recombination. For an indirect gap material, the PL requires a change in both energy and momentum for the excited electron involving both a photon and a phonon. The PL process for an indirect gap material is a slow process ($\sim 10^{-5}$ -10^{-3} s) and a relatively small efficiency due to the competition with nonradiative combination. On the other hand, in a direct gap material, the emission of a photon does not need the assistance of a phonon to conserve momentum. Therefore, the PL process for a direct gap material is a fast process ($\sim 10^{-9}$ -10^{-8} s) and the PL efficiency is typically high.
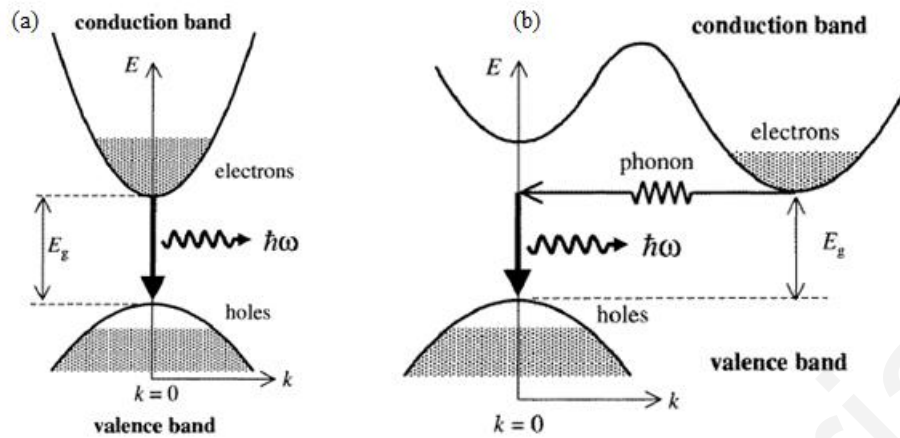
Figure 2.8 The mechanism of photoluminescence for a direct band gap semiconductor (a) and an indirect gap semiconductor (b)[1]

PL experiments can provide important information about the nature of the photoexcitations and recombination channels in the material. Further information about the material can be extracted by varying experimental parameters of the PL experiments such as excitation density (*excitation-dependent PL*), sample temperature (*temperature-dependent PL*), the excitation wavelength (*resonant versus non-resonant PL*) and polarization state (*anisotropy measurements*). For example, an excitation-dependent PL experiment can provide information for recombination mechanisms such as trapping or Auger, based on the power law exponent that describes the intergrated PL dependence on excitation. On the other hand, temperature-dependent PL provides information of thermally-activated processes such as trapping or de-trapping of carriers. Excitation photoluminescence (PLE) is a useful method to investigate the electronic level structure of materials and provides information on emissive interband transitions. PLE monitors the photoluminescence intensity at a specific wavelength while varying the excitation beam wavelength.

Experimental setup PL I

This PL setup is based on a Horiba-Jobin Yvon FL3 spectrophotometer. The main parts of the setup include a series of additional diode lasers coupled to the sample chamber of the spectrophotometer or the monochromatically-filtered output of a broadband Xe lamps as the excitation sources. The lamp with the combination of a monochromator allows for a continuous

tunable excitation source throughout the visible. The samples are typically placed in vacuum, in a temperature controlled liquid nitrogen (77 K) optical cryostat. The detection part consists of a second monochromator that spectrally analyzes the emitted light and a visible PMT detector covering the 250-850 nm range or an infrared PMT for the 950-1700 nm range. A schematic representation of the PL setup I is presented on **Figure 2.9**.
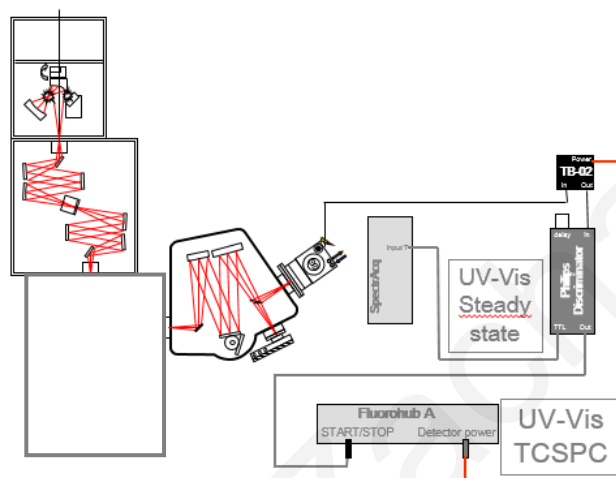
Figure 2.9 Schematic of the Horiba-Jobin Yvon FL3 spectrophotometer in which PL setup I is based on [28]

Experimental setup PL II

This PL setup is based on a high resolution 0.75 m Princeton Instruments, Acton Advanced 2750A spectrometer. The samples are typically placed on a temperature controlled, closed cycle optical refrigerator, being excited by a series of continuous wave (cw) laser diodes. Between the sample and the detector, two lenses with focal lengths of 150 mm and 200 mm are placed, to make the beam parallel and focused onto the entrance of the spectrometer slits, respectively. As the beam enters the spectrometer, it illuminates a concave mirror (2) which makes the collected beam parallel. By means of a flat mirror (3) the beam is directed to the diffraction grating (4) (**Figure 2.10**) and then onto one of the two detectors, namely an InGaAs array detecting at the 800-1700 nm wavelength range or a CCD camera used for the region of 250-950 nm.
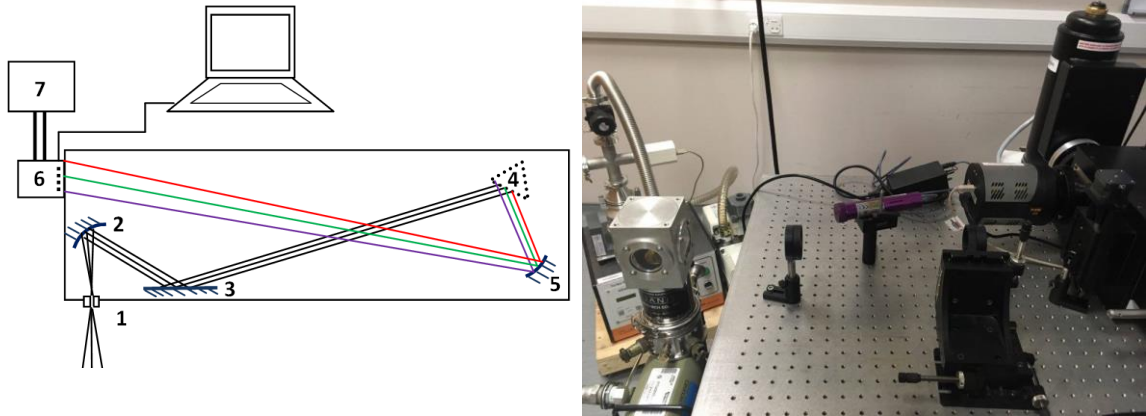
Figure 2.10 Experimental PL setup II – Princeton Instruments, Acton Advanced 2750A

2.4 Time-resolved PL

When a sample is excited by a pulse of light, an initial population of n_0 carriers exists is in its excited state. The excited-state population decays with a rate **k** according to

$$\frac{dn}{dt} = -kn(t) \qquad\qquad 2.25$$

where n(t) is the number of excited carriers at time t following excitation. The solution of this equation is an exponential decay of the excited-state population:

$$n(t) = n_0\, e^{-kt} \qquad\qquad 2.26$$

The lifetime τ is the inverse of the decay rate k: $\tau = 1/k$ and the decay rate k is the sum of rates of all decay processes. The intensity I(t) to an infinitely sharp pulse of light at time t = 0 is given by

$$I(t) = Ae^{-\frac{t}{\tau}} \qquad\qquad 2.27$$

while in the case of multi-exponential decay the intensity is given:

$$I(t) = \sum_i A_\iota e^{-\frac{t}{\tau_i}}$$

2.28

The average PL lifetime t_{avg} of the PL decays is calculated from the relation [22]:

$$t_{avg} = \frac{\sum_i A_i \tau_\iota^2}{\sum_i A_i \tau_i}$$

2.29

The relative weight of each of the emissive channel contributions (*Wi*) was calculated by the following formula:

$$W_i = \frac{A_i}{\sum_{j=1}^3 A_j}$$

2.30

Experimental setup TRPL

Time-resolved PL (TR-PL) is measured by exciting the sample with a pulsed light source, and measuring the subsequent photoluminescence decay as a function of time. Our experiment takes place in the same setup with that of **Figure 2.9** by employing appropriate fast electronics and pulsed lasers, with pulse width of tens to hundreds of picoseconds while the PL is detected via a visible or a near-IR photomultiplier tube (PMT). In combination with the response time of the electronics and detectors, the setup exhibits a time-resolution of the order of 50 ps in the visible and 100 ps in the infrared. Time resolution is obtained via time correlated single photon counting (TCSPC) which is a digital counting technique. Measurements build a probability histogram relating the time between an excitation pulse and the observation of the first emitted photon. [29] In the case of mixtures of luminescence species with overlapping spectra, a variation of the technique known as time-resolved emission spectra (TRES) is employed. A typical TRES measurement involves moving the monochromator in fixed wavelength steps, with time-resolved decays acquired at each wavelength. With this process, a three dimensional graph of PL intensity versus wavelength (energy) and time can be obtained. It is possible to take "slices" of data in the intensity –wavelength plane to obtain PL spectra at different times during the decay. [29] The aforementioned time-resolved techniques allow us to study the temporal

characteristics of recombination processes in CQDs and extract important information such as the exciton lifetime, Auger or trapping rates etc.

2.5 Transient Absorption (Pump –Probe)

Ultrafast transient absorption is employed for the study of the relaxation and recombination dynamics of carriers down to the femtosecond regime. Pump-probe measurements included in the thesis were carried out by the group of Prof. A. Othonos at the Laboratory of Ultrafast Science at the Physics Department of the University of Cyprus using the setup is displayed in **Figure 2.12.**

In a pump-probe experiment, the incident laser pulse is divided into two pulses with different intensity, a pump and a probe pulse. Pump pulse constitutes the majority part of the intensity of the initial pulse and excites the sample. The probe pulse is much weaker than the pump pulse in order to ensure that it will not perturb the sample properties. So we can detect the changes induced to the sample by the pump pulse. The two pulses follow different optical paths and a translation stage is placed in the pathway of the probe beam to induce an adjustable time delay Δt with respect to the pump pulse. The probe beam changes when interacting with the sample due to changes in the sample properties induced by the incident pump beam. The modifications depend on the temporal delay Δt of the probe beam with respect to time zero. The time zero corresponds to the arrival time of the pump beam. For times $\Delta t \geq 0$, the probe beam experiences the changes on the sample and for $\Delta t < 0$, the probe beam reaches the sample before the pump beam and no changes are detected.

In general, positive differential absorption signals originate on photoinduced absorption transitions of carriers from the ground state to higher excited states or within different excited states. Negative differential absorption can typically signify state bleaching due to the filling of the relevant probed state by pump pulse excited carriers. Negative signals can also indicate the accumulation of a large enough excited carrier population to initiate stimulated emission transitions.
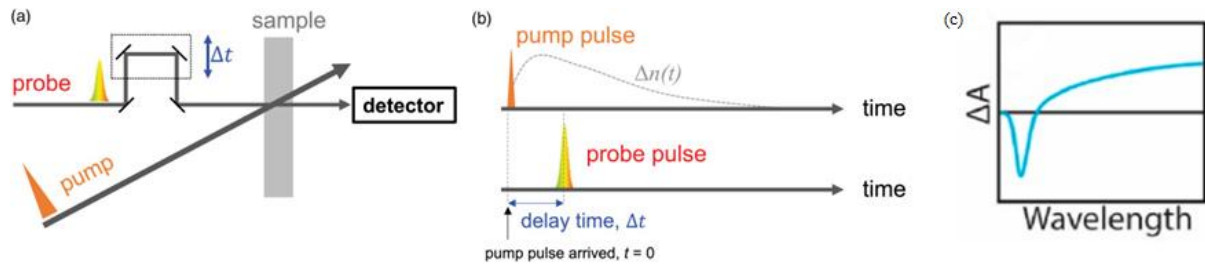
Figure 2.11 (a) Schematic diagram of the pump–probe technique. Time delay (Δt) between pump and probe pulses (b) Principle of pump–probe spectroscopy. Time-dependent refractive index changes n(t) of the sample induced by pump pulses can be observed by detecting the intensity variations of probe pulses. (c) Transient absorption spectra [30] [31]

Experimental Setup Pump-Probe Absorption

In our experiments, two different ultrafast amplifier laser systems in supercontinuum non-collinear pump-probe configuration (two beams incident onto the sample in a different angle) have been used. A beam splitter divided the output beam produced by the amplifier system into two components, the pump and the probe beams. The larger part of the output energy is directed into an Optical Parametric Amplifier (OPA), which converts the wavelength of the pump beam and provides pulses within a wide spectral region (290-1800nm). For the experiments in this research work, OPA was used to generate excitation pulses above band gap for the materials under investigation.

The probe beam at 800 nm, is used to generate a supercontinuum white light for absorption measurements. This was achieved through a strong focus of the beam on a 1mm sapphire plate. Two different setups are used for the range of selected probing wavelengths. The first setup produces the continuum white light in the region 500-1000 nm. The second one is used to generate wavelengths in UV region 300-500nm. This is achieved through the additional second harmonic crystal that initially converts the probe wavelength to 400nm and then utilizing this second harmonic to produce the wight light. Using a computer controlled translation range, which was placed in the pathway of the probe beam, the variation of the relative delay time between pump and probe pulses was achieved. The reflection change and transmission signals were detected using Si photodiodes which were measured using lock-in amplifiers with reference to an optical intensity modulator (an optical chopper) of the pump team, in order to

enhance signal to noise ratio. The lock-in amplifier is digitally recorded using a Labview program that controls various experimental parameters.
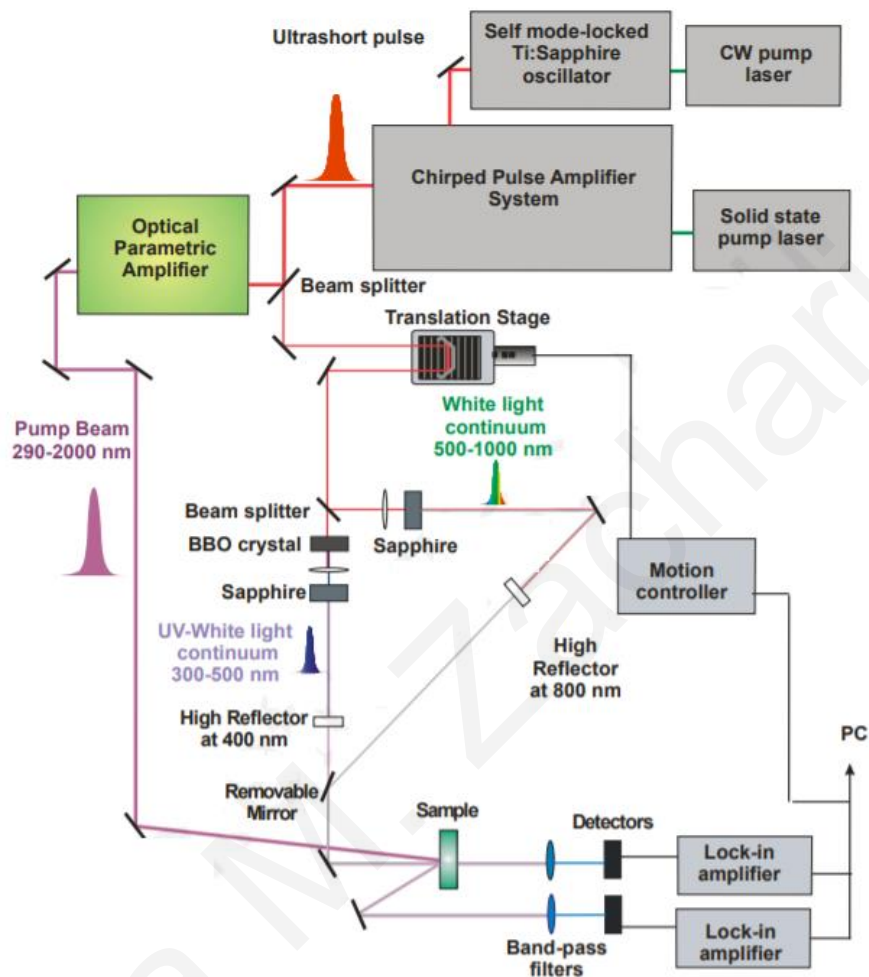
Figure 2.12 Schematic demonstration of the experimental arrangement of the pump probe setup.

3 Size-Dependent Optical Properties of Zn-Shelled CuInS$_2$ CQDs

Copper indium sulfide (CIS) CQDs are promising "green" alternatives to the widely used Cd- or Pb-containing NC systems, as they do not employ such heavy metals while they exhibit attractive optical properties such as high absorption coefficients, long luminescence decay times and high photostability [32]. In the presented work, we performed a comprehensive spectroscopic study of colloidal CIS CQDs employing a Zn-shelling as surface stabilizer. The optical properties of such CQDs were studied, using steady-state and time-resolved photoluminescence techniques in the colloidal and solid state, across the 10-300 K range. The main work objective has been to unravel the impact of (i) quantum confinement and (ii) Zn-shell on the typically multicomponent, broad luminescence of CIS CQDs. The results and a model interpreting the energetics and dynamics of the emission channels in such CIS CQD solids, are presented below.

3.1 Basic Properties of CuInS$_2$ Crystals

3.1.1 Structure of CuInS$_2$ Bulk and Nanoscale Crystals

Bulk CuInS$_2$ typically crystallizes in the tetragonal chalcopyrite structure (CP) shown in **Figure 3.1 (a)**, but CIS in the nanocrystalline form can exist also as hexagonal wurtzite (HW) and cubic zinc blende (ZB). Based on previous work [33] the CQDs involved in the present study, appear to crystallize in the cubic ZB phase.
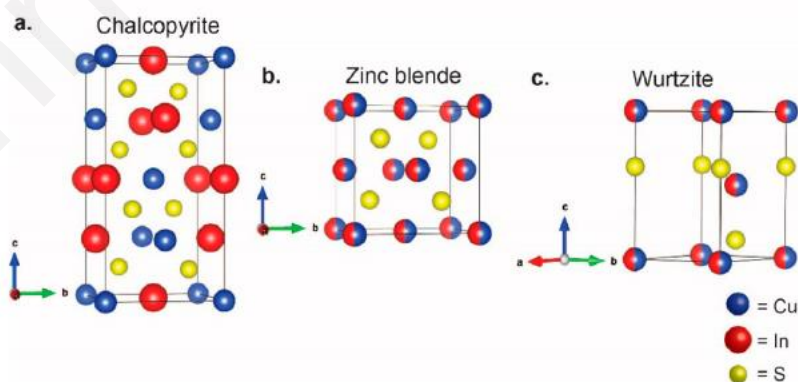
Figure 3.1 Three types of crystal structure of CuInS$_2$: (a) chalcopyrite structure, (b) cubic zinc blende structure, and (c) hexagonal wurtzite structure [32]

CP I−III−VI$_2$ materials exhibit cation ordering. Each S atom surrounded by two Cu and two In atoms with the different bond lengths (RCu−S ≠ RIn−S) cause anion displacement, leading to a tetragonal distortion of the crystal lattice. The characteristic broad emission of I−III−VI$_2$ CP semiconductors is caused by the structural complexity results in a low band gap energy and an abundance of intrinsic defects. Moreover, deviations from 1:1:2 I:III:VI stoichiometry allow the growth of both n-type and p-type NCs, which have been used to increase the efficiency of CIS-based photovoltaics.

The ZB structure is analogous to CP with related lattice parameters but is cation disordered. This cation disordered have the advantage of more flexible stoichiometry (compared to the chalcopyrite structure), due to both cations occupying the same lattice site can easily be exchanged for each other. The flexible stoichiometry allow the growth of both n-type and p-type NCs. The WZ structure is the hexagonal analogue of ZB with both consisting of a close-packed anionic lattice with one half of the tetrahedral interstitial sites filled by cations but the WZ structure is cation ordered. [32]

3.1.2 Electronic Properties of CuInS$_2$ Bulk Crystals

For bulk CIS, the valence band results from the hybridization of Cu d-orbitals and anion p-orbitals while the conduction band is composed of In 5s and S 3p orbitals. (**Figure 3.2**) [34] CIS is typically p-type as the addition of the trivalent element, In^{3+}, to the intrinsic CuS, generates acceptor levels. These acceptor states collect electrons from the valence band, creating holes in the valence band without simultaneously increasing the concentration of electrons in the conduction band. This results in holes becoming the majority carriers, yielding the p-character of the material.
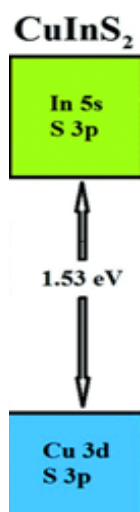
Figure 3.2 Band diagram of CuInS$_2$ bulk [34]

Bulk CuInS$_2$ has a direct bandgap of ~1.53 eV, which matches the optimal spectral range for photovoltaic applications; based on such attribute, the large optical absorption coefficient ($\alpha >$ $10^5\,cm^{-1}$) in the visible [32] and the energy tuning via the quantum confinement, makes colloidal CuInS$_2$ CQDs great materials as solar harvesters for solution processed solar cells. [35]

3.1.3   CuInS$_2$ Colloidal CQDs

Copper indium sulfide (CIS) CQDs are promising alternatives to the most common II−VI QD systems for reasons elaborated above. The Bohr exciton radius of CIS is ~4.1 nm [36], thus, quantum confinement effects have been reported in CIS nanocrystals up to a size of ~8 nm. By changing the sizes of CIS QDs, their absorption and emission can be tuned from the visible to the near infrared region of the optical spectrum, making them promising semiconductor materials for solar cells, light emitting diodes and bio-labelling [37]. The synthesis of ternary materials such as CIS requires adjusting the reactivity of two cationic precursors at the same time, which makes finding optimum reaction conditions and avoiding the formation of undesired side-products more complicated, than in the case of binary compounds. Furthermore, CIS frequently differs from the exact 1:1:2 ratio between copper, indium and sulfur; thus, the stoichiometry of the nanoparticles is an additional parameter, which can be adjusted by changing the conditions of the synthesis and can be used to fine-tune the properties of the resulting material. [36]

CIS CQDs can be synthesized using a variety of metal salts and sulfur sources. Most of the syntheses are conducted in organic solvents. Best size and shape control could be obtained in hot-injection or heating-up procedures. [36] In "hot-injection" and "heat-up" techniques, ligand and metal/ sulfur precursor choice can be used to tune the crystal structure of the resultant NCs. [32] In a ternary system, there are three elements involved in the reaction, and the reaction activity of the reagents related to the three elements should be considered. If the reaction activities of two metal precursors differ from each other, a separated nucleus will be generated and grow into heterostructures or even two compounds. [38] CIS QDs exhibit a wide spectral emission in the visible and near-infrared with large FWHMs in the 200-500 meV range, unlike bulk CIS in which typically a sharp near-band-edge emission around 1.5 eV along with a slightly broader (FWHM ∼20-50 meV) trap emission at 1.4-1.3 eV is observed, as displayed in **Figure 3.3**.
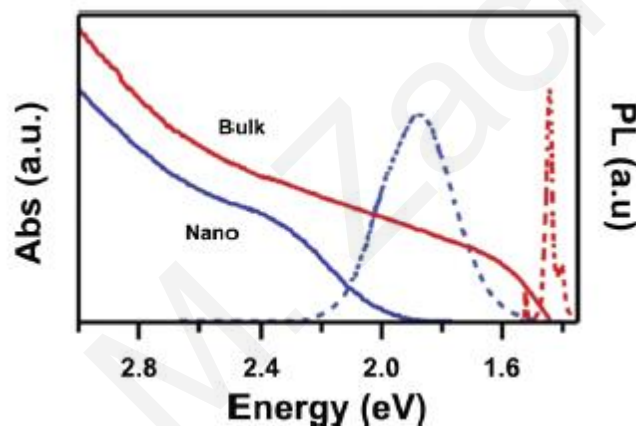
Figure 3.3 Photoluminescence (dotted lines) and Absorption (solid lines) spectra of bulk (red lines) and nanostructured (blue lines) CuInS₂ [39]

The most plausible models of radiative recombination in CuInS$_2$ NCs, displayed in the schematics of **Figure 3.4** are:

    (i)   The donor-to-acceptor (DAP) recombination model [32],

    (ii)   The free to bound channel involving electronic levels and localized intragap carrier states i.e. CB to Localized (self-trapped) Holes or Localized (self-trapped) Electrons to VB transitions [32]

<ol type="i" start="3">
Band-to-band recombination, [31] based on transitions within the intrinsic electronic structure of CuInS$_2$ NCs.
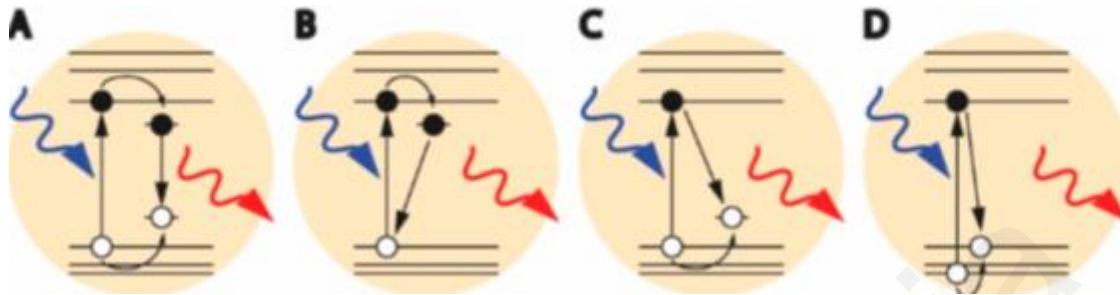
Figure 3.4 The most plausible models of radiative recombination in CIS QDs. (a) Donor - acceptor pair recombination. (b) Localized Electrons to VB (c) CB to Localized Holes (d) Band-to-band recombination. [31]

The donor-acceptor pair (DAP) recombination is supported by the broad emission linewidth, long photoluminescence (PL) lifetimes and the large Stokes-shifts observed. The broad bandwidths can be attributed to a wide distribution of DAP distances within the NC crystals resulting in a concomitant large distribution of the DAP emission energy. On the other hand, the large carrier energetic relaxation following localization in the donor and acceptor states would account for the large Stokes shifts. Furthermore, the reduced overlap between the electron and hole wave functions in combination with the aforementioned wide distribution of donor−acceptor pair distances would result in long and multiexponential PL decays.

Even though the model sufficiently explains some of the main emission characteristics of the CIS QDs, it fails to support the presence of strong size dependence in the PL energies observed. Instead, the size dependent PL energy appears more plausible to originate from the band-to-band or free-to-bound recombination mechanism in which one of the carriers is delocalized in the CB or VB and the other carrier is localized at a defect. [39] [31] The broad PL linewidth and size-independent Stokes shift are inconsistent with the band-to-band model. For free-to-bound mechanism, the quantized nature of the conduction (valence) band electron (hole) explains the size-dependence of the PL energies in terms of the quantum confinement, while the large Stokes shift originates from the energy difference between the top of the valence (conduction) band and the localized hole (electron) state. Based on the extensive studies of the Cu-In-S NC system, the localized carrier is most probably the hole. [31] The hole localized state has been typically

assigned to a Cu^+ ion with the intrinsic $CuInS_2$ crystalline surrounding (**Figure 3.5** (b)), or a Cu-related (**Figure 3.5** (c)) defect (for example, a Cu^{2+} ion neighboring a Cu vacancy or a Cu+ ion in an antisite defect) which may for example be an extrinsic defect, such as a Cu^{2+} on a Cu^+ site (Cu_{Cu}^+) or an interstitial Cu^{2+} (Cu^{2+}_i) neighboring a Cu vacancy (V_{Cu}^-), or a native defect such as a Cu^+-based Frenkel pair ($V_{Cu}^- - Cu^+_i$) or a Cu^+ antisite (Cu_{In}^{2-}), as they are known from bulk $CuInS_2$. The notion that a Cu^- related defect must be involved probably comes from the many defect-related emission lines known from bulk $CuInS_2$. [31]
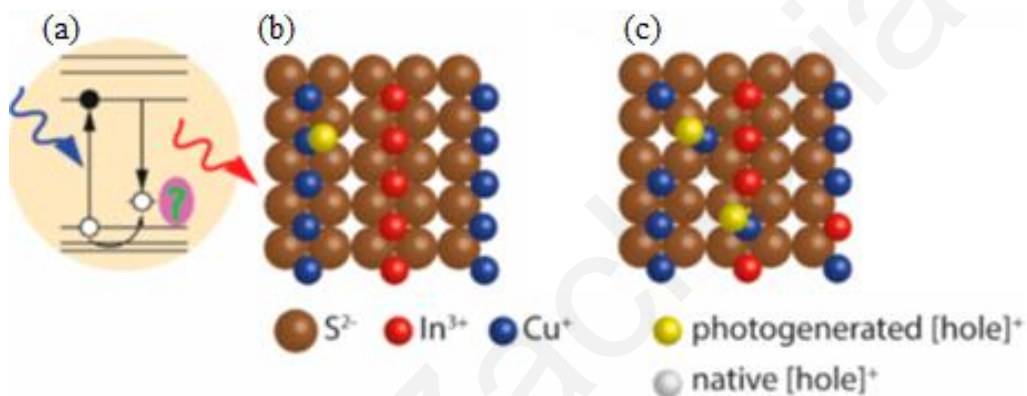
Figure 3.5 (a) Conduction Band to Localized Holes (b) Photogenerated localized hole on a Cu+ ion. (c) Photogenerated localized hole on Cu+ related native defects. [31]

3.1.4 Zn-Shelled $CuInS_2$ CQDs

The Zn-CIS QDs of the present study, were synthesized with the hot-injection method. By varying the injection temperature of the sulfur precursor, at 50°C, 90°C, 130°C and 170 °C, the nanocrystal size was systematically grown, resulting in CQDs solutions with light yellow, orange, red and black colors (**Figure 3.6**), named from now on as CIS 50, 70, 130 and 170 respectively. The procedure was developed by G. Konstantatos group and published in [33]. QD films were spin-casted at 1000 RPM for 30 seconds on quartz substrates out of toluene solutions with a concentration of 25 mg/ml.

Figure 3.6 Toluene solutions of Zn-CIS NCs synthesized at different growth temperatures [33]

The studied CQDs where surface-treated with zinc oleate Zn provides stabilization and surface passivation, resulting in relatively high PL quantum efficiencies that can be retained even after a year [33]. Based on the findings of the previous paper, the effect of Zn-incorporation appears dot size-dependent. X-Ray photoemission (XPS) experiments indicate a non-stoichiometric synthesis of $Cu_xIn_{1-x}S_2$ QDs (In-rich QDs). The zinc replaces more indium for smaller particles (Table 3.1). In larger QDs, Zn appears to bind in the surface providing stabilization while at smaller QD sizes i.e. lower growth temperatures, a partial alloying of the CIS core with Zn is promoted. The passivation process is shown in **Figure 3.7** wherein a copper-deficient core with surface decorated mainly with indium atoms is treated with zinc oleate.

	90 ºC		130 ºC		170 ºC	
	Zn treatment	As synthesized	Zn treatment	As synthesized	Zn treatment	As synthesized
Cu	0.20	0.23	0.33	0.30	0.48	0.50
Zn	0.94	-	0.56	-	0.43	-
In	0.75	1.92	0.9	2.07	0.98	1.36
S	2.11	1.85	2.2	1.63	2.12	2.14

Table 3.1 Composition of CIS CQDs for various synthesis temperatures and Zn treatments [33]
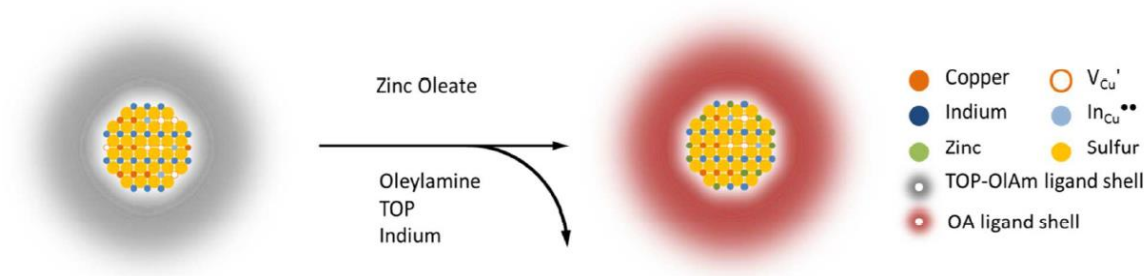
Figure 3.7 Indium decorated copper-poor cores stabilized with TOP and OlAm are treated with zinc oleate [33]

Basic X-ray diffraction experiments indicate that the QD crystal structure is either cubic or tetragonal, with more plausible the first phase that supports the non-stoichiometric content of the QDs. In the Zn-treatment, shifts to higher Q values in XRD peak position (**Figure 3.8 (a)**) occur more prominently with materials synthesized and Zn-treated at lower temperatures. This indicates the formation of disordered Zn-Cu-In-S alloys in the smaller QDs. The line widths of the peak at (111) in wide angle X-Ray diffractograms (**Figure 3.8 (a)**) increase with decreasing synthesis temperature. Wide angle X-Ray diffraction measurements provide estimates for the QD diameters ranging from 2.0 nm to 3.3 nm, using the Scherrer equation. This calculated diameter of 3.3nm agrees well with TEM sizing, providing an average value of 3.2nm (**Figure 3.8 (b)**), showing clear (111) planes. [33].
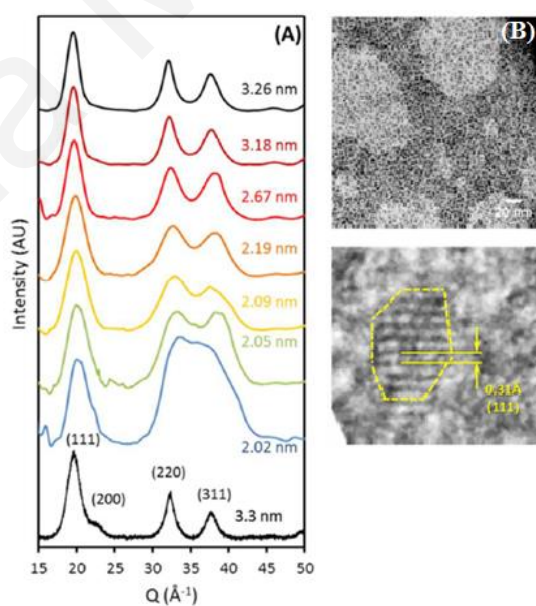
Figure 3.8 Structural properties of CuInS$_2$ nanocrystals. (a) XRD data. (b) TEM micrograph of CIS-ZnOA nanocrystals synthesized at 170 °C, (111) planes shown.

3.2 Optical Properties of CIS QD colloids

The absorption spectra of Zn-CIS QD solutions in toluene with concertation of 1 mg/ml are shown in **Figure 3.9.** The bandgap is obtained by Tauc plots i.e. plots of $(Abs*hv)^2 = f(hv)$ by the interpolation of the linear part of the spectra to $y = 0$. The absorption edge appears to gradually shift from an estimated value of ~2.8 eV for CIS 50 to 2.5 eV for CIS 90, 2.16 eV for CIS 130 and 1.62 eV for CIS170, approaching in the latter case the bulk CIS value of 1.54 eV. The bandgap shift with increasing growth temperature, is consistent with the progressively larger size of the particles produced as the colloidal growth temperature increases. It is noted that the estimation of the band-gap in such QDs yields systematically smaller values as hole levels near the band edge in CIS appear to contribute to the band-edge absorption, as elaborated in [40]. The spectra also contain broad excitonic peaks, whose position is calculated from the second derivative maxima. The exciton peaks appear more pronounced in smaller QDs as the aforementioned hole-induced absorption tails appear to weaken as the QD size decreases. [40] From the energetic difference of the exciton and band-edge positions, large exciton binding energies of 0.2-0.25 eV can be obtained. Such estimates appear overestimated especially at larger QD sizes due to the sub-gap absorption by the hole states that yields underestimated QD gap values, as elaborated above.
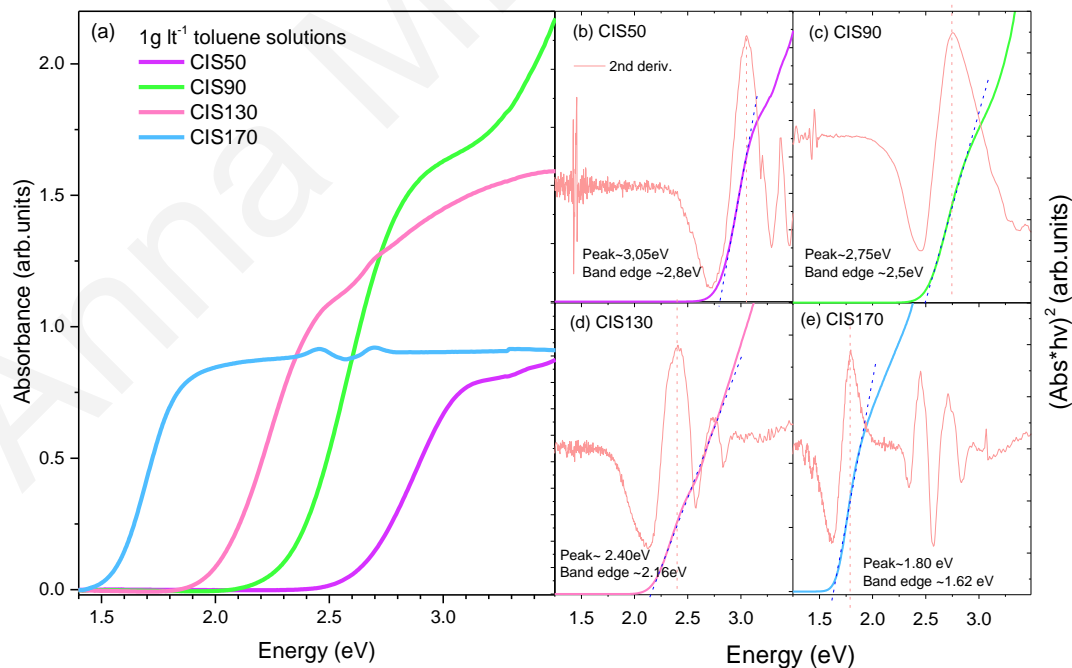
Figure 3.9 Absorbance of Zn-CIS QD solutions. Tauc plots and second derivatives of the spectra are also included, from which the respected bandgap and excitonic peak energies are estimated.

The steady state PL spectra at 300K were measured using quasi-resonant excitation at energies of ~3.1, 2.5, 2.3, 1.9 eV for CIS 50, 90, 130, and 170 respectively. **Figure 3.10** contains representative comparative and normalized PL data along with the integrated PL variation. The integrated emission increases as the particle size increases before getting significantly quenched for CIS170, possibly due to the loss of quantum confinement. Despite the stronger confinement, CIS 50 exhibits less bright luminescence compared to CIS 90 and 130, while it yields by far the larger FWHM compared to the other samples. Furthermore, the Stokes shift monotonically and dramatically decreases from ~0.8 to ~0.04 eV as QD size increases. The significant larger Stokes shift values in small QDs can be attributed to a non-uniform incorporation of Zn. All the above trends, are consistent with increased disorder in the smaller CIS QDs due to the formation of a disordered quaternary CIS-Zn alloy [41] rather than a Zn shell.
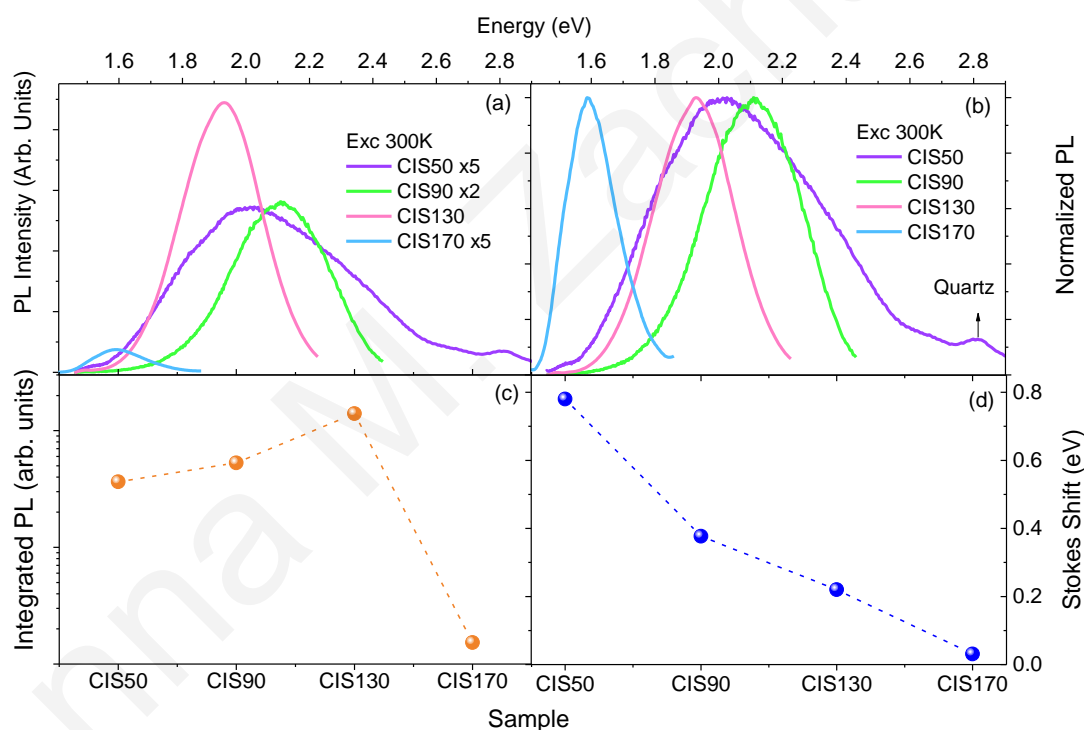
Figure 3.10 a) Comparative PL and b) Normalized PL spectra of CIS CQDs solutions at 300K. c) Integrated PL and d) respective Stokes shifts are also displayed.

3.3 Optical Properties of Zn-CIS QD films

The absorbance for spin-casted CIS QDs films is shown in **Figure 3.11** along with Tauc plots from which the bandgap is estimated. As in the solution data, broad excitonic peaks are observable, becoming less crisp as the QD size increases. The excitonic peak and the QD band-

edge at CIS 50 and 90 shifts to slightly longer wavelengths compared to the respective solutions, attributed to additional interactions in the solid state. For CIS 130, the band-edge of QD solutions and films appear to match, while for the bulk-like CIS 170, a non-expected blue shift of the band edge is consistently observed in films compared to the solutions gap values.
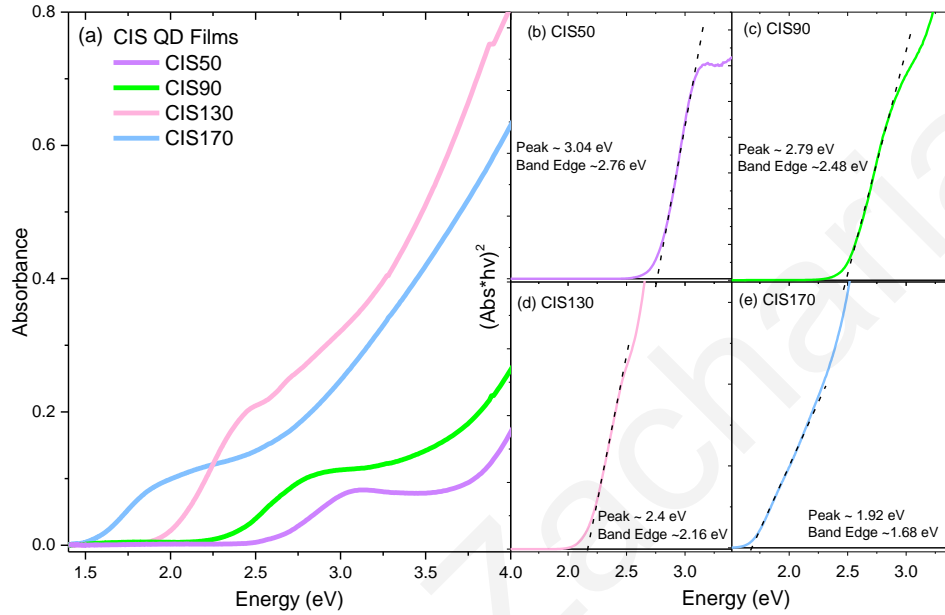
Figure 3.11 Absorbance spectra and Tauc plots of spin-casted films of the four CIS QD samples.

Normalized PL spectra at 300K of the Zn-CIS CQD films are displayed in **Figure 3.12 (e).** The films exhibit broad, multi-component emission with CIS 50 showing the broader linewidth, in agreement with the QD solution data. **Figure 3.12** contains also the results of a Gaussian lineshape analysis of the multi-peak PL spectra from the films. Three Gaussian peaks are required to provide an adequate fit of the PL lineshape for CIS50, CIS90, CIS130, while the bulk-like CIS170 films can be fitted by two Gaussian peaks. The fits cannot support such monotonic shift. Instead the lineshape analysis yields for the quantum-confined CIS50, CIS90, CIS130 QD films similar, within the fitting margin of error, peak 1,2,3 energies, with only the relative intensity varying between samples. For films CIS50 and 90, the high energy peak 3 appears to have the higher relative contribution while its amplitude reduces substantially in the CIS 130 film. **Figure 3.12 (f)** displays the energetic separation of the absorption edge, obtained from Tauc plots, with the PL peak 1,2 and 3 for all films. The separation strongly decreases as

QD size increases, as the absorption edge red-shifts while the Gaussian PL peaks do not vary much with QD size.
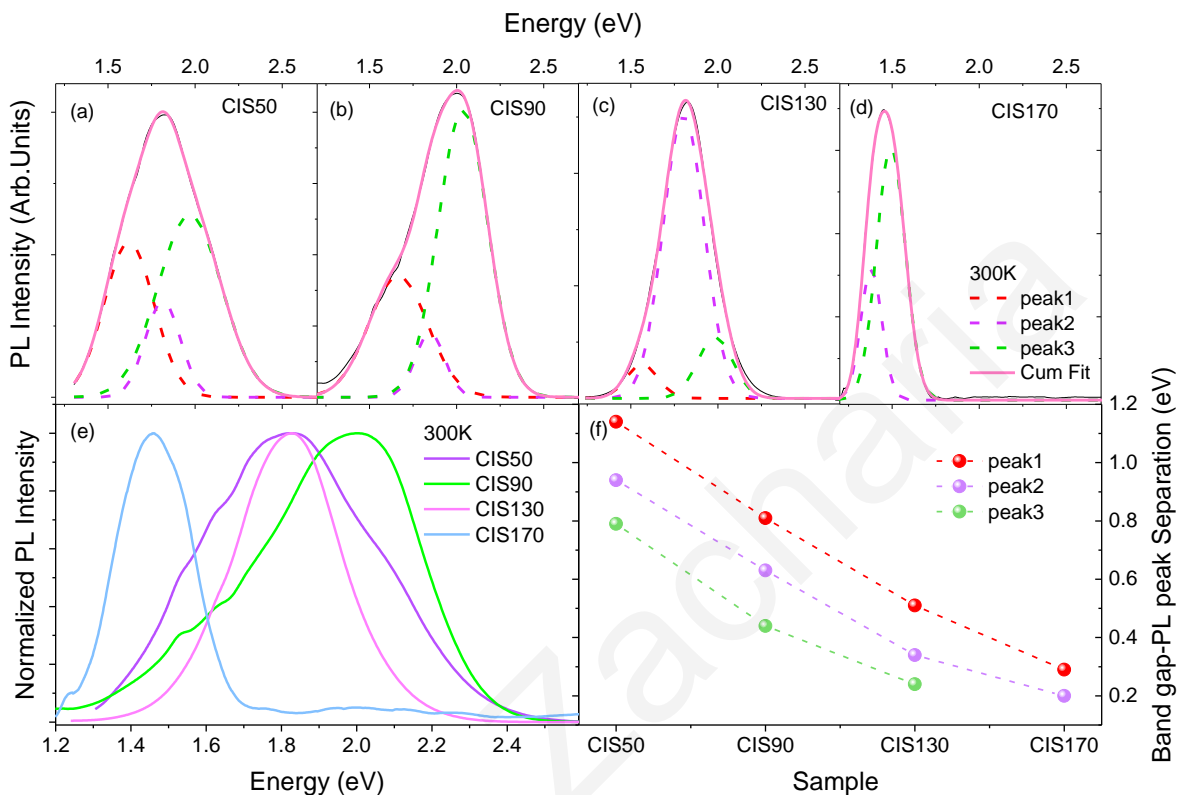
Figure 3.12 Gaussian lineshape fitting of the room temperature PL spectra of (a) CIS50, (b) CIS90, (c) CIS130, (d) CIS170, (e) Normalized PL spectra of CIS CQDs films at 300K and (f) Band gap – Gaussian PL peak separation for CIS50, CIS90 and CIS130 films.

Figure 3.13 displays the temperature-dependent PL spectra of the four CIS films in the 10 to 300 K range. Cooling was provided by an optical closed-cycle refrigerator and excitation by a 375 nm (~3.1 eV) laser diode system with a constant excitation density of ~25 mW/cm^2. The temperature-activated competition of the three Gaussian contributions is readily visible in the CIS90 film, and to a lesser degree in the CIS 50 film, with the relative emission at low energies quenching as the temperature rises at the expense of the high energy PL contribution.
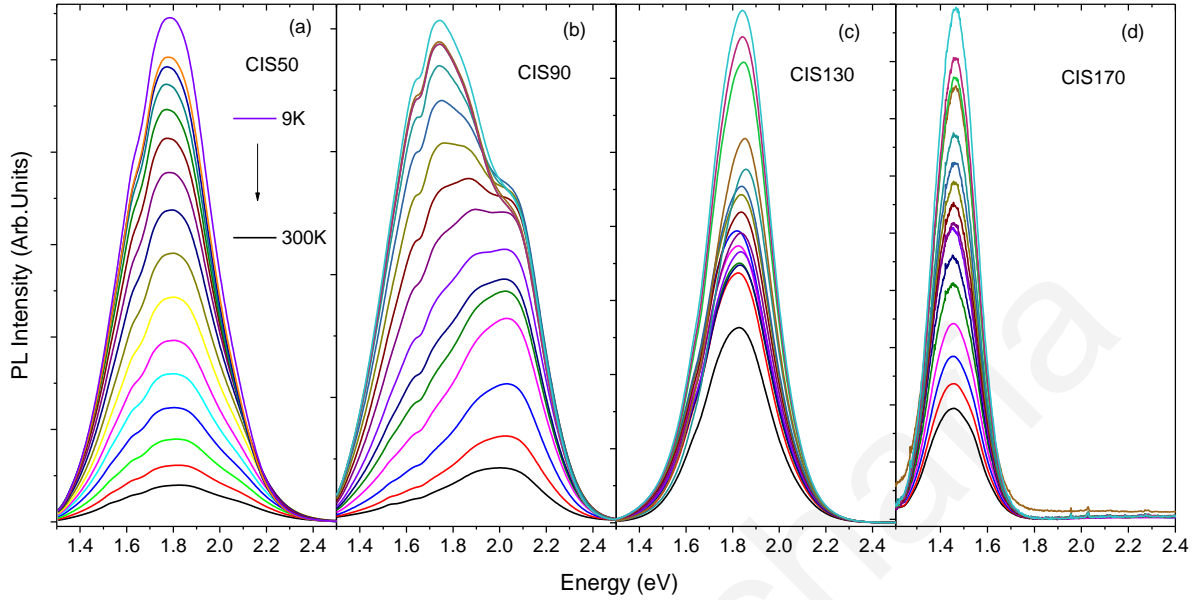
Figure 3.13 Temperature-dependent PL spectra of the spin-casted CIS QD films in the 10-300 K range

Figure 3.14 contains the results of a Gaussian lineshape analysis performed for a temperature evolution of the PL spectra of CIS QD films. The large energetic separation of peak 3 from the experimentally estimated band-edge making unlikely the assignment to band-to-band transitions. Most probably the peak is associated with free-to-bound transitions i.e. recombination of electrons in the conduction band with localized holes in states above the valence band edge. [42] [43]The integrated emission intensity I(T) of peak 3 is plotted at **Figure 3.14** as a function of temperature and fitted via the following modified Arrhenius function [44] [45]:

$$I(T) = \frac{I_0 + I_1 e^{-(\Delta E/k_B T)^2}}{1 + A e^{\frac{-E_{AC}}{k_B T}} + B(e^{\frac{E_{LO}}{k_B T}} - 1)^{-m}} \qquad 3.1$$

Here I_0 is the PL Intensity at zero temperature and I_1 is the PL contribution due to excitons that are thermally de-trapped from shallow traps of barrier ΔE assuming a Gaussian trap site energy distribution. E_{AC} and E_{LO} are the acoustic and optical phonon energies with m being the average number of LO phonons involved in the exciton-LO phonon interaction. A and B are the amplitudes of each term. In agreement with studies on CIS, the fit yields E_{LO} in the range of

50

~15-16 meV for all films while a fixed average acoustic phonon energy of 6.5-7 meV is extracted. [46]
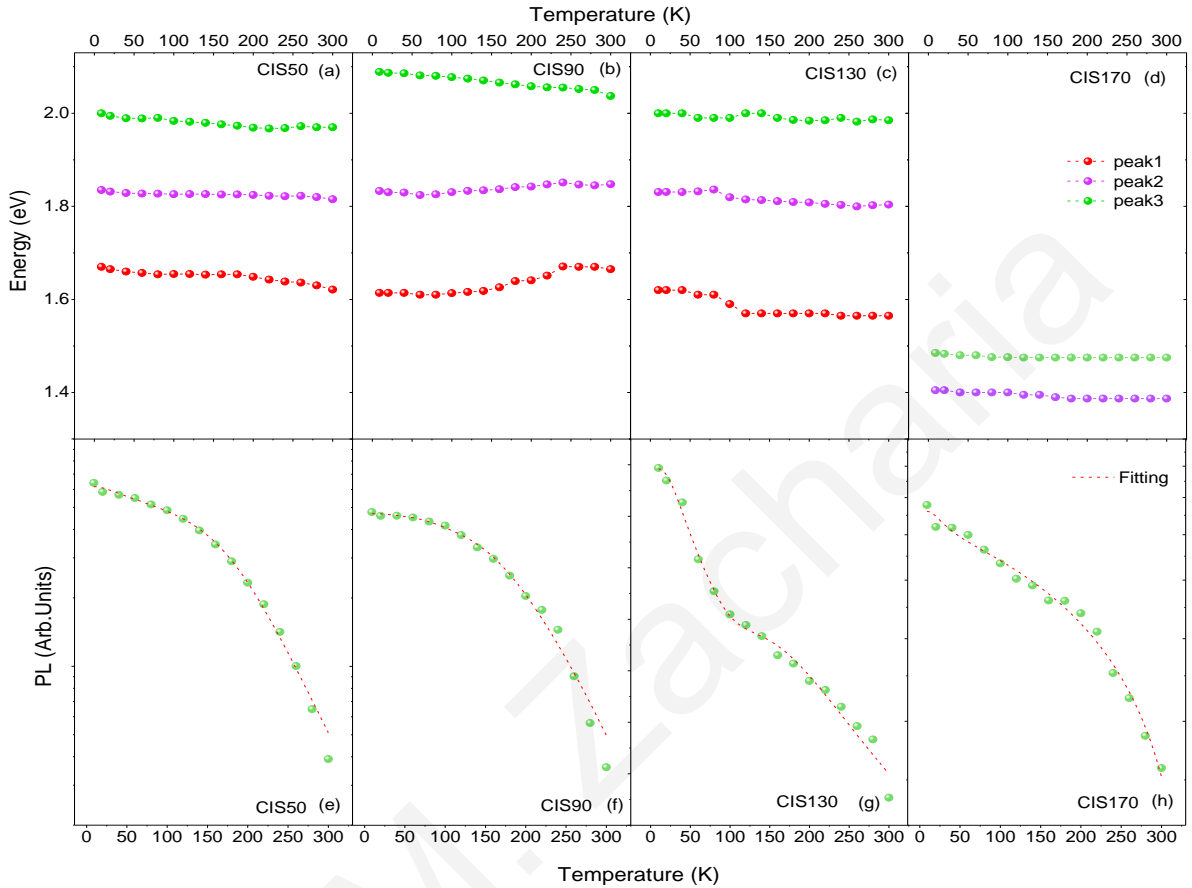
Figure 3.14 Results of a Gaussian lineshape analysis performed at each PL spectra for the confined QDs of a) CIS50, b) CIS90, c) CIS130 and d) CIS170. Arrhenius plots of the PL peak 3 in the c) CIS50, d) CIS90, c) CIS130 and d) CIS170 films. **The dashed line displays the** *Arrhenius model fit curve.*

As expected, the number of optical phonons that are required to activate quenching of excitons via phonon-assisted thermal escape processes decreases with NC size i.e. as carrier confinement energy reduces, as shown in Table 3.2. Using an average LO phonon energy of 15 meV, the thermal-escape carrier barrier of CIS50, CIS90, CIS130 and CIS170 is roughly estimated equal to ~45, ~30, ~30 and ~15 meV, respectively. Furthermore another consistency with NC size is observed with the exciton detrapping processes from surface states with the relevant barrier ΔE monotonically decreasing as confinement reduces. The values extracted for CIS50, CIS90, CIS130 and CIS170 are ~20, ~18, ~13 and ~8 meV. The trend is reasonable, as surface traps are expected to deepen as QD size is decreased.

Sample	ΔE (meV)	EAC (meV) ±1	ELO (meV)	m
CIS50	20	6	15	3
CIS90	18	6	15	2
CIS130	13	6	15	2
CIS170	8	6	15	1

Table 3.2 Results of the Arrhenius plot fit of the free exciton transition (peak 3) for CIS50, CIS90, CIS130 and CIS170 films.

A PLE study at 300K was also performed to further probe the origin of the three emissive channels in the CIS50, CIS90 and CIS130 films. The work was performed monitoring the spectral region of the PL in the vicinity of the respective three Gaussian peaks. The results of such study are displayed in **Figure 3.15,** containing a comparison of the spectral characteristics of the PLE and absorbance spectra from each film. It can be observed that PLE spectra monitoring the high energy peak 3 exhibit a slightly broader lower energy tail compared to the other PLE spectra and the absorbance. The trend becomes pronounced in CIS90 film, in which the PLE spectrum at peak 3 is clearly red-shifted by few hundreds of meVs compared to the other PLE spectra and the absorbance peak. A slightly smaller (~100 meV) but visible bathochromic shift of the PLE at peak 3 compared to the absorbance is also visible at CIS 130. The PLE spectra monitoring peaks 1 and 2 do not exhibit such distinct features in the vicinity of the band-edge. The main outcome of the PLE study is that CQD photoexcitation species responsible for the high energy peak 3 can be excited via sub-gap light. This appears compatible with our initial assignment of the peak to a free (most probably electron) to localized (most probably self-trapped hole) transition, as sub-gap excitation in such cases can provide resonant excitation of such transition. On the other hand, below-gap excitation of the DAP is inefficient due to the small density of states and the wide energy distribution of such defects. It is thus quite probable that the deep level emission of peaks 1 and 2 originates on D-A pairs that are populated via energetic relaxation from band-edge states, based on the spectral resemblance of the respected PLE spectra and the films absorbance.
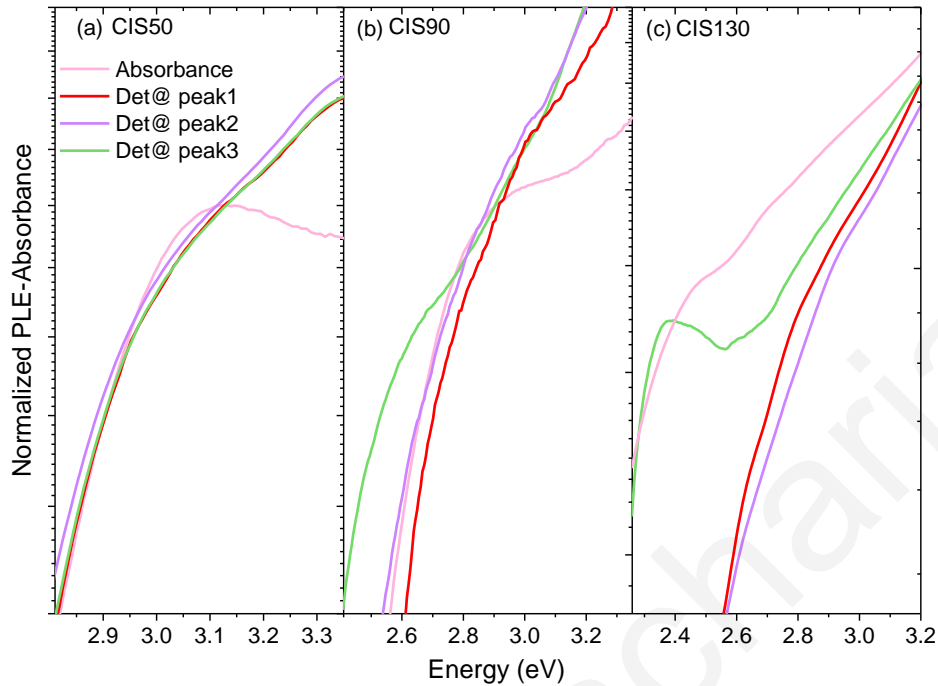
Figure 3.15 PLE spectra of (a) CIS50,(b) CIS90 and (c) CIS130 films at 300K

Further information is provided by the PL dynamics of the Zn-CIS QD films measured with the TCSPC method. The samples were excited by a 375 nm laser diode with pulse width of ~150 ps. **Figure 3.16** contains the PL average lifetime of the 3 quantum-confined CQD samples across the 78-300K range, monitoring the three PL peak contributions. At room temperature, the average PL lifetime decreases monotonically as the growth temperature increases. Typically transitions involving one or two electronic states are expected to exhibit larger recombination rates i.e. shorter PL lifetimes compared to defect-mediated transitions due to the typically higher density of states of the electronic states. The PL lifetime of peak 3 is indeed shorter and appears significantly less temperature dependent than the peaks of 1, 2 in all three CQD films which is consistent with the three peaks assignment. [38] [47]
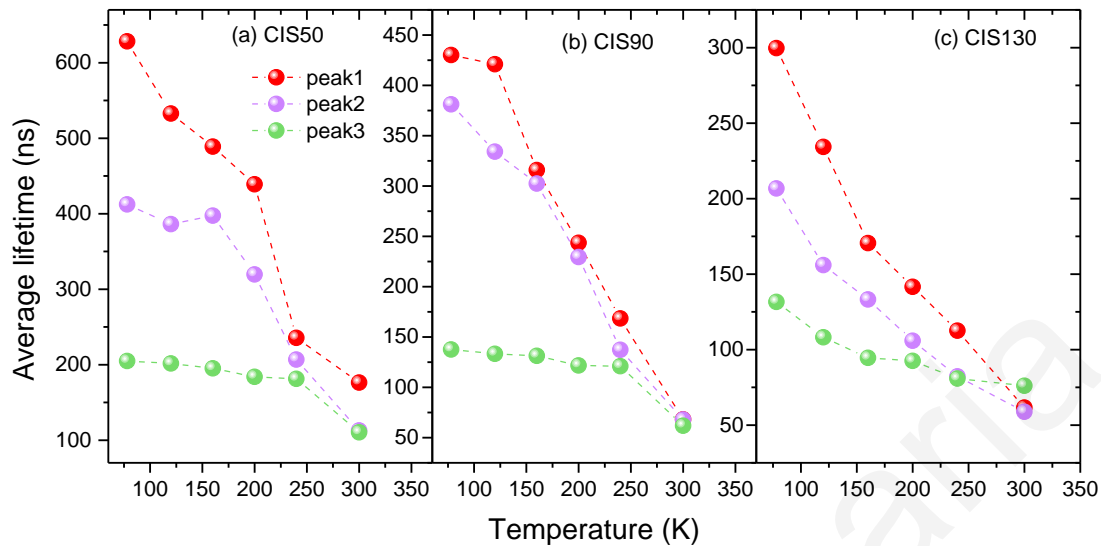
Figure 3.16 Average PL lifetime vs Temperature of the three Gaussian PL contributions in the (a) CIS50 (b) CIS90 and CIS130 Films.

3.4 Chapter Conclusions

Insight into the size-dependent optical properties of solutions and films of CIS QDs passivated by Zn is provided. A red shift of the gap with the QD size was observed due to reduction of quantum confinement, while large Stokes shifts and linewidths combined with weaker emission may indicate the formation of disordered Zn-Cu-In-S alloys in the smaller QDs probed. The PL temperature-dependent data indicate the presence of thermally-activated de-trapping process that feed the high energy emissive species of peak 3 by the lower energy photoexcitations of peak 1 and 2. Based on the evidence provided by the steady-state and time-resolved photoluminescence, the high energy peak 3, appears to originate from excitations slightly below the band-edge; it is tentatively assigned to a free to bound type of transition, most probably from the conduction band to localized holes below the valence band edge. On the other hand peaks 1 and 2 are more probably associated with defect states i.e. D-A pairs that are populated via relaxation from band-edge states.

4 Spectroscopic Studies of PLD-grown CuInGaSe$_2$ and CdS Thin Films for Solar Cell Applications

Pulsed laser deposition (PLD) of CuIn$_{1-x}$Ga$_x$Se$_2$ (CIGS) provides a low cost, single-step process via which stoichiometric, high quality thin films for light harvesting applications can be produced. Recently the group of J. Giapintzakis has demonstrated the potential of producing high-quality, nearly stoichiometric PLD-grown CuIn$_{0.7}$Ga$_{0.3}$Se$_2$ films using a systematic investigation of the PLD growth parameters [22]. In the aforementioned publication, the room temperature optical properties of such films were preliminary assessed. The work was followed-up by a more detailed luminescence investigation of the PLD grown CIGS films [48], in which sample temperature has been implemented as the varying experimental parameter along with Gaussian lineshape analysis that allowed us to monitor the energetics and dynamics of the various emissive channels providing a mapping of the electronic and defect structure of PLD-grown CIGS films. Such studies are important, as PLD synthesis results in films with particular structural and morphological characteristics yet no fundamental spectroscopic studies have been performed to provide an insight into the optical properties of PLD-deposited CIGS and how they compare with the respected properties of the well-studied evaporated or sputtered CIGS films. The work on this chapter is completed by a preliminary photololuminescence study of PLD - grown CdS thin films deposited on soda-lime glass under various growth temperatures. These results are useful for the ambitious task of demonstrating PLD grown, CIGS-based solar cells; such cells will be fabricated in the typical p-n junction configuration consisting of molybdenum (Mo) as the bottom electrode, CIGS thin film as the absorber layer p-type, CdS thin film as the buffer layer n-type, and intrinsic zinc oxide (i-ZnO) and Al-doped ZnO (AZO) layers as the window layers. [49] **Figure 4.1** shows the schematic diagram of the targeted CIGS solar cell structure.
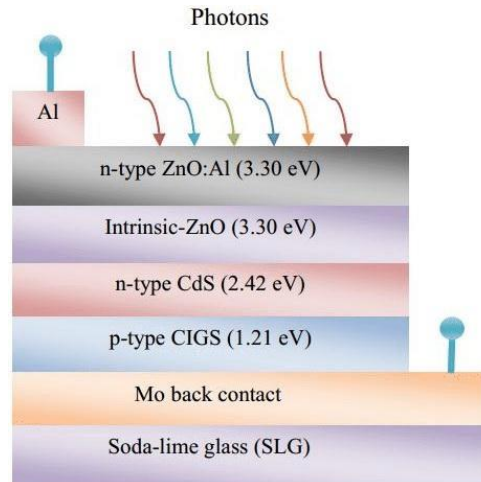
Figure 4.1 Targeted CIGS solar cell structure to be produced via PLD [50]

4.1   Basic Properties of CuInGaS$_2$ Crystals

Copper indium gallium (di)selenide (CIGS) is a I-III-VI$_2$ semiconductor material composed of copper, indium, gallium, and selenium with a chemical formula of CuIn$_x$Ga$_{(1-x)}$Se$_2$. The bandgap varying continuously with *x* from about 1.0 eV (for copper indium selenide) to about 1.7 eV (for copper gallium selenide). CIGS is a tetrahedrally bonded semiconductor, with the chalcopyrite crystal structure. [51]
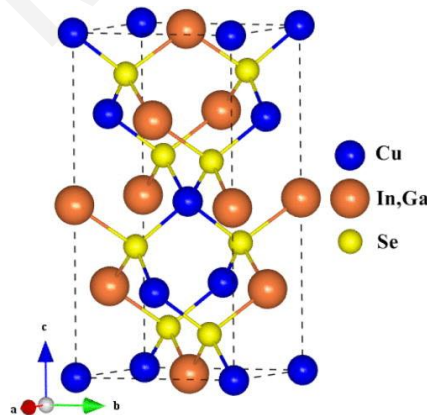
Figure 4.2 Crystal structure of the chalcopyrite CIGS [52]

Chalocopyrite MCS and mainly CuIn$_{1-x}$Ga$_x$Se have been extensively studied in recent years because of their high power conversion efficiency, which is higher than of other promising

materials used for thin film photovoltaic devices, such as CdTe, CuS, and $PbSe_xS_{1-x}$. [53] CIGS possesses controllable band gap energy of 1.1 to 1.4 eV and high optical absorption coefficient of $>10^5$ cm^{-1} making it possible to reduce effectively the thickness of the photoabsorber layer. [54] Electrical properties such as carrier concentration and mobility are also important for realization of high-efficiency solar cells. [54] For CIGS, the valence band results from the hybridization of Cu d-orbitals and anion p-orbitals while the conduction band is composed of In 5s and Ga 4s orbitals (**Figure 4.3**). It is typically p-type and exhibits good electrical conductivity properties. [55]
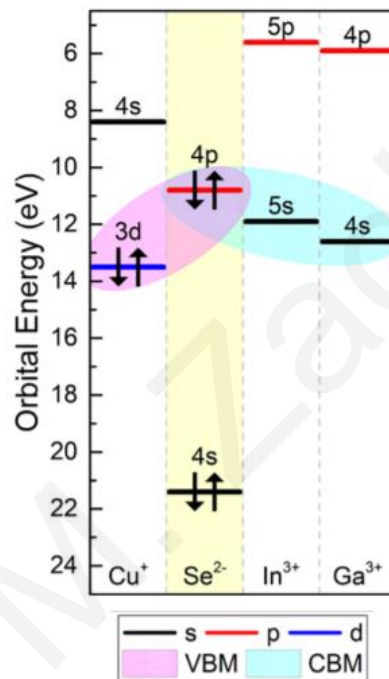
Figure 4.3 Schematic of the valence and conduction band for CIGS [55]

Regarding their emission properties, CIGS exhibit broad luminescence in the near-infrared with large FWHMs of few hundreds of meV. Little is known for the emission properties of PLD-grown CIGS; an example from one of the few literature reports is provided in **Figure 4.4.** The figure contains the PL spectrum of nanosecond-PLD CIGS at 15 K. The weak PL peak at 1.2 eV is assigned to the band-to-band transition while the dominant contribution at lower energies are attributed to different radiative defect-related transitions.
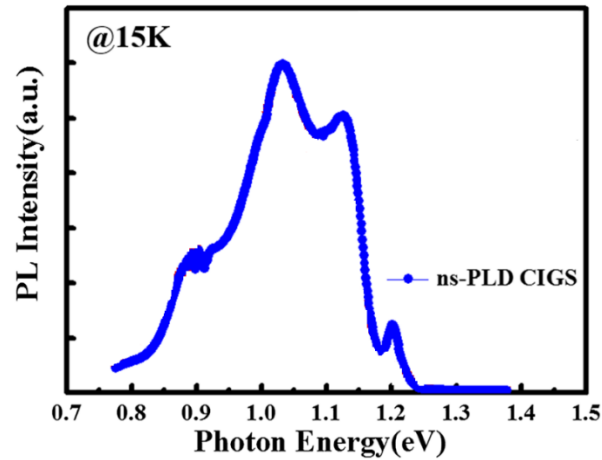
Figure 4.4 Example of low temperature (15K) PL spectra from ns-PLD CIGS thin films. [56]

The broad emission predominantly arises from multiple optical transitions involved in the luminescence process. PL has been thoroughly studied in thin films of CIGS produced via established evaporation, sputtering and epitaxial techniques. It has been found that the photoluminescent properties depend strongly on the CIGS stoichiometry. [57] Irrespective though from stoichiometry the radiative recombination in CIGS appears to be dominated by sub-gap defect recombination mainly in the form of DAP (donor-acceptor pairs). Some of the most quoted defect states contributing to the CIGS emission are Cu vacancies (V_{Cu}), typically acting as shallow donors, Se vacancies (V_{Se}) mainly acting as shallow acceptors and deep level In antisite (In_{Cu}). [58] There is a consensus in the literature that the emission can be described by a combination of the DAP and band-to-band recombination. A model example for the emission from evaporated CIGS films is displayed in the **Figure 4.5**, below. The participated donor and acceptor states were assigned to anion vacancy (V_{Se}) defects, and copper vacancies (V_{Cu}) or Indium vacancies (V_{In}), respectively. [59] In addition to defect-based emission, the band-edge high energy PL contribution is observed.
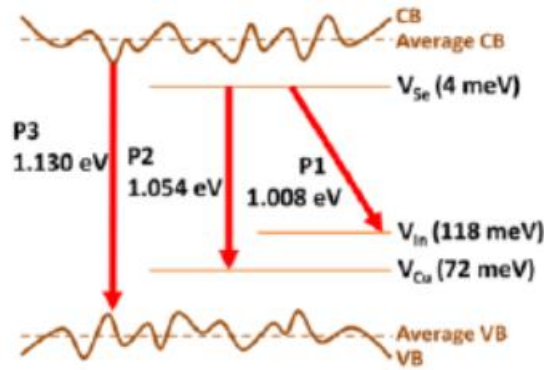
Figure 4.5 An example of the emission channels involved in evaporated CIGS thin films. [59]

4.1.1   Solar Cell Applications

$CuIn_{1-x}Ga_xSe_2$ has been extensively studied in recent years as solar harvesting material owing to its material robustness, direct energy bandgap and strong absorption covering the visible and a fraction of the near-infrared solar light spectrum [60] [61]. As photo-absorber material it exhibits high absorption coefficients of about $10^5\,cm^{-1}$ over most of the visible solar spectrum, thus absorber thicknesses of about 2 μm are sufficient, which offers a low-cost perspective for industrial production (in contrast, crystalline Si solar cells need as much as 100 times thicker absorbers owing to the lower absorption coefficient of Si). [54] CIGS has the additional advantage of being able to be deposited on flexible substrate materials, producing highly flexible, lightweight solar panels. Improvements in efficiency have made CIGS an established technology among alternative cell materials. The high prospect of CIGS for thin film solar cells has been recently confirmed by the achievement of one of the highest efficiencies of 22.6% among all thin film solar cells at the laboratory level. [62]

4.2   PLD-Deposition of CIGS films

High quality CIGS films are typically fabricated via thermal co-evaporation [63] and sputtering techniques [64] however both of them exhibit certain drawbacks. In general, co-evaporation is difficult to control due to variations in the elemental fluxes resulting in lack of stoichiometric reproducibility. [65] The co-evaporation process consists of evaporating Cu, In, Ga, and Se pure elements through a three-stage process. The sputtering process, on the other hand, synthesizes the CIGS absorber layers via a two-step process, including the fabrication of a metallic precursor

59

layer and postselenization. Both of the methods require a high-vacuum environment and precise control during deposition. [53] Pulsed laser deposition (PLD) is an alternative, relatively simple and low cost method that achieves good transfer of stoichiometry of the target composition [23]. PLD has been used to grow high quality, complex compounds containing as many as five or six elements; [66] yet its use in the fabrication of CIGS films is rather limited with plenty of room for optimization.

In the presented work, CIGS films were deposited on soda-lime glass (SLG) substrates by PLD using a KrF excimer laser source ($\lambda = 248$ nm, $\tau \leq 25$ ns) in a high-vacuum chamber. The laser beam was driven through an arrangement of mirrors and focused by a focal lens on a polycrystalline $CuIn_{0.7}Ga_{0.3}Se_2$ (Testbourne) target at an incident angle of 45° inside the chamber. The target rotation during the irradiation ensured a uniform ablation of the target surface. The substrate was placed parallel to the surface target at a fixed distance of 4.5 cm. The deposition was carried out in the presence of background gas after the chamber was evacuated at a base pressure of 4×10^{-6} mbar. Argon (Ar) was used as background gas to confine the plume. The number of pulses and the repetition rate were kept constant at 6000 and 10 Hz respectively, for all depositions. Laser fluence, Ar background pressure and substrate temperature were systematically investigated in order to achieve the optimum growth conditions for high quality CIGS films. The assessment of the previous investigations related to fluence and background gas pressure have led to the selection of 1 J/cm^2 and 0.01 mbar, respectively. All studied films are nearly stoichiometric with composition of $CuIn_{0.7}Ga_{0.3}Se_2$, and have been deposited at substrate temperatures in the range of 20 $^{\circ}$C (ambient lab temperature) to 500 $^{\circ}$C. [48]

4.3 Structural Properties of PLD-grown CIGS

Figure 4.6 shows the compositional ratios of the films deposited at various substrate temperatures determined via energy-dispersive X-ray spectroscopy. As the figure indicates, all films are nearly stoichiometric independently of the deposition temperature, with slightly In-excess and Ga-deficiency with respect to the target stoichiometry. Specifically, the stoichiometry of the films is $CuIn_{1-x}Ga_xSe_2$, with x~0.26.
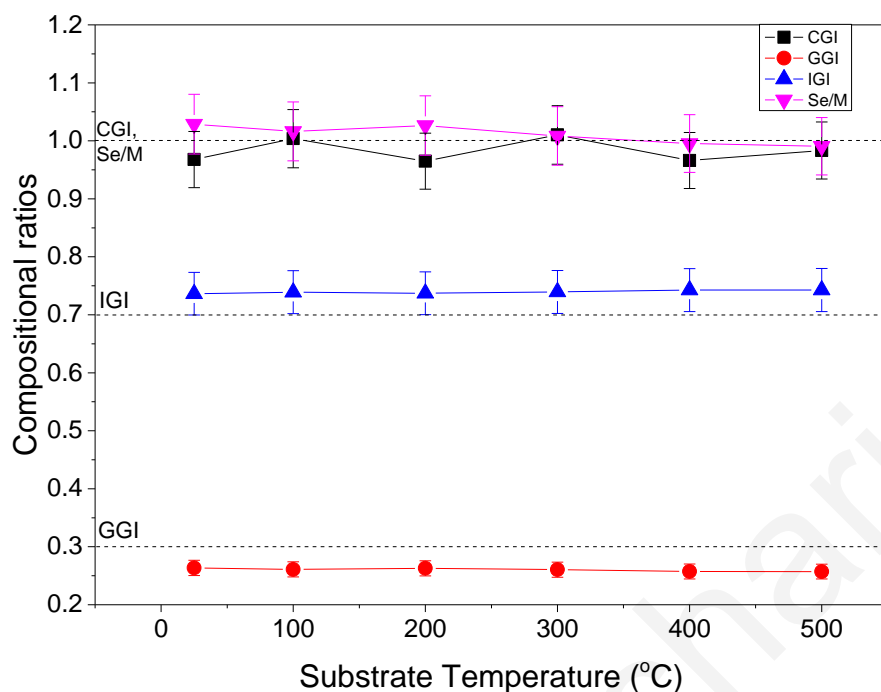
Figure 4.6 Compositional ratios of CIGS thin films deposited on SLG substrates at various substrate temperatures. Dashed lines indicate the ratios of a stoichiometric film, being CGI=Cu/(Ga+In)=1, GGI=Ga/(Ga+In)=0.3, IGI=In/(Ga+In)=0.7 and Se/M=Se/(Cu+Ga+In)=1. All films are stoichiometric in respect to the target stoichiometry. [22]

Grazing incidence X-ray diffraction (GIXRD) patterns of the films are shown in **Figure 4.7** in a logarithmic scale. All deposited films exhibit seven diffraction peaks identified as (1 1 2), (2 2 0)/(2 0 4), (3 1 2)/(1 1 6), (4 0 0)/(0 0 8), (3 3 2), (4 2 4), (5 1 2) planes of $CuIn_{0.7}Ga_{0.3}Se_2$ chalcopyrite phase, with (1 1 2) peak being the most prominent. An additional very-low intensity peak at $\sim 25.6°$, is attributed to the Cu_2Se secondary phase, observed mainly on films grown at low PLD temperatures. The $Cu_{2-x}Se$ peak becomes less intense as the deposition temperature increases and eventually disappears on films grown at 500 °C. As the substrate temperature increases, the surface mobility of the ablated species increases, regardless of the atomic mass, and the single CIGS chalcopyrite phase is obtained. **Figure 4.7** shows also that the position of the (1 1 2) peak shifts to higher 2θ angles as the deposition temperature increases. Specifically, the (1 1 2) peak shifts from 26.72° to 26.92° as the substrate temperature increases from room temperature to 500 °C. The shift of the Bragg angle towards the stoichiometric bulk value of chalcopyrite CIGS (2θ=26.92º) indicates the relief of strain in the films crystal structure. This observation is reinforced by the fact that the films grown at room temperature and at 100 °C

underwent delamination a few hours after deposition. Similar results have been reported previously [54] [53]. The aforementioned experiments were performed and analyzed by Christiana Nicolaou and published in [22].
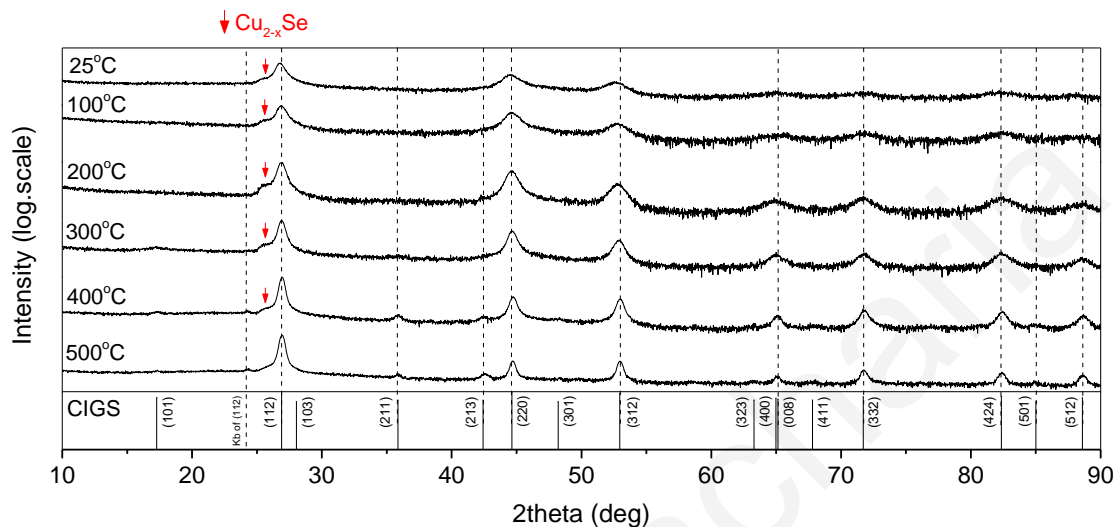
Figure 4.7 XRD patterns (10°–90°) of CIGS thin films deposited on SLG substrates at different substrate temperatures. The bottom plot shows the XRD pattern of CuIn$_{0.}$7Ga0$_{.3}$Se$_2$. The secondary phase of Cu$_{2-x}$Se is indicated by the arrows. The Cu$_{2-x}$Se peak gradually fades as the deposition temperature increases. The (1 1 2) peak shifts towards the stoichiometric bulk value of chalcopyrite CIGS. [22]

4.4   Optical Properties of Pulsed Laser Deposited CuInGaSe$_2$ Films

The light harvesting ability of the PLD-grown CIGS films was evaluated by the magnitude and spectral variation of the absorption coefficient, which was estimated by optical transmission and reflectivity experiments. The absorption coefficient in the range of 0.8 to 2 eV for CIGS films grown at various substrate temperatures is displayed in the graphs of **Figure 4.8.**
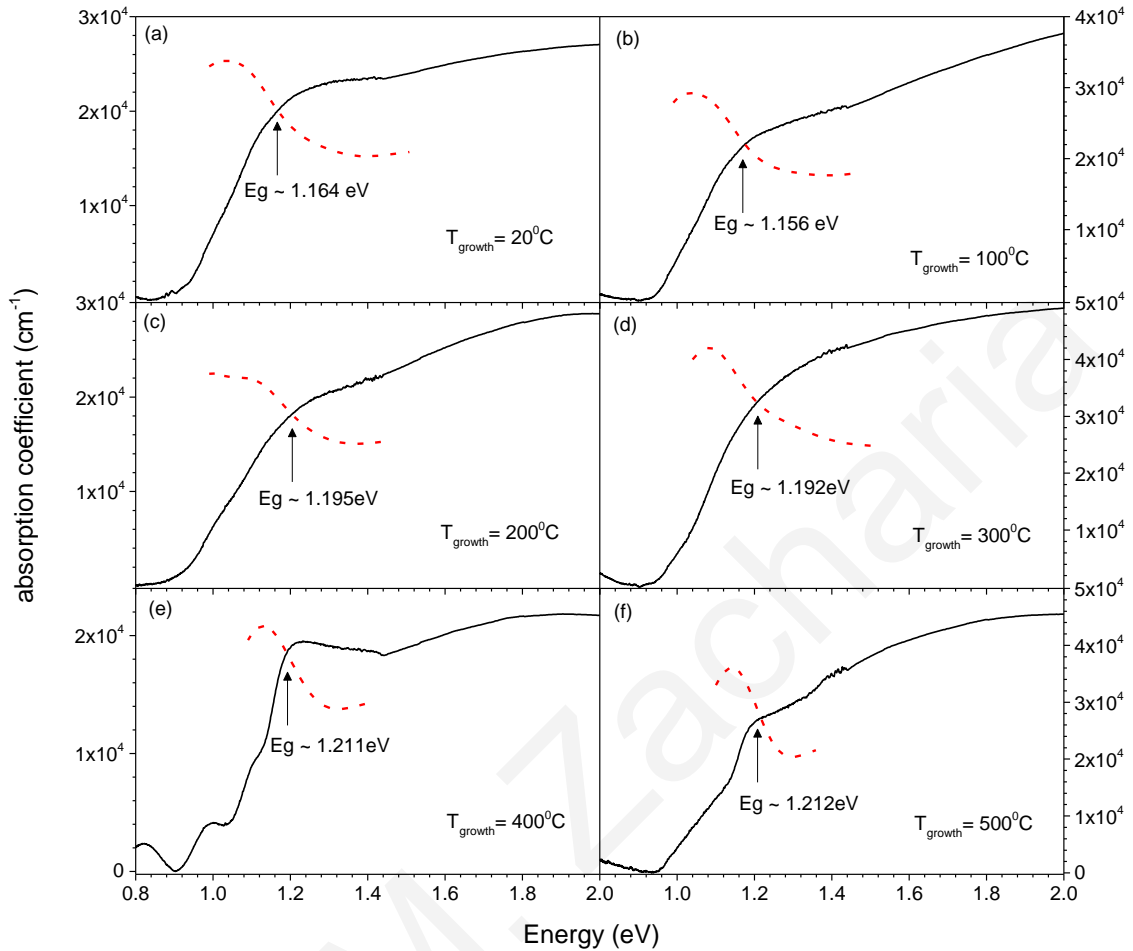
Figure 4.8 Spectral variation of the absorption coefficient of CIGS films grown at various substrate temperatures. The first derivative of the absorbance and the estimated energy gap for each film is also shown. [22]

The films exhibit high absorption coefficients of $\sim 2\text{-}3*10^4$ cm^{-1} in the vicinity of the band-edge standing in par with coefficients of previously reported module-ready CIGS [67] and recently demonstrated PLD-grown CIGS thin films. [66] [56] A recent publication [68] reports on higher absorption coefficients in PLD-grown CIGS thin films, surpassing 10^5 cm^{-1} in the visible; however, such values appear artificially inflated as the optical absorption measurements do not account for the significant light scattering losses at the films' surface.

In the latter report, the influence of deposition temperature on the absorption coefficient is also investigated, demonstrating a reduction of the absorption coefficient and an increase of the band gap energy (E_g) as substrate temperature increases. In our studies, we have not observed a

correlation of the optical absorption strength with the substrate temperature; on the other hand, a systematic blue shift of the band gap energy with deposition temperature is indeed observed, as shown in **Figure 4.9**. A systematic temperature-dependent variation of the stoichiometry has to be excluded as a possible origin of the effect based on the EDS results of **Figure 4.6**, revealing a negligible compositional impact of the substrate temperature. Quantum confinement effects suggested by Sima et al. [68] as a possible source of the shift are also unimportant at the micron-size scales of the deposited films. It is likely that the blue shift of the band gap energy is a result of the strain relief of the chalcopyrite crystal structure, indicated by the respective Bragg angle shifts in the XRD patterns of **Figure 4.7**; such band-edge shifts, induced by lattice strain, have been reported previously [69].

It is noted that the band gap energy of the studied films is determined from the inflection point of the first derivative of the absorbance, which is superimposed to the absorption coefficient data of **Figure 4.8**. Almost identical values are also obtained using the minima of the second derivative of the absorbance. Compared to the conventionally used Tauc plot method, the first-derivative method in our case provides a more reliable estimation of the CIGS band-edge, which is consistent with the photoluminescence spectra presented later in the text. This is due to the fact that the linear extrapolation process used in the former method to determine the band gap energy is affected by the presence of the r Cu_2Se secondary phase and the contribution of band-tail states of the complex quaternary semiconductor.
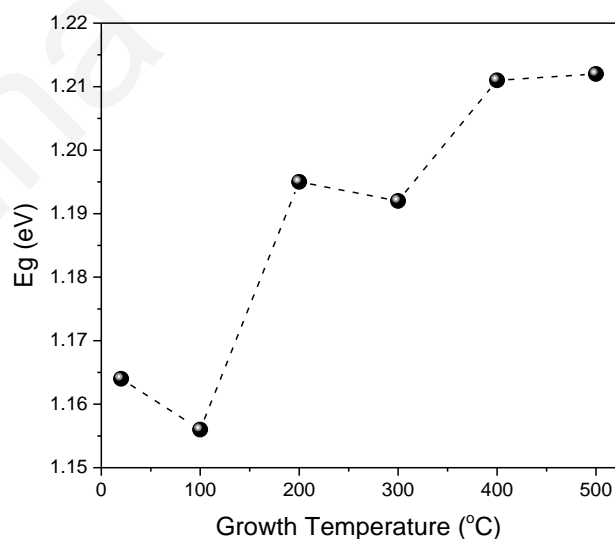
Figure 4.9 Variation of the optical band gap energy versus PLD substrate temperature [22]

Figure 4.10 presents comparative and normalized PL spectra of the CIGS films under non-resonant excitation with a 785 nm laser with a power density of $\sim$50 mWcm^{-2}. The observed broad, multi-peak lineshape is typical of the high spatial and energetic disorder of CIGS materials, as well as the presence of high energy band-edge and low energy defect-mediated recombination channels. The PL experiments indicate an improvement in the material quality and uniformity with increasing substrate temperature. This is evidenced by the: (i) monotonic increase in the integrated PL intensity, and (ii) systematic decrease of the PL linewidth and Stokes shift. The observed trends are attributed to the reduction of the band-edge potential fluctuations and the suppression of non-radiative recombination at defects related to the secondary Cu_2Se phase and the presence of Cu and Se vacancies that act as shallow acceptors and donors, respectively The effective blue-shift of the luminescence as PLD temperature increases is also consistent with an increased contribution at high energies due to emission from electronic states at the expense of the lower energy defect-related recombination; it also supports the small band gap hypsochromic shift revealed by the optical absorption experiments.
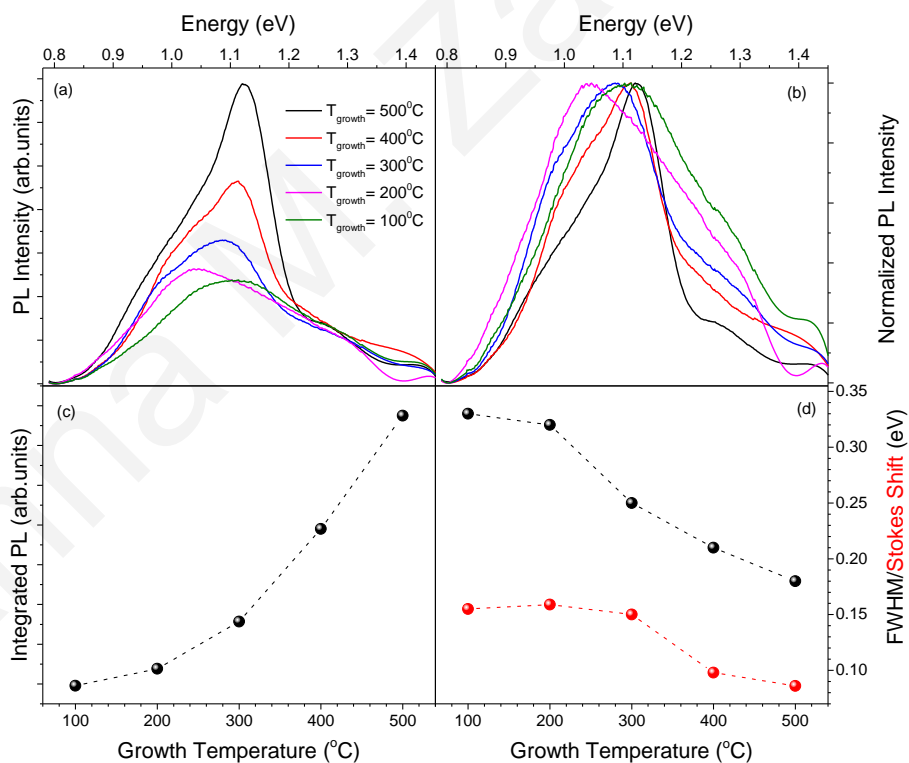
Figure 4.10 (a) Comparative PL spectra of films deposited at various temperatures in the range of 100 to 500 ^{0}C, (b) Normalized PL spectra of the same film series, (c) Integrated PL intensity versus deposition temperature, and (d) PL linewidth (FWHM) and Stokes shift as a function of substrate temperature [22]

To further resolved the emission mechanism in the studied films, we performed a PL temperature-dependent study of the three most emissive films at PLD temperatures of 300, 400 and 500^0 C, coded respectively as CIGS 300^{0}C, CIGS 400^{0}C and CIGS 500^{0}C. The PL spectra in the 10-300 K range and the respective absorption spectral profiles at 300K are displayed in **Figure 4.11**. A room temperature bandgap in the vicinity of ~1.2 eV can be estimated using the first derivative maxima that slightly blue-shifts by as much as ~20 meV as PLD deposition temperature increases due to strain relief of the chalcopyrite crystal structure [22] [69]. All films exhibit broad, multi-peak PL in the near-IR with similar spectral characteristics to those reported for material produced via evaporation [59] or PLD [56]. Inspection of the PL spectra reveals a weakly-temperature sensitive high energy emission peaked at ~1.1-1.15 eV and a strongly temperature-dependent contribution at lower energies.
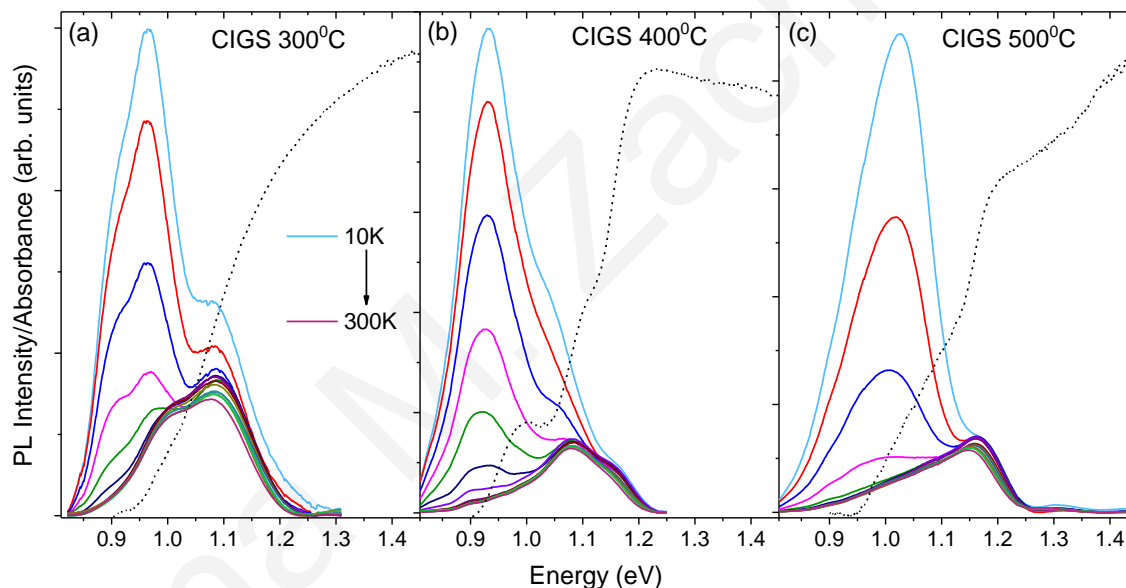
Figure 4.11 Room-temperature absorption (dotted lines) and temperature-dependent PL spectra of a) CIGS 300 ºC, (b) CIGS 400 ºC and (c) CIGS 500 ºC in the 10-300 K range. [48]

Figure 4.12 contains representative Gaussian curve fits of the PL at three temperatures per fim. CIGS 400 °C and CIGS 500 °C can be consistently fited with three Gaussian peaks (Peaks 1,2,3 in ascending energy) while an additional peak (Peak x) is required to simulate the PL spectrum of CIGS 300 °C at all temperatures.
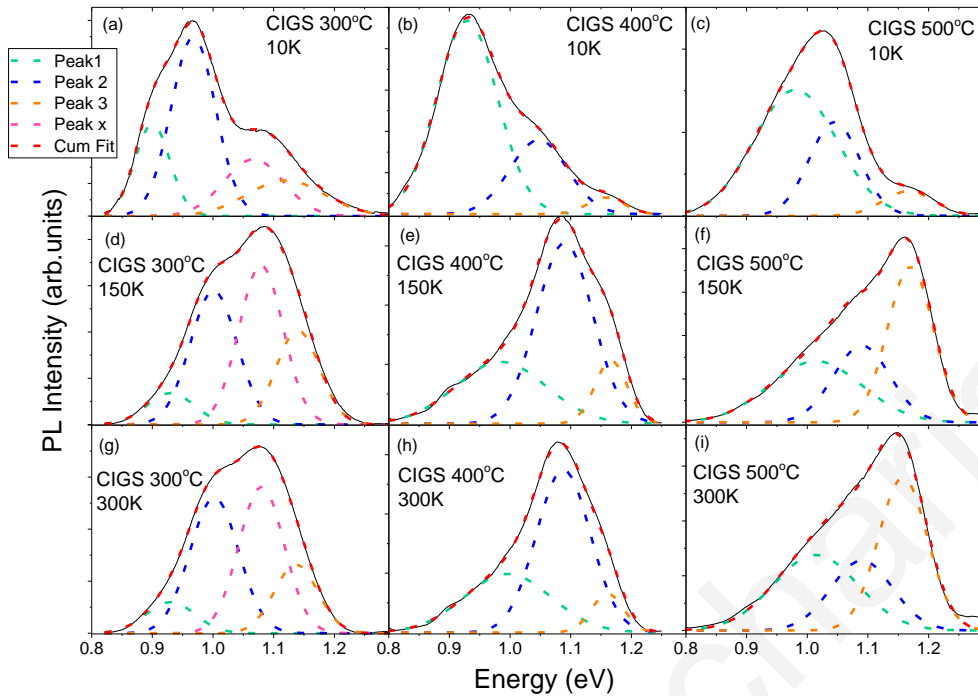
Figure 4.12 Representative examples of Gaussian lineshape analysis of the PL spectra of CIGS300 ^{o}C, CIGS400 ^{o}C and CIGS500 ^{o}C at temperatures of 10, 150 and 300K [48]

At room temperature the high energy peak 3 in the films, blue shifts with PLD temperature from ~1.14 eV at 300 ^{o}C to ~1.16 eV at 500 ^{o}C, in similar fashion and magnitude to the strain-induced shift of the energy gap observed in the optical absorption data. Furthermore its intensity shows significantly weaker dependence on temperature compared to the lower energy peaks. Based on the energetic proximity to the band-edge, the similar shift it exhibits with growth temperature and its weak temperature dependence, we assign peak 3 to the band-to-band CIGS radiative transition.

Lower energy peaks 1 and 2 are found at energies of ~150-240 meV and ~60-150 meV below the band-to-band emission with the separation from the band-edge decreasing as deposition temperature increases, as seen in **Figure 4.13.**
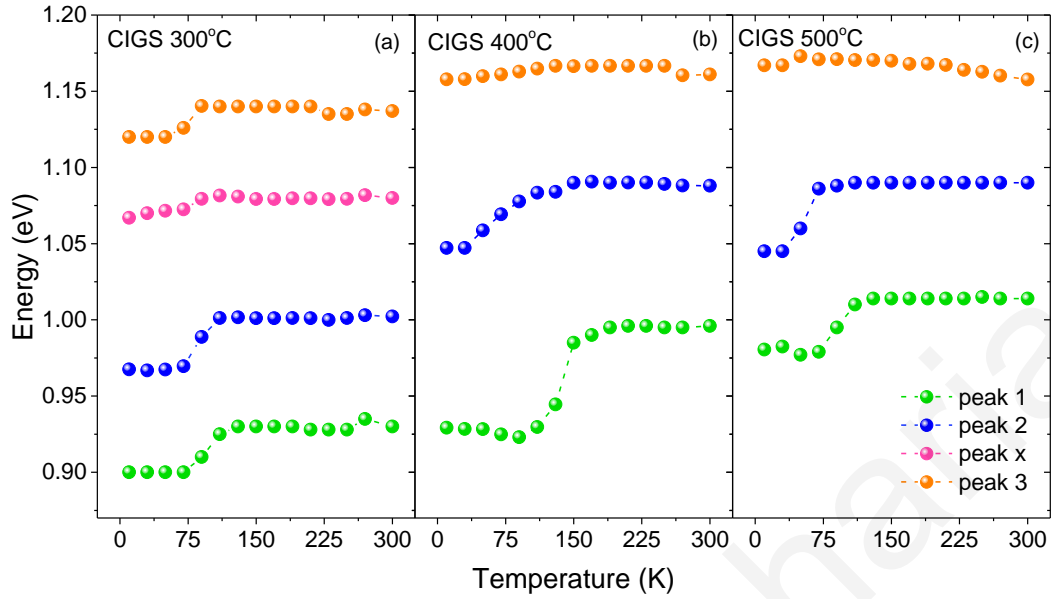
Figure 4.13 Energy positions of the extracted Gaussian PL peaks in the 10-300K range for samples: (a) CIGS 300ºC, (b) CIGS 400ºC, (c) CIGS 500ºC. [48]

This indicates that the position of the deep levels is influenced by the PLD temperature, with higher deposition temperatures inducing somewhat shallower defect levels. Peak 1, to a larger degree, as well as peak 2 exhibit strong quenching as temperature increases up to ~130 K in all films as seen in **Figure 4.14** combined with a concomitant anomalous temperature-dependent blue shift in the 80-150 K range, as observed in **Figure 4.13.** Such behaviour reported previously in co-evaporated CIGS thin films [59], indicates that carriers experience a relatively low trapping potential at the defect deep levels; as temperature increases carriers acquire sufficient energy to become detrapped and redistribute at higher energy local minima of the manifold of the defect states where they recombine non-radiatively, blue shifting and quenching the respective emission peaks. A similar type of blue-shift across the same temperature range is also visible in the band-to-band peak (peak 3) of the CIGS 300 ºC film which can be analogously being assigned to thermally-activated redistribution of carriers within energy local minima of the band potential fluctuations. Such behaviour is not observed at the band-edge emission peak of CIGS 400 ºC and 500 ºC films which confirms the hypothesis of improved compositional uniformity at higher PLD temperatures [22] resulting in an effective reduction of the band-edge potential fluctuations.

68
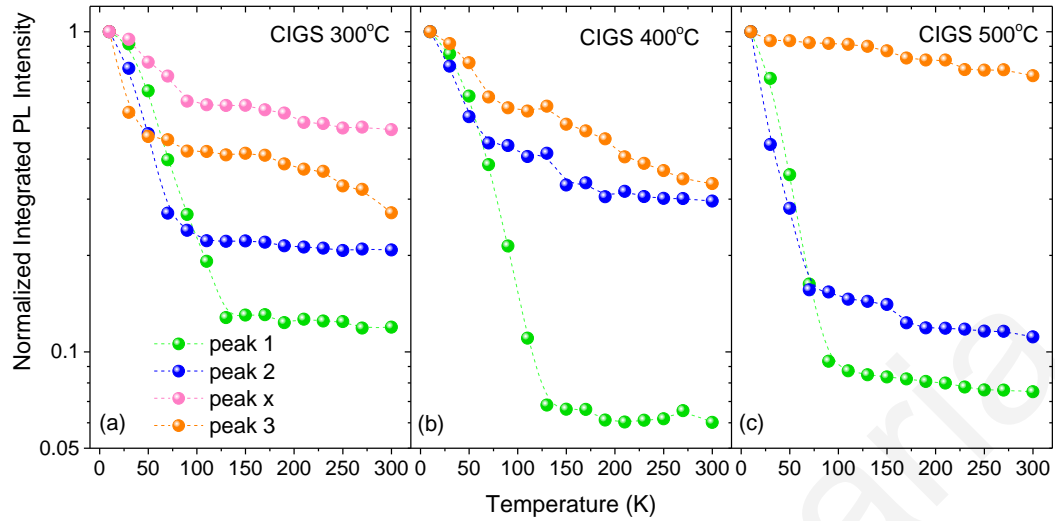
Figure 4.14 Integrated PL Intensity of the Gaussian peaks in the 10-300 K range from: (a) CIGS 300ºC, (b) CIGS 400ºC, (c) CIGS 500ºC. The PL intensity has been normalized to the intensity maximum that occurs for each film/peak at the lower temperature probed i.e. 10 K. [48]

An assignment of the deep levels participating in the emissive peaks 1 and 2 on specific CIGS point defects is challenging due to the spatial and energetic disorder that broadens deep levels to a manifold of states as evidenced by the associated broad luminescence peaks. Defects with the lower formation energy in CIGS are In_{Cu} (antisite) and V_{Cu} (vacancies) acting as individual donor and acceptors, respectively or correlated $In_{Cu}+V_{Cu}$ defect complexes [70] [71]. The latter complex induces a donor-to-acceptor emission at roughly ~200 meV below the gap [71] that based on the energetics may be associated with peak 1. According to our previous work [22], the films are slightly In-rich and Ga-deficient so In interstitials and/or Ga vacancies are also candidate deep levels involved on the emissive peaks 1 and 2. Peak x that appears as a fourth Gaussian to properly model the emission from CIGS 300 ºC most probably originates on the secondary $Cu_{2-x}Se$ phase observed via GIXRD **(Figure 4.7)** at low PLD-growth temperatures. Such assignment seems to be supported by the observation of an indirect $Cu_{2-x}Se$ electronic gap at energies coincident with peak x [72], and the absence of the peak at higher PLD deposition temperatures in which such secondary phase diminishes.

Based on the aforementioned assignments, an important figure of merit, namely the ratio of band-to-band (peak 3) to defect (peak 1 + peak 2+ peak x) integrated emission for the three films in the range of 10K to 300K is displayed in **Figure 4.15**. The higher emission quenching rate of the defect related peaks effectively increases the ratio from 10K to 100-130K while a decrease of the ratio is observed for temperatures higher than 200 K for CIGS300ºC and CIGS400ºC, as temperature-activated trapping quenches the band-to-band peak in favor of deep level emission. For CIGS500ºC an impressive dominance of the band-to-band recombination is observed for sample temperatures higher than 100 K with peak emission almost an order of magnitude higher than that of CIGS300ºC and no sign of temperature-activated quenching up to room temperature, confirming the improvement on the optoelectronic properties of the film.
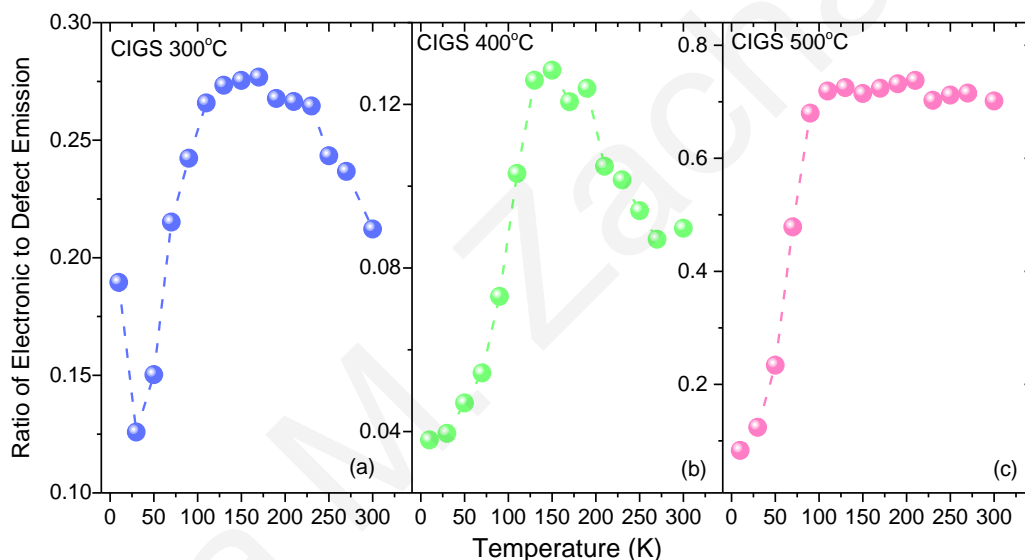
Figure 4.15 Ratio of integrated area of peak 3 (band-to-band) to the integrated emission from lower energy peaks (defect-based) at different temperatures in the range of 10-300K range for the (a) CIGS300ºC, (b) CIGS400ºC and (c) CIGS500ºC films. [48]

Additional information on the recombination mechanisms is provided by the temperature-dependent carrier dynamics probed via time-resolved PL experiments. The samples were excited by a 785nm pulsed laser (DeltaDiode-785L) with a pulse width of~80 ps. For all peaks 1,2 and 3 monitored at each temperature in the 80-300K range, the PL decays require modelling by a complex triple exponential function. Initially the PL dynamics are globally quantified for each Gaussian peak by its respective average PL lifetime, extracted by the amplitudes and lifetimes of each of the three exponential decays, as shown in Eq. **2.29**. Representative transients

at 80K, 180K and 300K monitoring the dynamics of the band-to-band peak 3 for each sample, along with the respective exponential fits and the average PL lifetimes are displayed in **Figure 4.16.**
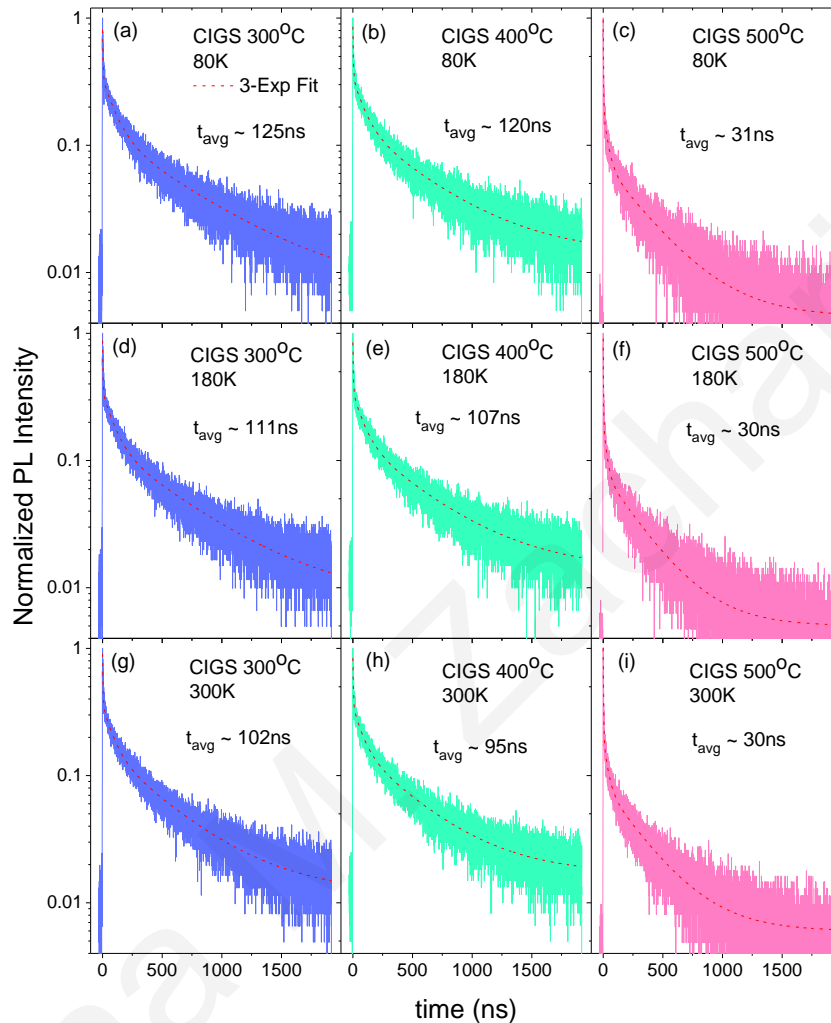
Figure 4.16 Representative PL decay curves, triple exponential fits and calculated average PL lifetimes for the band-to-band peak (peak 3) of the three CIGS film emission at (a)-(c) 80 K, (d)-(f) 180 K and (g)-(i) 300K. [48]

Figure 4.17 contains the extracted average PL lifetime versus temperature for peaks 1,2,3 of the the three films. The general trend observed is that the average PL lifetime: (i) increases as lower energy peaks are probed, (ii) reduces with sample temperature for each peak, (iii) reduces per peak as higher PLD temperatures are employed. Trends (i) and (ii) are generally consistent with the assignment of the high/low energy emission to electronic/defect-based transitions respectively. Band-edge transitions are generally expected to exhibit larger recombination rates compared to sub-gap transitions due to higher radiative rates and the presence of non-radiative

71

trapping channels that feed the lower energy peaks and effectively quench the higher energy emission lifetime. Furthermore increase of the temperature typically benefits non-radiative quenching over radiative recombination [73]. Interpretation of trend (iii) requires more elaborate thinking. For defect-related peaks 1 and 2, the shortening of the radiative rate as PLD deposition temperature increases, may be attributed to slightly shallower defect states being involved in the sub-gap emission, as hinted by the smaller separation of peaks 1,2 compared to the band-edge peak 3, seen in **Figure 4.13**. On the other hand, the quenching of the band-edge PL lifetime appears rather contradictory to the steady-state PL results that indicate a monotonic increase in the integrated PL intensity as deposition temperature is increased up to 500 °C. Furthermore, the average PL lifetime values obtained for the band-to-band peak 3 appear reasonable only for CIGS500°C, being comparable to values reported in literature for high quality CIGS thin films [73] [[74] while the dynamics of such peak appear significantly inflated for the CIGS300°C and CIGS400°C films.
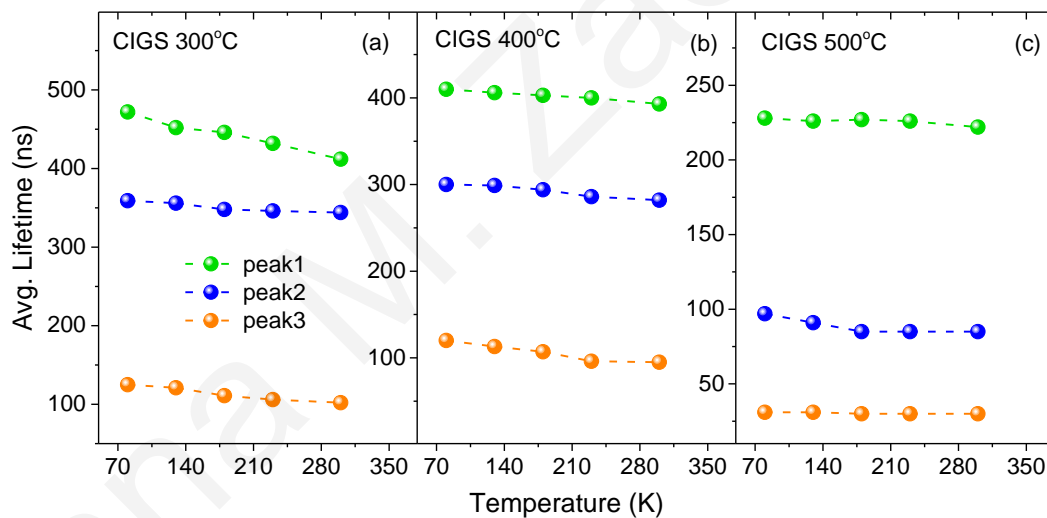
Figure 4.17 Average PL lifetime versus temperature in the 80-300K range for the three emissive contributions of: (a) CIGS300ºC, (b) CIGS400ºC and (c) CIGS500ºC. [48]

The larger band-to-band PL lifetimes obtained are in fact an artifact as the transients monitor effectively the convolution of peak 3 with the lower peak 2 or peak x; such overlap for CIGS300°C and CIGS400°C films is substantial, as vividly observed in **Figure 4.12.** To avoid such artifacts we employ a more elaborate method in which we obtain emission transients across the whole PL lineshape and we reconstruct the temporal evolution of the PL spectra. Each of the spectra on this time sequence are linefitted with the three (or four for CIGS 300 °C) Gaussian

peaks and the integrated area of each of the Gaussians is plotted versus time (TRES spectra). **Figure 4.18** contains the results of such analysis. Due to the intensive analysis associated with such method, we focus our discussion solely at room temperature.
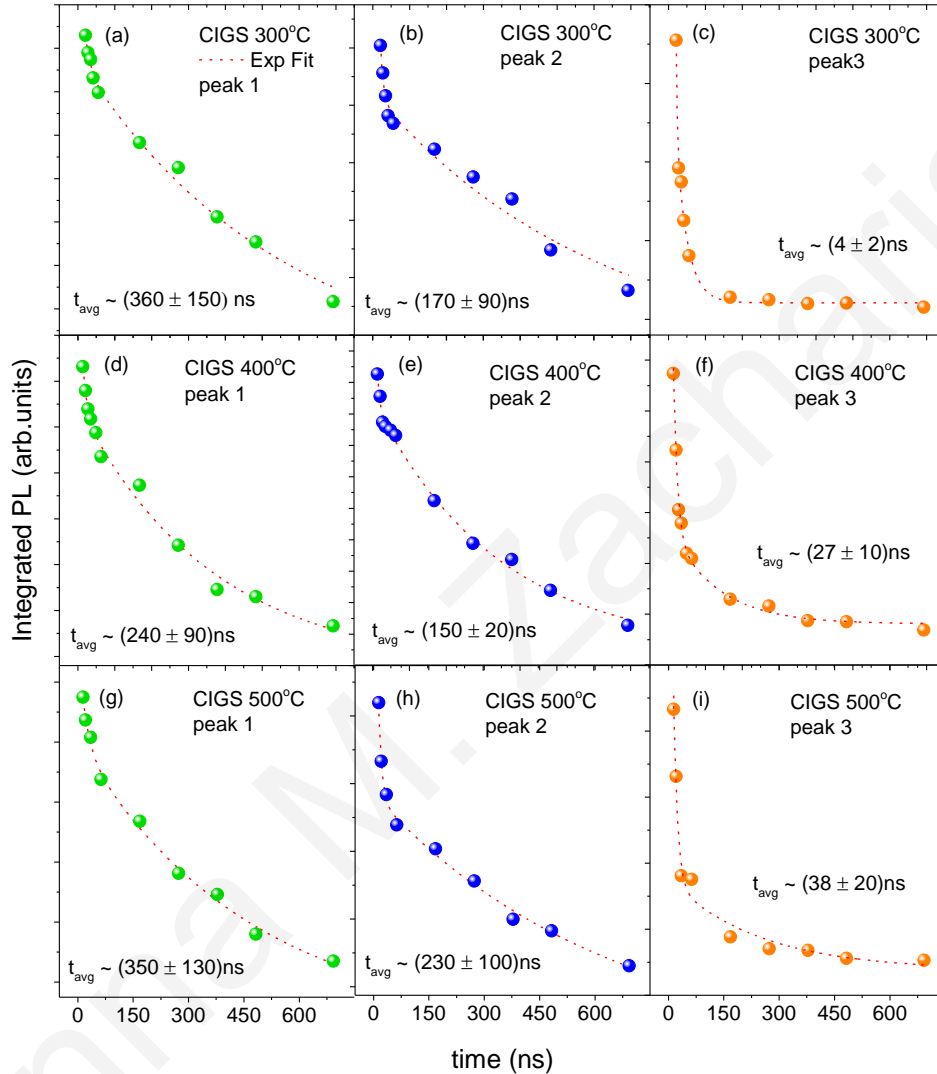
Figure 4.18 Time evolution of the integrated emission from the three Gaussian contributions of the CIGS films obtained by analysis of TRES experiments at room temperature. [48]

The obtained decays can now be adequately fitted using double-exponential decays, with a long lifetime of hundreds of ns and a significant shorter decay of the order of few to tens of ns. It is evident that the method introduces a large statistical uncertainty in the extracted decay lifetimes due to the small density of experimental data but circumvents the significant systematic error produced by the spectral overlap of the Gaussian peaks; the validity of the method has been

73

demonstrated in previous work of some of the manuscript authors on probing the dynamics of multi-component emission with overlapping peaks [75]. Focusing our discussion on the band-to-band PL dynamics i.e. peak 3, we observe that the TRES analysis yields an average PL lifetime that increases by an order of magnitude i.e. from ~4 ns to ~40 ns, as PLD temperature increases, in close agreement with the order of magnitude intensity enhancement observed in the steady-state PL results and consistent with the lifetime range values reported in the literature. The short τ_{short} and long τ_{long} lifetimes of the bi-exponential decay and the relative amplitude ratio of the latter to the former is displayed in Table 4.1.

Sample	τ_{short} (ns)	τ_{long} (ns)	$\dfrac{A_{long}}{A_{long} + A_{short}}$
CIGS 300 °C	4	30	0.01
CIGS 400 °C	10	130	0.14
CIGS 500 °C	11	180	0.16

Table 4.1 Parameters of the biexponential decay fit of the TRES PL data for the band-to-band peak (Peak3). [48]

The two lifetimes increase while the relative contribution of the long decay component enhances by more than an order of magnitude as the substrate temperature increases from 300 to 400, 500°C. Taking into account the concomitant increase of the band-edge emission, observed mainly at the higher deposition temperature, we tentatively assign τ_{short} to non-radiative recombination associated with trapping of carriers at the deep levels while τ_{long} is associated with the dynamics of the band-to-band transition. Trapping times of the order of few ns and band-to-band recombination of the order of tens to hundreds of ns such as those observed in our films, have been routinely reported in the literature for evaporated CIGS films [72], [76] so such assignment appears reasonable. It is noted that within the low excitation level range of 1 to 25 µW employed in our TCSPC experiments, no influence of the excitation fluence was observed in PL dynamics, which suggests that defect saturation effects by carriers is absent [72].

4.5 PLD-grown CdS films: Structural Properties

The influence of deposition temperature on the growth of CdS films has been investigated by depositing CdS on SLG substrates using PLD, with deposition temperatures varying from 20 to

400 °C, at optimum fluence of 1.1 J/cm^2. The thickness of the films monotonically decreases with increasing deposition temperature from 130 to 55 nm. **Figure 4.19** shows the EDS-determined compositional ratio S/Cd of the films deposited at various deposition temperatures. The S/Cd ratio was calculated by averaging the composition values obtained by scanning multiple areas for each sample. As the figure indicates, the films are sulfur deficient at room temperature and at 100 °C with increasing S/Cd ratio. At temperature of 200 °C and higher, the S/Cd ratio is almost constant, and the films are nearly stoichiometric. A plausible source for the compositional deviation described is the different sticking coefficient of S and Cd atoms during the film growth. The sticking coefficient of each element is a complex function of atomic mass, kinetic energy, incidence angle, surface energy and temperature [77]. The EDS analysis of the films presented in **Figure 4.20** leads to the conclusion that the sticking coefficient of S increases (and/or the sticking coefficient of Cd decreases) with increasing deposition temperature and the films become stoichiometric at higher temperatures. However, this is only a hypothesis as no published works exist in the literature reporting on the temperature dependence of the sticking coefficients of Cd and S atoms on SLG substrates, using PLD.
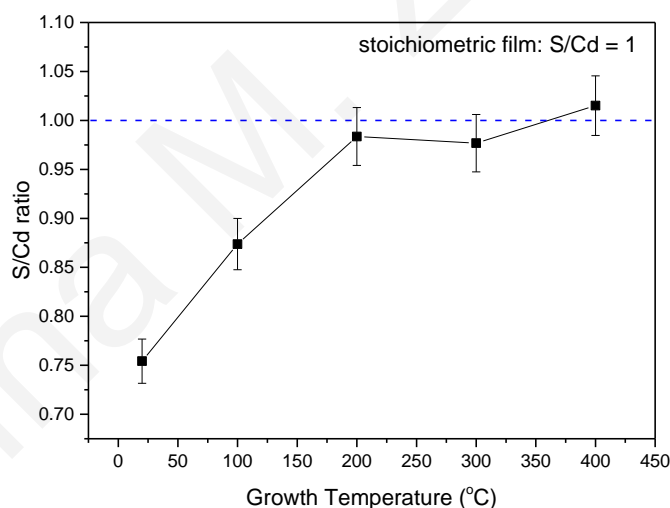
Figure 4.19 Compositional ratio of CdS thin films deposited on SLG substrates at deposition temperatures, from room temperature up to 400 °C. Dashed line indicates the ratio of a stoichiometric film, being S/Cd = 1. Films change from sulfur-poor to nearly stoichiometric films as the deposition temperature increases. [78]

Crystallite size of the films has been calculated by the Debye-Scherrer formula using the (0 0 2) diffraction peak. **Figure 4.20** illustrates the dependence of crystallite size with deposition

temperature. As the deposition temperature increases, nucleation is enhanced due to the higher kinetic of the atoms, thus larger crystallites are being formed. An abrupt increase is observed at deposition temperatures higher than 200 °C, with crystallite size of about 18 nm. Comparing the crystallite size with S/Cd ratio, stoichiometric films with S/Cd ratio close to unity are formed by larger crystallites, while sulfur-poor films exhibit small crystallite sizes of about 3–5 nm. Non-stoichiometric films (whether sulfur-poor or sulfur-rich) appear to have low crystallite sizes, while stoichiometric films with S/Cd ratio around unity grow in larger crystallites. Small crystallites have also been observed for non-stoichiometric CdS films deposited by chemical technique [79]. The observed compositional deviations of CdS films can lead to structural defects, such as S and Cd vacancies and interstitials. These point defects act as low-energy nucleation centers that limit the crystallite growth due to multiple adjacent crystallites growing next to each other [80]. Therefore, non-stoichiometric CdS films are composed of smaller crystallites compared to the stoichiometric films. Similar results have been found in other PLD-grown films [81] [82] [83] [84] [85].
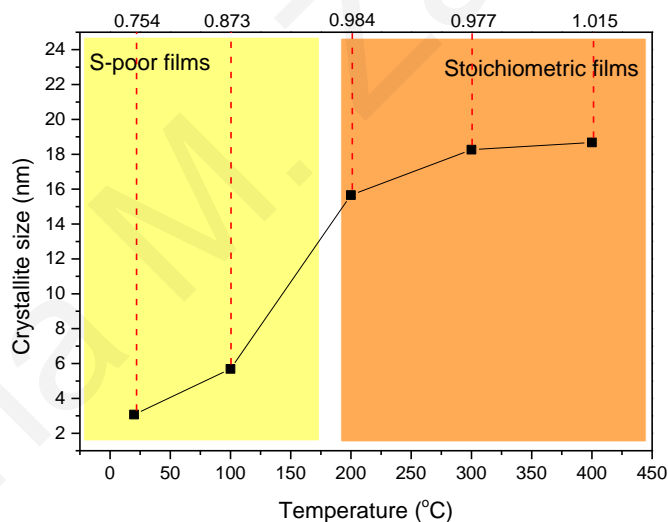
Figure 4.20 Crystallite size of CdS thin films deposited on SLG substrates as function of deposition temperature and S/Cd compositional ratio. The crystallinity of the films increases as deposition temperature increases. Sulfur-poor films have lower crystallite sizes while stoichiometric films exhibit higher crystallite sizes. [78]

4.6 Influence of Growth Temperature on the Optical Properties of PLD-grown CdS Films

The estimated energy gaps and the respective optical absorption spectra of the CdS films grown at various substrate temperatures are shown in **Figure 4.21** (a) and (b), respectively. The band gap energy is determined from the inflection point of the first derivative of the absorbance, as it has been found [22] to provide a more reliable estimation of the energy gap of pulsed laser deposited thin films. **Figure 4.21** (a) reveals a small but systematic red shift of the band gap energy from 2.55 to 2.49 eV as the substrate temperature increases from 100 to 400 °C. The estimated values are within the literature reported values of CdS [86] [87] [88]; furthermore the red shift of the gap with temperature is consistent with the respective increase of the crystallite size shown in **Figure 4.20** that results in reduction of carrier quantum confinement effects [89].
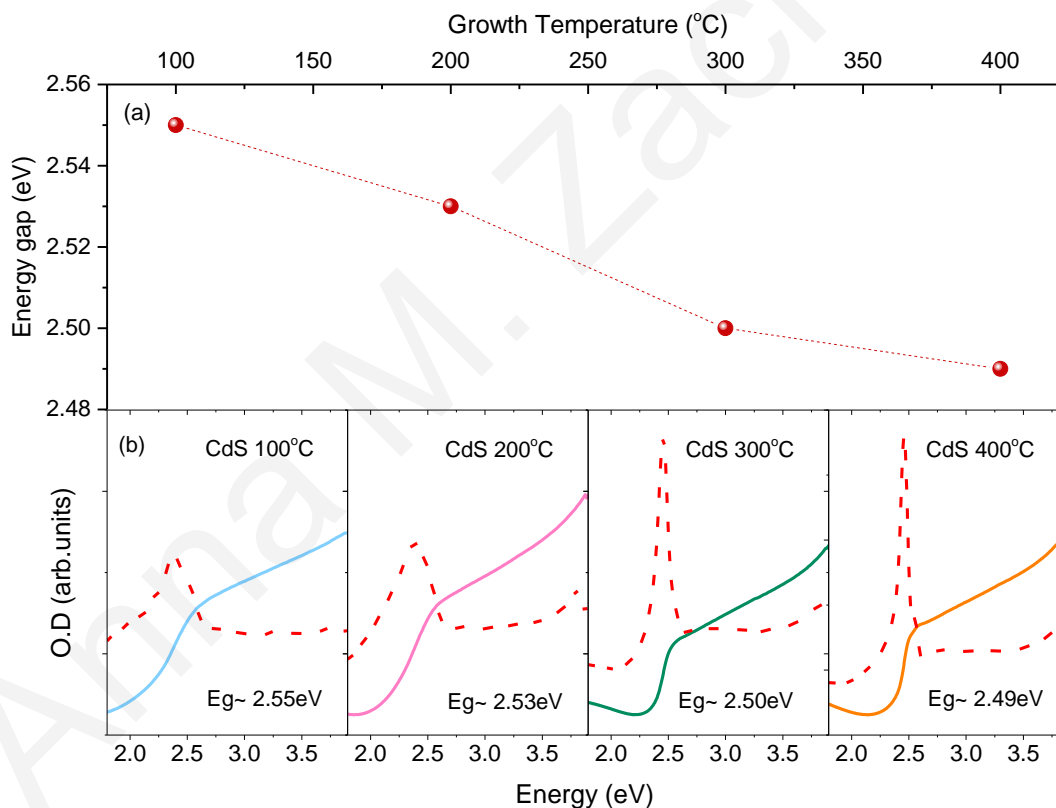
Figure 4.21 (a) Variation of the optical band gap energy versus deposition temperature (b) The steady-state absorption for the CdS films grown at various deposition temperatures. The first derivative of the absorbance and the estimated energy gap for each film is also shown. [78]

Comparative non-resonant photoluminescence (PL) spectra at 300 K of the CdS films deposited at various temperatures are displayed in **Figure 4.22** (a). Steady-state PL was excited via a 375 nm Oxxius diode laser and time-resolved PL was performed using excitation via a 375 nm NanoLED pulsed laser with a pulse width of ~150 ps. The The emission is peaked at ~2.26 to 2.28 eV and exhibits a broad PL lineshape of ~650 meV. **Figure 4.22** (b) indicates that the integrated emission increases systematically with the deposition temperature within the 100–400 °C range. The weaker emission from the Spoor film deposited at lower temperatures can be attributed to the presence of S vacancies that quench non-radiatively a fraction of the photogenerated excitons. Time-resolved PL data confirm the results of the steady-state study. The PL dynamics are quantified by the average PL lifetime τ_{ave} that is found to systematically increase from ~4 to 6 ns as the growth temperature is raised from 100 to 400 °C. The measured lifetimes appear longer than the PL dynamics measured in CdS films fabricated by CBD and DC Pulse Sputtering, witnessing the high optical quality of the produced material [90].
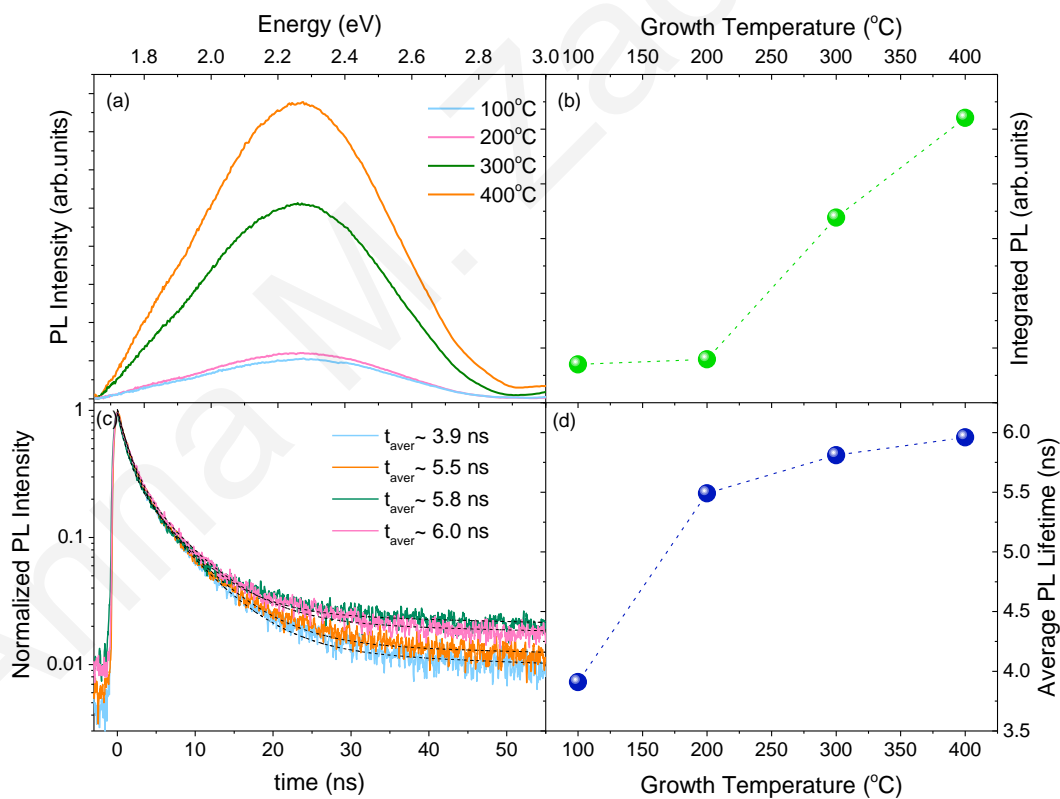
Figure 4.22 (a) Comparative PL spectra of films deposited at various temperatures in the range of 100–400 °C, (b) Integrated PL intensity versus deposition temperature, (c) PL decays measured at the band-edge PL peak from CdS films deposited at various temperatures and (d) Average PL Lifetime versus deposition temperature. [78]

4.7   Chapter Conclusions

A systematic spectroscopic investigation of PLD-deposited CIGS films as well as a preliminary study of PLD-grown CdS has been discussed. For CIGS, the work focused on studies of the influence of PLD deposition temperature on the emission properties. Variable-temperature steady-state and time-resolved experiments in combination with Gaussian lineshape analysis allow us to unravel the contribution of three main radiative channels, with the high energy one associated with electronic and two lower energy ones with defect CIGS levels. A fourth emissive channel observed at lower PLD-temperatures has been also resolved and assigned to a $Cu_{2-x}Se$ secondary crystal phase. Important figures of merit for the implementation of such films in solar cell applications such as the carrier trapping time in the range of 4 to 10 ns, the band-edge recombination time of 30 to 180 ns and the ratio of electronic to defect emission have been estimated. Such values are not far from those reported in well-studied, state-of-the-art evaporated or sputtered CIGS films, confirming the prospect of PLD as fabrication method for high quality CIGS material.

The impact of deposition temperature on the luminescent properties of CdS films grown by PLD has also been investigated and correlated to the structural data obtained from such solids. Polycrystalline and stoichiometric films with relatively large crystallites were obtained at deposition temperatures of 200–400 °C. The band gap energy of the films appears to red shift from 2.55 to 2.49 eV as the substrate temperature increases from 100 to 400 °C as a result of the increase of the crystallite sizes. Within the same PLD temperature range a consistent increase of the integrated PL and the PL lifetime is observed, witnessing the improvement of the structural film properties. Despite the very broad PL spectrum obtained which indicates large disorder, the measured PL lifetimes in the range of ~4 to 6 ns appear at the same level or longer compared to CdS films fabricated by other deposition techniques.

5   Unravelling the Origin of Photoexcitations in AgInSe QDs

Much of the focus on multinary chalcogenide colloidal quantum dots has been placed on the prototype Cu-In-S system. Ag-In-Se CQDs are significantly less developed with little work produced thus far [91] [92] [93] [94] [95] [96] [97] [98] [99]. Herein we report spectroscopic studies of robust $Ag_3In_5Se_9$ CQDs fabricated via an amide-promoted synthesis, [91] using QD size as the structural varying parameter. Temperature-dependent photoluminescence combined with Gaussian lineshape analysis reveal the consistent presence of three radiative channels in colloids and films of the $Ag_3In_5Se_9$ QDs. Based on the energetics, the temperature and QD size-dependence and the temporal characteristics provided by transient absorption and luminescence experiments, we assign the peaks to transitions from the conduction band edge to: (i) self-trapped hole states and (ii) valence band holes, (iii) holes in higher lying valence band states. The experiments provide also evidence of shallow surface states acting as sites in which fast exciton trapping and much slower de-trapping occurs, with the aforementioned rates being influenced by confinement and temperature.

5.1   Basic Properties of AgInSe Films and Nanocrystals

Silver indium selenide (AISe) is a I-III-VI semiconductor material that typically crystallizes into the chalcopyrite structure with the c/a ratio approximately equal to 2, closely related to the structure of Zinc blende. [100] $AgInSe_2$ nanocrystals have been reported in the orthorhombic lattice type (a ≠ b ≠ c, α = β = γ = 90º) [101] with a band gap energy of 1.20 eV and a melting point of 780 ∘C [102]. The nanocrystal structure and energy gap have a strong dependence on stoichiometry. For example, AgInSe CQDs with stoichiometry Ag:In = 0.8 or 0.6, crystallize in wurtzite/orthorhombic structures, while indium-rich NCs crystallize in cubic/tetragonal structures (**Figure 5.1**). Like other I-III-VI NCs, large Stokes shifts for all AISe NC compositions are reported. The band gap increases with increasing indium content because of the presence of defects and p-d orbital hybridization. [91]
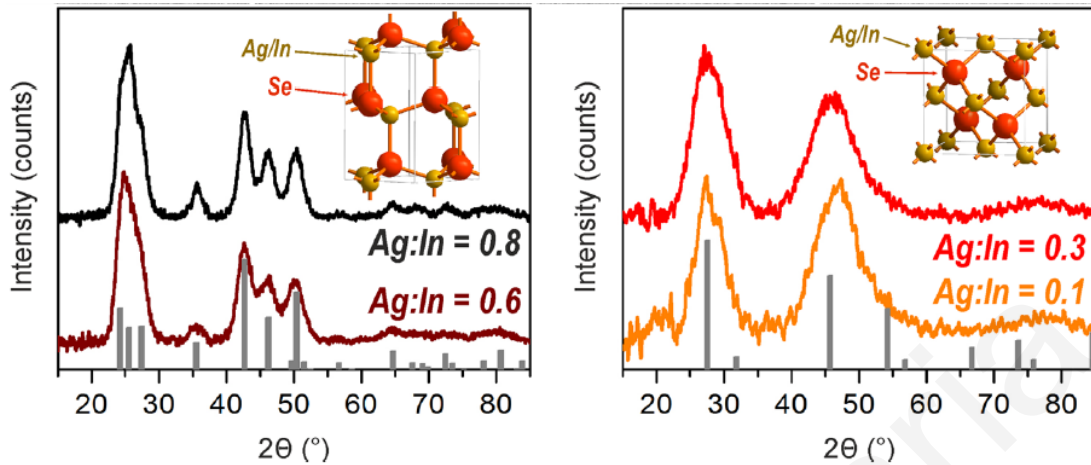
Figure 5.1 X-ray diffraction patterns for AISe nanocrystals with different compositions [91]

Regarding the electronic properties, AgInSe$_2$ (AIS) is a direct gap semiconductor that exhibits attractive optical properties (high absorption coefficient, wide band gap, etc.) that make it suitable for a variety of light emitting and light harvesting applications, including photovoltaics. [103] As the conduction band of chalcopyrites is mainly derived from group III (In) s-orbitals and the valence band position, while derived from Se p-orbitals, is strongly affected by underlying group I (Ag) d-orbitals, it is proposed that the defect responsible for the change in gap, particularly those that occur in the valence band, could be a buried In$_{Ag}$ or V$_{Ag}$ defects. Fewer Ag atoms would mean fewer d-orbitals interacting with the valence band Se p- orbitals and less repulsion, which would lower the valence band, thereby opening the gap. [104]

Despite the attractive properties of the bulk analogue, there are only a few reports that deal with the preparation of Ag-In-Se nanocrystals. Recently there has been a breakthrough with a number of effective methods being developed to synthesize AgInSe$_2$ quantum dots. Issues with these CQDs were their non-stoichiometry, the presence of an important amount of Ag$^{(0)}$ and the use of highly volatile and hazardous bis(trimethylsilyl)selenide in the synthetic method. The synthesis of stoichiometric ternary NCs can be difficult due to the necessity of balancing the reactivity of the precursors, but can be done via thermolysis and amide-promoted synthetic with less hazardous precursors. [92] A number of techniques such as flash evaporation, r.f. sputtering, thermal evaporation, solution growth, hot press, and pulse laser ablation are used for the

preparation of AgInSe$_2$ films under different experimental conditions. These techniques have advantages and disadvantages depending on the type of application intended for the films. [100]

Theoretically, Ag–In–Se CQDs are potential alternatives of the CIS CQDs to exhibit higher energy emission from orange to red. However, in the limited reports thus far, Ag–In–Se NCs appear to mainly achieve NIR emission. [105] Stoichiometry and size of I−III−VI NCs has a notable effect on band gap energy, and this must be taken into account to design materials with demanded optical characteristics. [106] Similarly to stoichiometric compositions, In-rich I−III−VI NCs exhibit relatively broad PL width (typically, 200−300 meV), large Stokes shifts, and long-lived charge carriers (on the order of hundreds of nanoseconds), as displayed in **Figure 5.2**. Composition of I−III−VI NCs has, however, a very pronounced effect on PL efficiency. [106] It should be mentioned that absorption spectra of ternary AISe is typically structureless (i.e., no well-defined exciton absorption peak), compared with those of binary NCs.
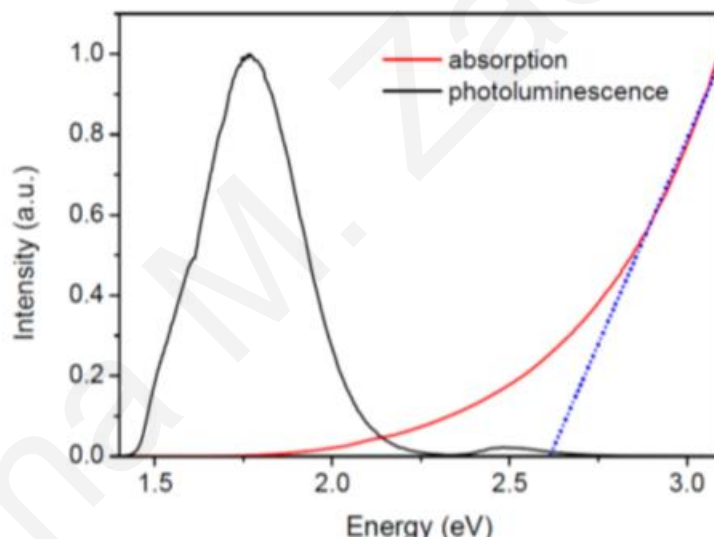
Figure 5.2 Absorption and photoluminescence spectra of AgInS$_2$ nanoparticles synthesized at 120 °C. The dotted line is obtained by extrapolating the linear part of (αhv)^2 in the absorption spectrum. [107]

5.2 Influence of size on the Optical Properties of AgInSe CQD Colloids and Films

In this work, we studied Ag$_3$In$_5$Se$_9$ CQDs fabricated via an amide-promoted synthesis, [91] using QD size as the structural varying parameter. The synthesis process was developed by the

group of Vanessa Wood that kindly supplied the material and published in [91]. CQDs with size variation in the range of ~2 to ~3.5 nm were investigated; in ascending size order, the samples are coded as S1 to S4 for the rest of the manuscript while a fifth $Ag_3In_5Se_9/ZnSe$ - Core/Shell QD sample is named as S5. The characteristics of the studied CQDs in colloidal form are included in Table 5.1.

Normalized photoluminescence (PL) from diluted CQD solutions is displayed in **Figure 5.3 (a)**. The solutions were excited by a cw-diode laser at 375 nm (~ 3.31 eV) with an excitation density of ~25 mW/cm^2. The CQDs exhibit broad emission, typical of ternary I-III-VI NCs, with the PL peak progressively red shifting from ~1.74 eV (~713 nm) for S1 to 1.59 eV (~780 nm) for S4 as quantum confinement reduces, as shown in **Figure 5.3 (b).** The PL quantum yield (QY) of the samples is displayed in **Figure 5.3 (c)**; it exhibits a non-monotonic variation with size in the 5% to 21% range, with an initial sharp increase as surface recombination becomes less efficient, followed by a more gradual drop as confinement energy reduces. The PL lineshape can be reconstructed by three Gaussian peak, as representatively displayed in **Figure 5.3 (d)**.
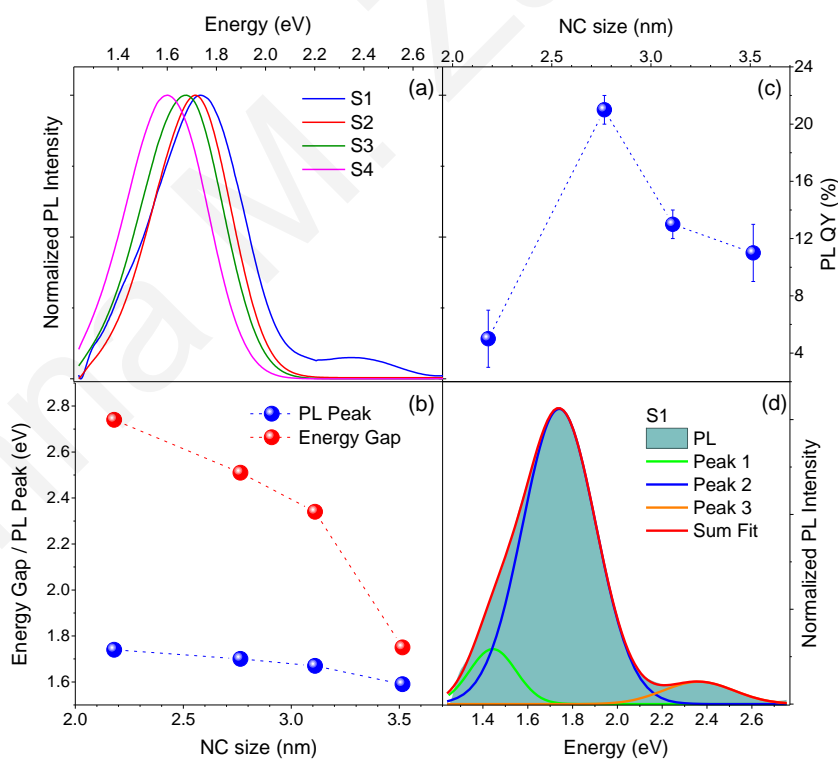
Figure 5.3 (a) Normalized PL spectra of the CQD solutions. (b) PL QY of the CQD solutions. (c) Estimated gap and PL peak versus QD size. (d) Example of Gaussian lineshape fitting of the room temperature PL of S1.

Sample	Size (nm)	Energy Gap (eV)	PL Peak (eV)	FWHM (eV)	QY(%)
S1	2.18 ± 0.33	2.23	1.76	0.44	5
S2	2.77 ± 0.37	2.14	1.72	0.36	21
S3	3.11 ± 0.37	2.02	1.68	0.36	13
S4	3.52 ± 0.41	1.75	1.61	0.35	11

Table 5.1 Structural and emission characteristics of the studied QDs in colloidal form

The studied $Ag_3In_5Se_9$ QDs crystallize in the wurtzite structure, exhibiting a polygonal QD shape, as evident in the high-resolution TEM (HRTEM) image of **Figure 5.4 (a**), and the QD model illustration in **Figure 5.4 (b),** respectively. Most of the work focused on spectroscopy of CQDs in the form of thin films. To produce the films, quartz substrates were thoroughly cleaned in nitric acid (HNO_3), washed by deionized water and dried with compressed air. Subsequently they were submerged in (1:10 v/v) triethoxy(octyl)silane solution in toluene to become hydrophobic. Prior to deposition the substrates were washed with toluene and dried. 25μL of solution was spin coated at 1000 rpm for a minute followed by a drying step at 4000rpm for 20s. A portion of samples were drop casted on the same substrates and vacuum dried in a desiccator to ensure rapid evaporation of the solvent and uniformity of the films.

The CQD films exhibit broad emission, typical of ternary I-III-VI NCs, with the PL peak progressively red shifting from ~1.79 eV (~693 nm) for S1 to 1.61 eV (~770 nm) for S4 as quantum confinement reduces, as shown in **Figure 5.4 (c).** A parametric line-shape analysis of the emission spectra of QD films performed across the aforementioned QD size range reveals that the PL lineshape can be consistently reconstructed with a three Gaussian peak model, in agreement with the CQD data, with the addition of a fourth weak contribution, present only in the largest QD S4 film; The core-shell CQD film is also nicely fitted via 3 Gaussians. **Figure 5.4 (d)** shows the lineshape fitting analysis for S2 as an example. The structural and emission characteristics of CQD films are summarized in Table 5.2.
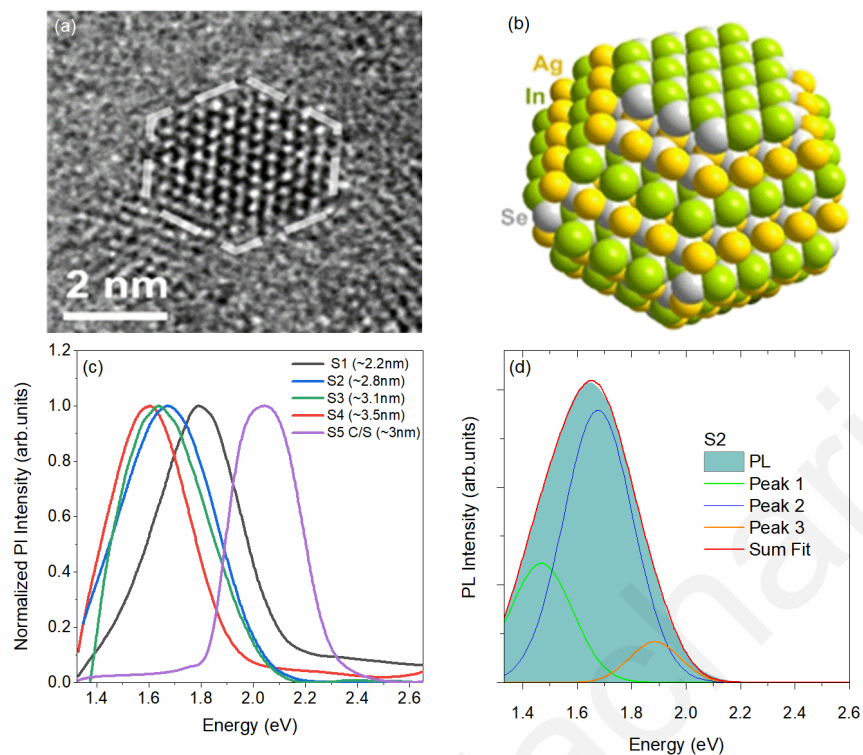
Figure 5.4 (a) HRTEM image of a single Ag₃In₅Se₉ nanocrystal. (b) Three-dimensional model of the Ag₃In₅Se₉ QDs under study. (c) Normalized PL spectra of the S1(2.2 nm), S2(2.8 nm), S3 (3.1 nm), S4(3.5 nm) and S5(3 nm -core/shell) QD films. (d) Example of Gaussian lineshape fitting of the room temperature PL of the S2 film.

Sample	Size (nm)	PL Peak (eV)	FWHM (eV)
S1	2.18 ± 0.33	1.80	0.41
S2	2.77 ± 0.37	1.68	0.43
S3	3.11 ± 0.37	1.64	0.42
S4	3.52 ± 0.41	1.60	0.37
S5	~3 nm (core)	2.04	0.31

Table 5.2 Structural and emission characteristics of the studied CQD films.

The consistency of the three peak fitting indicates that three main, distinct radiative recombination channels exist in the studied CQD. Based on substantial evidence by

temperature-dependent photoluminescence and transient absorption and luminescence experiments presented later in, the three channels are attributed to transitions from the conduction band to: (i) sub-gap states associated with self-trapped holes (peak 1), (ii) ground state valence band states (peak 2), (iii) higher valence band states (peak 3).

Variable temperature PL data recorded from the S1 (~2.2 nm), S2 (~2.8 nm), S4 (~3.5 nm) and the S5 - Core/Shell CQD films in the 30 to 300 K range, are displayed in **Figure 5.5 (a)** to **(d)**. **Figure 5.5 (e)** to **(j)** summarizes the temperature dependence of the position and relative weight of the three main Gaussian PL components from the four films, while representative fit examples at various temperatures are provided in **Figure 5.6.**
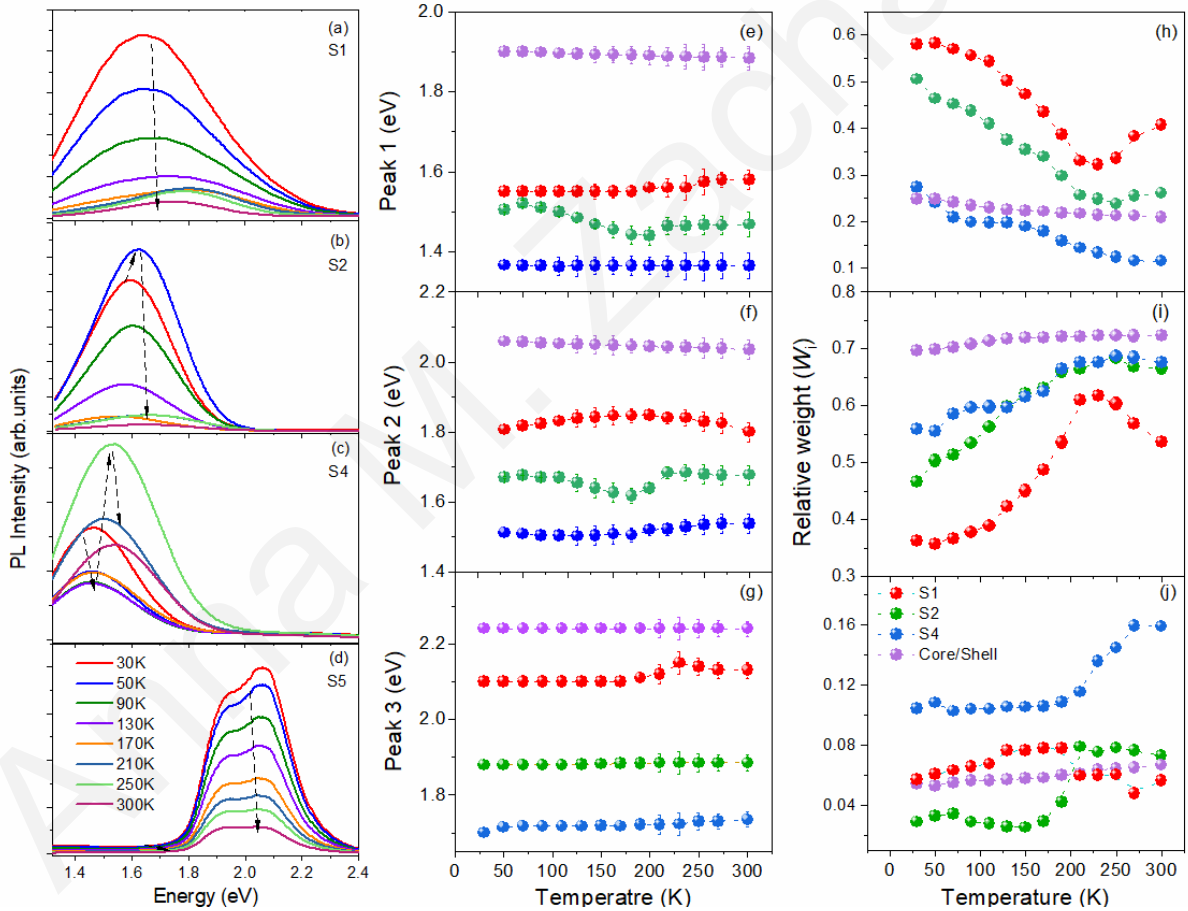
Figure 5.5 Temperature-dependent PL spectra of (a) S1, (b) S2, (c) S4, (d) S5 in the 30 K to 300 K range. Results of a Gaussian lineshape analysis performed at the variable temperature PL data of QD films S1, S2, S4 and S5. (e) Peak 1, (f) Peak 2 and (g) Peak 3 position as a function of samples temperature. Relative weight (Wi) for (h) peak 1, (i) peak 2 and (j) peak 3 versus temperature for the four QD films.
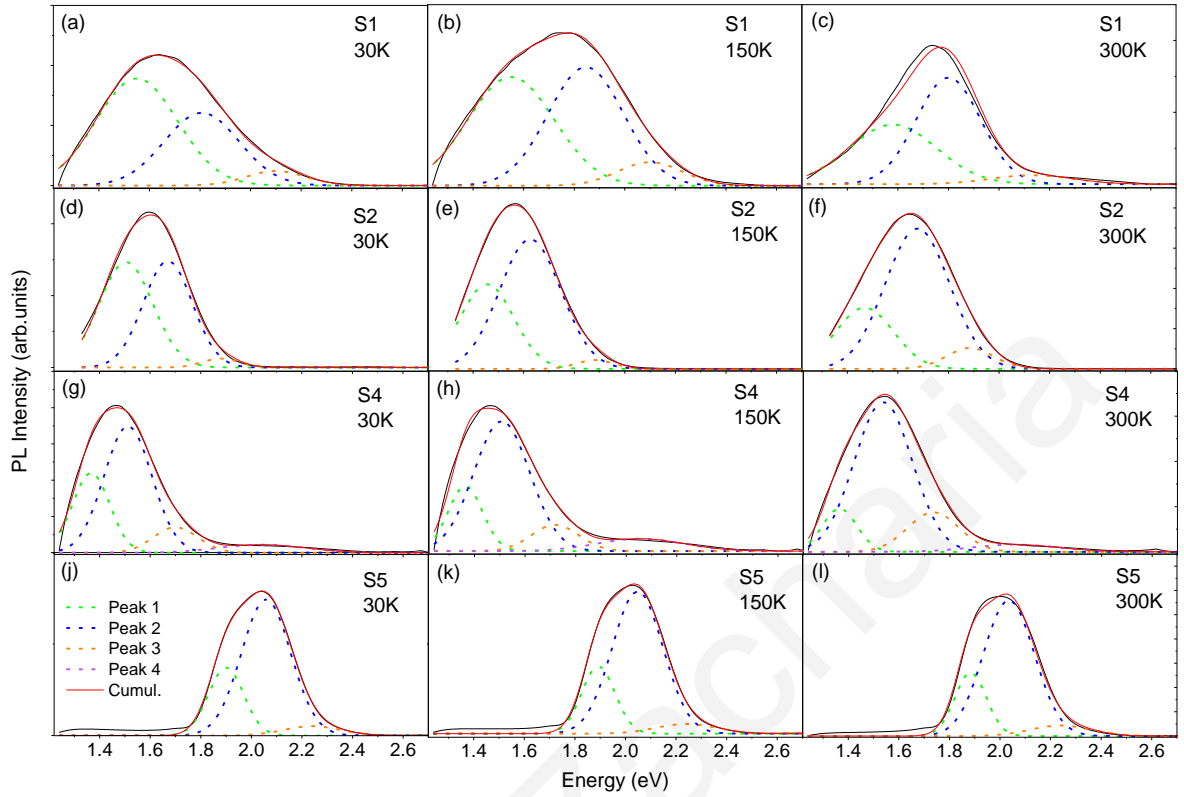
Figure 5.6 Representative examples of Gaussian lineshape analysis of the PL spectra of S1, S2, S4 and S5 at temperatures of 30, 150 and 300K

All three Gaussian peaks are found to red-shift as QD size increases, however the confinement appears to affect more the two higher emissive channels compared to peak 1 in consistency with their assignment to transitions between QD electronic levels. Furthermore, a temperature-dependent competition of the relative weight of the three peaks is visible. In the smaller QD sizes, peak 1 is the dominant channel at low temperatures; as temperature increases, peak 2 and to a lesser degree the weak peak 3 prevail at the expense of peak 1.

The integrated emission intensity *I(T)* of the two electronic-based transitions of peak 2 and 3 can be fitted as a function of temperature, via Eq. **3.1**, as displayed in **Figure 5.7.** The model produces good fits of the luminescent data for all four samples, yielding E_{LO} in the range of ~18-22 meV in agreement with phonon values obtained in studies of polycrystalline AgInSe [43], while a fixed average acoustic phonon energy of 5 meV is extracted.
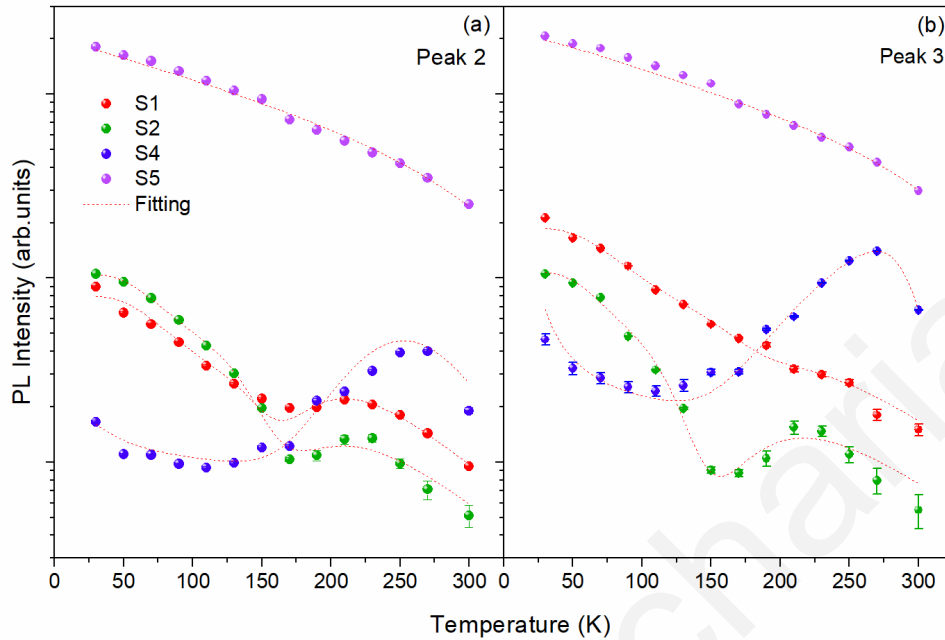
Figure 5.7 Arrhenius plots of the PL peak 2 (a) peak 3 (b) for S1 (red), S2 (green), S4 (blue) and S5 (purple) films. The red dashed line displays the fitted curve by the modified Arrhenius model.

As expected, the number of optical phonons that are required to activate quenching of excitons via phonon-assisted thermal escape from the QD confinement potential decreases with QD size, as shown in Table 5.3. Using an average LO phonon energy of 20 meV, the confinement potential of S1, S2 and S4 are estimated to be around 240, 200 and 150 meV for the two peaks. The exciton detrapping barrier ΔE also increases with confinement. The values extracted for S1, S2 and S4 are 46, 41 and 36 meV for peak 2 and 45, 44 and 37 meV for peak 3 respectively. Thermally-activated QD exciton detrapping process is evident in **Figure 5.7** for the S1, S2 and S4 film above 200K, resulting in an anomalous growth of the peak 2 and peak 3 intensity. It is reasonable to assume that traps are introduced by QD surface states with trapping potential that deepens as size is decreased [45] as surface to volume ratio becomes significantly larger as the size decreases. Such an assumption is further supported by the findings of the transient absorption experiments discussed in the next manuscript section, as well as the behavior of the better passivated core-shell sample. In this case monotonic quenching of PL intensity was recorded suggesting the absence of thermally activated de-trapping processes from surface states.

Sample	ΔE (meV)	E_{AC} (meV)	E_{LO} (meV)	m
Peak 2				
S1	46	5	22	12
S2	41	5	21	10
S4	36	5	20	7
S5	0	5	19	1
Peak 3				
S1	45	5	22	12
S2	44	5	21	10
S4	37	5	20	8
S5	0	5	19	1

Table 5.3 Results of the Arrhenius plot fit of conduction to valence band transitions (peak 2 and peak 3) for S1, S2, S4 and S5 films.

Transient PL and absorption experiments were implemented to probe the recombination dynamics in the $Ag_3In_5Se_9$ QD solids and provide further evidence on the assigned origin of the Gaussian PL peaks. Time-resolved photoluminescence (TR-PL) was performed using excitation via a 375 nm laser diode with pulse width of ~150 ps. The PL decay of each of the peaks 1,2 and 3 were monitored at temperatures between 80 and 300 K and fitted by a double exponential model, as demonstrated in **Figure 5.8** for the S1 and S5 film.
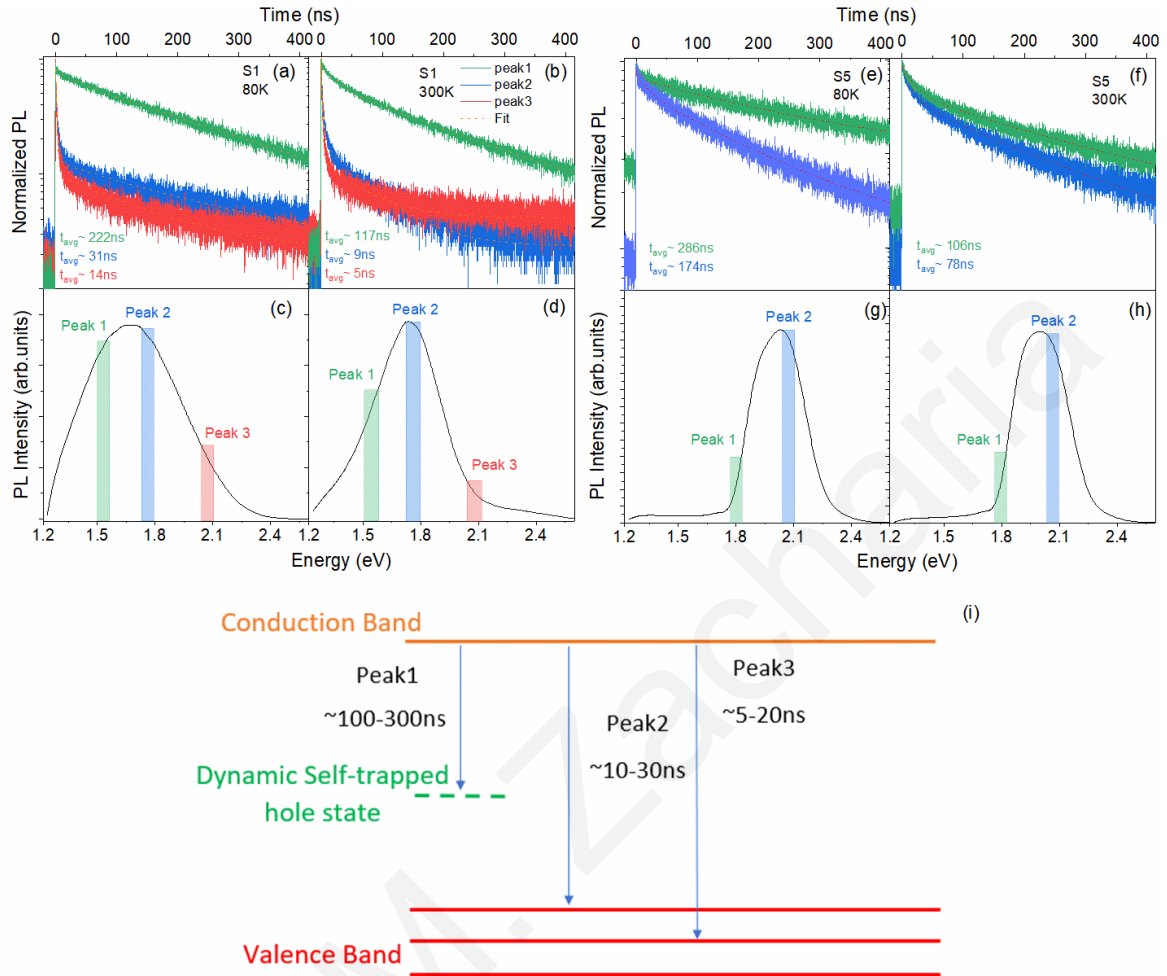
Figure 5.8 Representative PL decay curves, double exponential fits and calculated average PL lifetimes for the three main Gaussian PL contributions of the S1 film at (a) 80K and (b) 300K and S5 film at (e) 80K and (f) 300K. PL spectra of the S1 at (c) 80K and (d) 300K and S5 at 80K (g) and (h) 300K. The colored rectangles denote the energy at which each decay was recorded, while their width represents the bandwidth of the measurement. (i) Model of the radiative transitions and the respective dynamics in the studied QD films.

Similar decay dynamics and trends were obtained from all studied films with the average PL lifetime decreasing with probing energy and reducing with temperature. The PL lifetime of peaks 2 and 3 is estimated in the range of tens of ns while the dynamics of the lower energy peak 1 are significantly longer by approximately one order of magnitude. The lifetime values of the electronic transitions peak 2 and peak 3 appear comparable to respected dynamics reported for free exciton transitions in $AgInS_2$ nanoparticles [107]. Looking into the contribution of the

two components of the bi-exponential model fit, we find that for peak 2 and 3 the kinetics for all QD sizes are dominated by a fast channel of 1-2 ns with a significantly weaker longer decay component that varies in the 50 to 200 ns range. The fast dynamics of the former decay indicate that it is most probably associated with trapping of the free exciton, respectively while the weaker longer decay can be assigned to the radiative lifetime of the two transitions. On the other hand the dynamics of the low energy peak do not contain the fast trapping channel, being dominated by a significantly slower component with time constant of 30-50 ns (Table 5.4). For Core/Shell - S5, the PL lifetime of peaks 1 and peak 2 is estimated in the range of hundreds of ns. The PL kinetics are dominated by a channel of 10-50 ns with a longer and weaker decay component that varies in the 100 to 400 ns range (Table 5.5). The dynamics of the energy peak of S5 do not contain the fast trapping channel. The recombination channels along with their respective timescales are schematically illustrated in **Figure 5.8 (i)**.

	τ_s (ns)	RW (%)	τ_l (ns)	RW(%)	τ_s (ns)	RW(%)	τ_l (ns)	RW(%)	τ_s (ns)	RW (%)	τ_l (ns)	RW(%)
T (K)	Peak1	Peak1	Peak1	Peak1	Peak2	Peak2	Peak2	Peak2	Peak3	Peak3	Peak3	Peak3
80	29	13	250	87	2.2	87	221	13	1.7	91	144	9
130	31	17	221	83	2.4	85	174	15	1.8	90	129	10
170	33	23	205	77	2.5	85	134	15	1.8	88	92	12
210	30	21	209	79	2.6	84	124	16	1.8	88	74	12
250	24	24	200	76	2.6	84	97	16	1.6	89	51	11
300	24	39	176	61	2.1	88	64	12	1.4	93	61	7

Table 5.4 Lifetime components short (τ_s) and long (τ_l) along with their respective relative weight (RW) for S1 in the 80-300K range.

	τ_s (ns)	RW (%)	τ_l (ns)	RW(%)	τ_s (ns)	RW(%)	τ_l (ns)	RW(%)
T (K)	Peak1	Peak1	Peak1	Peak1	Peak2	Peak2	Peak2	Peak2
80	12	13	327	87	20	19	211	81
130	18	15	295	85	27	26	201	74
170	40	19	295	81	23	30	200	70
210	27	26	257	74	25	34	192	66
250	22	35	230	65	23	43	183	57
300	18	50	193	50	16	54	150	46

Table 5.5 Lifetime components short (τ_s) and long (τ_l) along with their respective relative weight (RW) for S5 in the 80-300K range.

To provide insight into the photogenerated species and their relaxation mechanisms, we employed ultrafast transient absorption measurements. The differential transmission spectra of the four films at various pump-probe delay times are presented in **Figure 5.9 (a) to (c)**. The spectra in S2, S3 and S4 are dominated by positive bleaching bands that become broader and more intense as QD size increases. In the case of the smaller QD size probed i.e. the S1 film, photo-induced absorption (PIA) prevails evolving slowly into a small positive signal at high energies within the vicinity of the ground state QD exciton. The pump probe dynamics at energies coincident with the respected peaks 1, 2 and 3 of the PL of the samples are displayed in **Figure 5.9 (d)** to **(f)**. All decays require modeling by the following triple exponential model that includes also a background term A_0 suitable for the description of processes with dynamics considerable larger than the 500 ps range of the pump probe setup:

$$\left|\frac{\Delta T}{T}\right| = A_0 + A_1 e^{-\frac{t}{\tau_1}} + A_2 e^{-\frac{t}{\tau_2}} + A_3 e^{-\frac{t}{\tau_3}} \qquad 5.1$$

The dynamics are globally quantified using the notion of the average decay time defined by equation **2.29**. The fitting results are presented in Table 5.6.
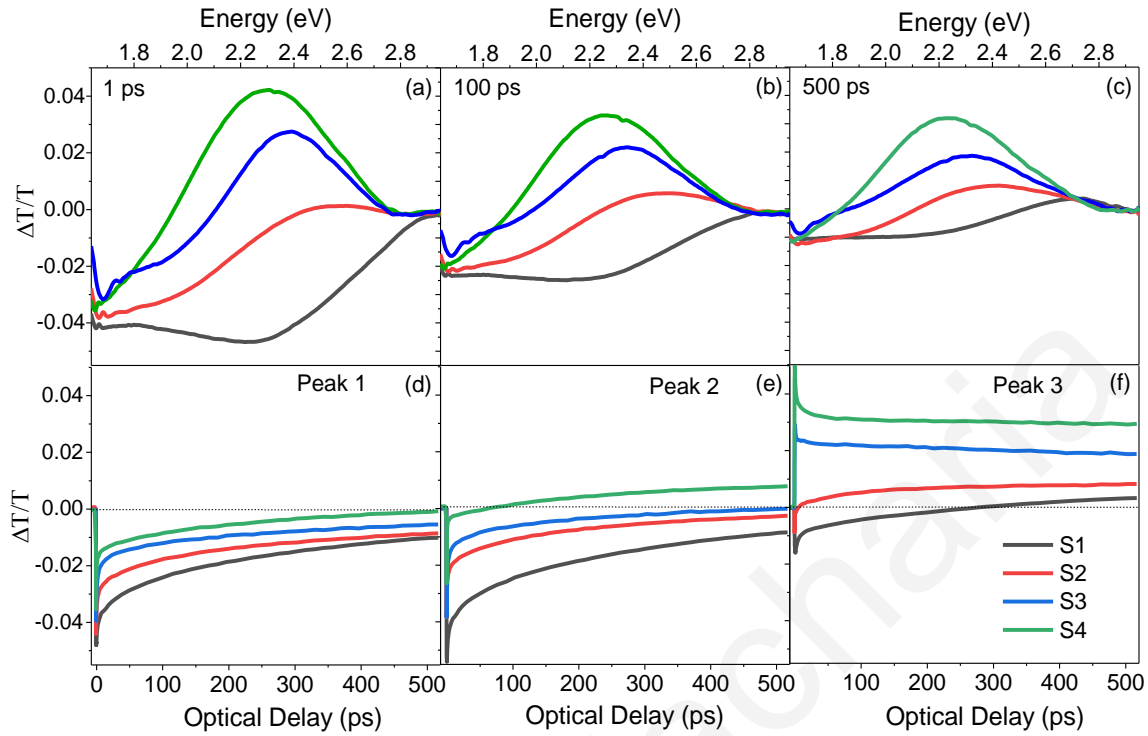
Figure 5.9 Differential transmission spectra from the four studied films at different pump probe times of 1 ps (a) 100 ps (b) and 500 ps (c). Transient decays for the four films monitoring the dynamics of peak 1 (d), peak 2 (e) and peak 3 (f).

The band edge transition associated with the emissive peak 2 is found to be slowly build-up with a time constant that becomes progressively slower i.e. from 80 to 265 ps as QD size decreases from ~3.5 το ~2 nm, as seen by the fitting summary presented in Table 5.6. As a result, bleaching signals i.e. positive differential transmission signals appear at progressively longer times as QD size increases with the smaller QD sizes of S1 and S2 showing a state-filling trend at pump-probe delays longer than the 0.5 ns limit studied. A similar trend is observed in the S1 and S2 for the transition involving higher valence band states associated with the emissive peak 3. The slow build-up of the TA signal is attributed to a slow exciton de-trapping process from shallow surface traps, resulting in a gradual population of the QD core electronic states. Based on the temperature-dependent PL experiments presented earlier, the localization energy of such surface traps increases as QD size decreases, which explains the faster de-trapping rates as QD size increases and the traps become shallower; the faster carrier de-trapping then results in a concomitant faster state-filling of the electronic states in the larger QDs probed. In the vicinity

of the lower energy peak, TA is found to be dominated by photoinduced absorption transitions, with slow recovery times in the range of 200 – 300 ps range.

Sample	Avg. Decay Time Peak 1 (ps)	Avg. Decay Time Peak 2 (ps)	Avg. Decay Time Peak 3 (ps)
S1	310 ± 21	265 ± 19	145 ± 14
S2	290 ± 19	220 ± 17	25 ± 4
S3	255 ± 16	165 ± 10	20 ± 5
S4	215 ± 18	80 ± 6	200 ± 10

Table 5.6 Differential transmission decay fitting results for the four QD films.

Summarizing on the presented results, the QD size-dependence of peak 1 implies the involvement of the quantized electronic states of QDs. The large separation from the QD band-edge but the rather size-independent PL bandwidths indicate that a localized sub-gap state is involved in the channel justifying its assignment to a free to bound transition [31] [108]. Based on the extensive studies of the Cu-In-S NC system, the localized carrier is most probably the hole [31]. The strong emission quenching with temperature and the obtained long PL lifetimes [109] [31] further support the assignment of the channel to the free-to-bound pair recombination model used to rationalize the emissive transitions in Cu-In-S NCs. On the other hand, the stronger influence of confinement, the faster emission dynamics and the presence of strong state filling effects combined with the consistent results on the thermally-assisted exciton quenching via QD surface states imply that the higher transitions involve only electronic states of the Ag-In-Se CQD.

Recent work on band structure electronic calculations of Ag-In-Se QDs was carried out by the collaborative group of V. Wood at ETH Zurich to assess the validity of the proposed emission model in the studied Ag-In-Se CQDs. Tight binding parameters were fitted to ab initio band structure calculations of Ag-In-Se compounds with and without vacancies. s- and p-orbitals were used for In and Se, while d-orbitals were included to describe Ag and vacancies.

94

Calculations were carried out using OMEN software [110]. The **Figure 5.10 (a)** shows the DOS function. The two main optical transitions, based on the calculated optical coupling strength are presented with arrows, denoting the involved energy levels of the CQDs as well. They correspond to transitions between: (i) The 1st VB and 2nd CB state (higher energy transition), (ii) The 1st VB and the 1st CB state i.e. the effective CQD bandgap. The respected peaks in the experimentally measured spectrum of the TA bleaching band of **Figure 5.10 (d)** were estimated from the first - derivatives of the spectra. The good agreement of theory and experiment is confirmed in the summary plot of **Figure 5.10 (c)** that contains the CQD size-dependent comparison of the energy position of the two lowest transitions. The lineshape of simulated and experimentally obtained absorption spectra are not equally well matched as in such case disorder and solid-state interactions present in the CQD film studied are not adequately addressed by the modeling; further optimization work on the simulations is in progress.
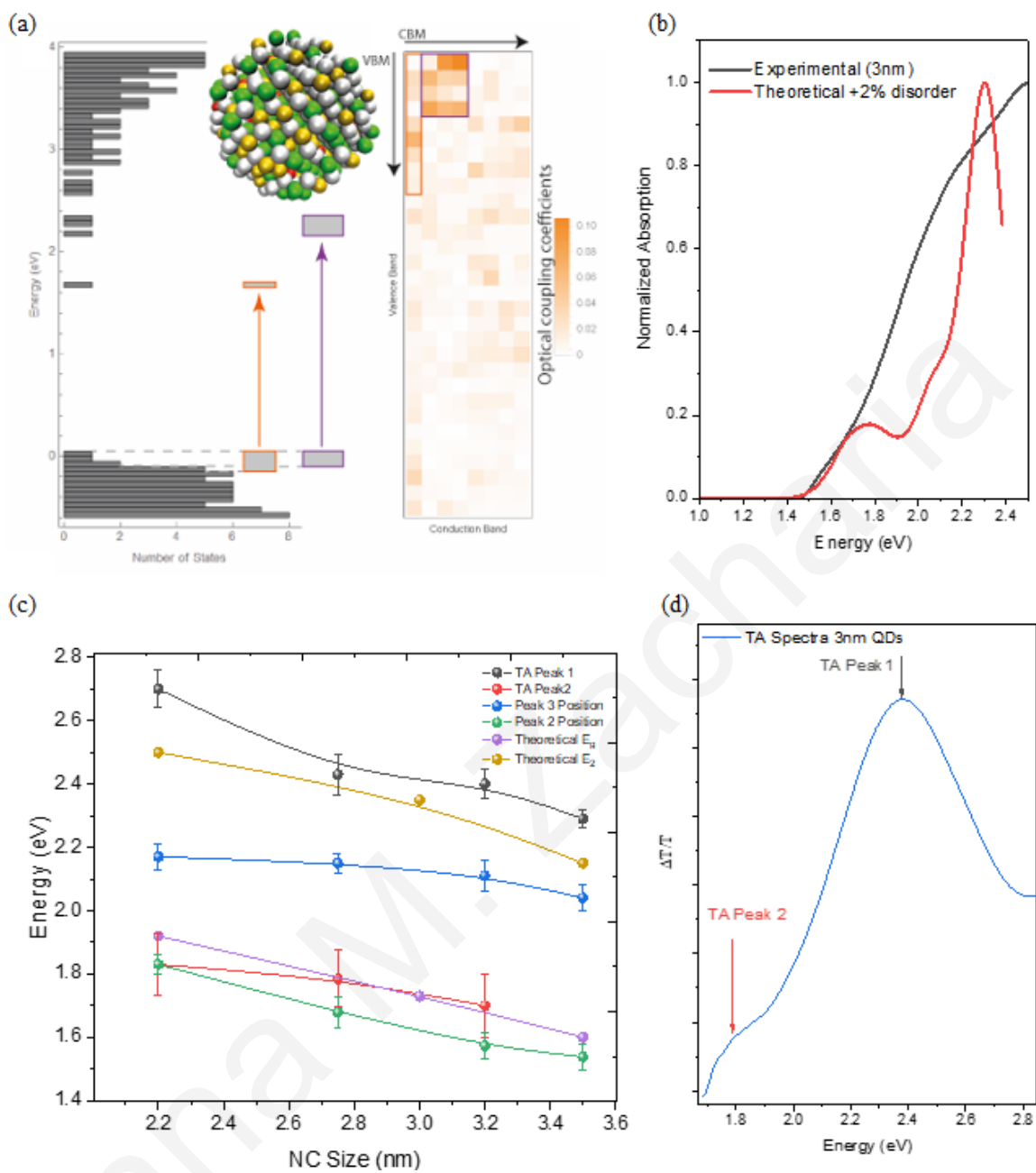
Figure 5.10 (a) Number of states from ab-initio calculations, (b) Normalized absorption spectra of 3nm sample from experimental (black line) and theoretical calculations (red line), (c) Energy position of two main energy absorption transitions and PL Peak 2 and peak 3 versus NC Size and the two transitions which are presented with arrows in figure 5.10 (a), (d) Differential transmission spectra of 3nm QDs.

5.3 Chapter Conclusions

A systematic photophysical investigation of colloids and films of non-stochiometric $Ag_3In_5Se_9$ CQDs is presented, using the QD size in the range of ~2 το 3.5 nm, as the adjustable material parameter. Variable-temperature PL experiments simulated by Gaussian lineshape analysis and a modified Arrhenius model allow us to consistently resolve the contribution of three emissive recombination channels in the CQDs. Transient PL and absorption indicate that the channels exhibit also distinct dynamical characteristics that are influenced by confinement and temperature. Based on the evidence on the energetics and dynamics of such photoexcitations, we assigned the luminescence channels to optical transitions from the conduction band edge to: (i) self-trapped hole states and (ii) valence band holes, (iii) holes in higher lying valence band states. The role of surface states as QD-size dependent trapping/detrapping sites of excitons was also highlighted. Furthermore preliminary theoretical calculations appear to further support the model, providing matching of the energy position of the two observed electronic transitions with features present in the transient absorption bleaching curve of the CQDs.

6 Conclusions

This thesis contains studies of three types of multinary chalcogenide semiconductor nanostructures that are promising for optoelectronics.

In particular, in Chapter 3, the optical properties of solutions and films of CIS QDs passivated by Zn were studied. Based on the evidence provided by the steady-state and time-resolved photoluminescence, we interpreted the lower energy emission to donor-acceptor pairs that are populated via relaxation from band-edge states, while the high energy PL contribution, appears to originate from excitations slightly below the band-edge; such excitations are tentatively assigned to a free to bound type of transition, most probably from the conduction band to localized holes below the valence band edge.

In Chapter 4, a spectroscopic investigation of PLD-deposited CIGS films as well as a preliminary study of PLD-grown CdS was performed. For CIGS, the work focused on studies of the influence of PLD deposition temperature on the emission properties. Based on the evidence provided by the temperature steady-state and time-resolved experiments in combination with Gaussian lineshape analysis the high energy peak appears to be associated with electronic levels while two lower energy PL channels with defect CIGS levels. A fourth emissive channel observed at lower PLD-temperatures has been assigned to a $Cu_{2-x}Se$ secondary crystal phase evidenced by XRD experiments. For CdS,. polycrystalline and stoichiometric films with relatively large crystallites were obtained at PLD deposition temperatures of 200–400 °C. Within the same PLD temperature range a consistent increase of the integrated PL and the PL lifetime is observed, witnessing the improvement of the structural film properties.

In Chapter 5, a photophysical investigation of colloids and films of $Ag_3In_5Se_9$ NCs was studied, using the QD size as the adjustable material parameter. Three recombination channels with distinct energetic and dynamic characteristics that are influenced by confinement and temperature were observed using Gaussian lineshape analysis. Based on evidence by variable temperature and transient absorption and luminescence experiments, the channels have been assigned in descending energy to radiative transitions from the conduction band edge to: (i) self-trapped hole states and (ii) valence band holes, (iii) holes in higher lying valence band states. The spectroscopic characterization provides also evidence of shallow surface states acting as

sites in which fast exciton trapping and much slow de-trapping occurs, with the rates being influenced by QD confinement and sample temperature.

7 Bibliography

[1]   M. Fox, Optical Properties of Solids, Oxford University Press, 2001

[2]   D. V. Talapin, J. - S. Lee, M. V. Kovalenko, E. V. Shevchenko, Prospects of Colloidal Nanocrystals for Electronic and Optoelectronic Applications, Chem. Rev., 2010, 110, 389-45

[3]   N. H. Kim, J. Jeong, H. Chae, White Light Emission with Quantum Dots: A Review, Applied Science and Convergence Technology, 2016, 25, 1-6

[4]   D. S. Kumar, B. J. Kumar, H. M. Mahesh, Chapter 3 - Quantum Nanostructures (QDs): An Overview, Synthesis of Inorganic Nanomaterials, 2018, 59-88

[5]   V. K. LaMer, R. H. Dinegar, Theory, Production and Mechanism of Formation of Monodispersed Hydrosols, J. Am. Chem. Soc., 1950, 72, 4847–4854

[6]   C. B. Murray, C. R. Kagan, M. G. Bawendi, Synthesis and Characterization of Monodisperse Nanocrystals and Close-Packed Nanocrystal Assemblies, Annual Review of Materials Science, 2000, 30, 545-610

[7]   K. Rajan, I. Roppolo, A. Chiappone, S. Bocchini, D. Perrone, A. Chiolerio, Silver nanoparticle ink technology: state of the art, Nanotechnol Sci Appl., 2016, 9, 1–13.

[8]   M. R. P. I. Jayawardhana , K. A. I. L. Wijewardena Gamalath, Electronic structures of CdSe quantum dots embedded in ZnSe, World Scientific News, 2017, 86, 205-225

[9]   S. V. Gaponenko, Optical Properties of Semiconductor Nanocrystals, Cambridge University Press, 1988, 5-8

[10] L. Brus, Electronic Wave Functions In Semiconductor Clusters: Experiment and Theory, The Journal of Physical Chemistry, 1986, 90, 2555-2560

[11] Y. Kayanuma, T. Uozumi, K. Yamanaka, K. Edamatsu, T. Itoh., Excited-state absorption of excitons confined in spherical quantum dots, Physical Review B, 1999, 59

[12] H. M. Shmidt, H. Weller., Quantum size effects in semiconductor crystallites: Calculation of the energy spectrum for the confined exciton, Chemical Physics Letters, 1986, 129, 615-618

[13] J. I. Pankove, Optical processes in semiconductors, Dover Publications Inc., 1971, Book

[14] S. T. Teklemichael, M. D. McCluskey, Acceptor and surface states of ZnO nanocrystals: A unified model, Nanotechnology, 2011, 22

[15] X. Zhang,T. Wang, W. Chen, S. Wang, D. Peng, Edge-Corrected Mean-Field Hubbard Model: Principle and Applications in 2D Materials, Front. Phys., 2017, 5

[16] D. Broberg, B. Medasani, N. E. R. Zimmermann, G. Yu, A. Canning, M. Haranczyk, M Asta, G. Hautier, PyCDT: A Python toolkit for modeling point defects in semiconductors and insulators, Computer Physics Communications, 2018, 226, 165-179

[17] A. Axelevitch, G. Golan, Efficiency analysis for multi-junction PV hetero-structures, Research Letters in Materials Science, 2010, 4

[18] Y. Diao, L. Shaw, Z. Bao, S. C. B. Mannsfeld, Morphology control strategies for solution-processed organic semiconductor thin films, energy environ. Sci., 2014, 7, 2145-2159

[19] R. Das, A. Chanda, Fabrication and Properties of Spin-Coated Polymer Films, Nano-size Polymers, 2016, 283-306 , Book

[20] N. Sahu, B. Parija, S. Panigrahi, Fundamental understanding and modeling of spin coating process : A review, Indian J. Phys., 2009, 83, 493-502

[21] P. Kajal, K. Ghosh, S. Powar, Manufacturing Techniques of Perovskite Solar Cells, Applications of Solar Energy, 2018, 341-364

[22] C. Nicolaou, A. Zacharia, G. Itskos, J. Giapintzakis, Influence of process parameters on the properties of pulsed laser deposited $CuIn_{0.7}Ga_{0.3}Se_2$ thin films, Sol. Energy, 2018, 174, 793–802

[23] J. Schou, Physical aspects of the pulsed laser deposition technique: The stoichiometric transfer of material from target to film, Appl. Surf. Sci., 2009, 255, 5191-5198

[24] S.Amoruso, Chapter 6, Plume characterization in pulsed laser deposition of metal oxide thin films, Metal Oxide-Based Thin Film Structures, 2018, 133-160

[25] J. Mittra, G. J. Abraham, M. Kesaria, S. Bahl, A. Gupta, S. M. Shivaprasad, C. S. Viswanadham, U. D. Kulkarni, G. K. Dey, Role of Substrate Temperature in the Pulsed Laser Deposition of Zirconium Oxide Thin Film, Materials Science Forum, 2012, 710, 757-761

[26] M. Bizarro, S. E. Rodil, Physicochemical Characterization of Photocatalytic Materials, Photocatalytic Semiconductors, 2014, 103-153, Book

[27] LAMBDA 850/950/1050 UV/Vis and UV/Vis/NIR Spectrophotometers, Manual

[28] Fluorolog-3, Operation Manual, rev. G, 2014

[29] Time-Resolved Fluorescence Technical Note TRFT-4, Horiba, Manual

[30] C.-W. Luo, Y.-T. Wang, A. Yabushita, T. Kobayashi, Ultrabroadband time-resolved spectroscopy in novel types of condensed matter, Optical Society of America, 2016, 3, 82-92

[31] A. C. Berends, M. J. J. Mangnus, C. Xia, F. T. Rabouw, D. de M. Donega, Optoelectronic Properties of Ternary I−III−VI$_2$ Semiconductor Nanocrystals: Bright Prospects with Elusive Origins, J. Phys. Chem. Lett., 2019, 10, 1600-1616

[32] A. D. P. Leach, J. E. Macdonald, Optoelectronic Properties of CuInS$_2$ Nanocrystals and Their Origin, J. Phys. Chem. Lett, 2016, 7, 572–583

[33] D. So, G. Konstantatos, Thiol-free Synthesized Copper Indium Sulfide Nanocrystals as Optoelectronic Quantum Dot Solids, Chem. Mater, 2015, 27, 8424-8432

[34] Y. Vahidshad, M. N. Tahir, A. I. Zad, S. M. Mirkazemi, R. Ghazemzadeh, W. Tremel, Structural and optical properties of Fe and Zn substituted CuInS$_2$ nanoparticles synthesized by a one-pot facile method, J. Mater. Chem. C, 2015, 3, 889-898

[35] H. Zhong, S. S. Lo, T. Mirkovic, Y. Li, Y. Ding, Y. Li, G. D. Scholes, Noninjection Gram-Scale Synthesis of Monodisperse Pyramidal CuInS$_2$ Nanocrystals and Their Size-Dependent Properties, ACS Nano 2010, 4, 5253-5262

[36] J. Kolny-Olesiak, H. Weller, Synthesis and Application of Colloidal CuInS$_2$ Semiconductor Nanocrystals, ACS Appl. Mater, 2013, 5, 12221−12237

[37] L. Wang, Z. Guan, A. Tang, Multinary copper-based chalcogenide semiconductor nanocrystals: synthesis and applications in light-emitting diodes and bioimaging, Journal of Nanoparticle Research, 2020, 22

[38] H. Zhong, Y. Zhou, M. Ye, Y. He, J. Ye, C. He, C. Yang, Y. Li, Controlled Synthesis and Optical Properties of Colloidal Ternary Chalcogenide CuInS$_2$ Nanocrystals, Chem. Mater, 2008, 20, 6434–6443

[39] K. E. Knowles, K. H. Hartstein, T. B. Kilburn, A. Marchioro, H. D. Nelson, P. J. Whitham, D. R. Gamelin, Luminescent Colloidal Semiconductor Nanocrystals Containing Copper: Synthesis, Photophysics, and Applications, Chem. Rev., 2016, 116, 10820–10851

[40] A. Shabaev, M. J. Mehl, and Al. L. Efros, Energy band structure of CuInS$_2$ and optical spectra of CuInS$_2$ nanocrystals, Phys. Rev. B, 2015, 92

[41] L. De Trizio, M. Prato, A. Genovese, A. Casu, M. Povia, R. Simonutti, M. J. Alcocer, C. D'Andrea, F. Tassone and L. Manna, Fluorescent Quaternary Cu−In−Zn−S Nanocrystals Prepared from Cu$_{1-x}$InS$_2$ Nanocrystals by Partial Cation Exchange, Chem. Mater., 2012, 24, 2400−2406

[42] O. Stroyuk, V. Dzhagan, A. Raevskaya, F. Spranger, N. Gaponik, D. R. T. Zahn, Insights into different photoluminescence mechanisms of binary and ternary aqueous nanocrystals from the temperature dependence: A case study of CdSe and Ag-In-S. Journal of Luminescence, 2019, 215

[43] K. Kishigui, K. Abe, G. Murakami, Y. Shim, K. Yoshino, K. Wakita, Study of steady-state photoluminescence of AgInSe$_2$ crystals. Thin Solid Films 2008, 517, 1445-1448

[44] H. C. Woo, J. W. Choi, J. Shin, S. H. Chin, M. H. Ann, C. L. Lee, Temperature-Dependent Photoluminescence of CH$_3$NH$_3$PbBr$_3$ Perovskite Quantum Dots and Bulk Counterparts. J. Phys. Chem. Lett., 2018, 9, 4066

[45] G. Morello, M. De Giorgi, S. Kudera, L. Manna, R. Cingolani, M. Anni, Temperature and Size Dependence of Nonradiative Relaxation and Exciton-Phonon Coupling in Colloidal CdTe Quantum Dots. J. Phys. Chem. C, 2007, 111, 5846-5849

[46] D. Haneman, Properties and applications of copper indium diselenide, Critical Reviews in Solid State and Material Sciences, 1988, 14, 387

[47] J. Seo, S. Raut, M. Abdel-Fattah, Q. Rice, B. Tabibi, R. Rich, R. Fudala, I. Gryczynski, Z. Gryczynski, W.-J. Kim, S. Jung, R. Hyun, Time-resolved and temperature-dependent photoluminescence of ternary and quaternary nanocrystals of CuInS$_2$ with ZnS capping and cation exchange, JOURNAL OF APPLIED PHYSICS, 2013, 114

[48] A. Zacharia, C. Nicholaou. J. Giapintzakis, G. Itskos, Luminescence properties of pulsed laser deposited CuIn$_x$Ga$_{1-x}$Se$_2$, Journal of Physics Communications, 2020,4

[49] H. Sim, J. M. Lee, S. Cho, E. – S. Cho, S. J. Kwon, A Study on the Band Structure of ZnO/CdS Heterojunction for CIGS Solar-Cell Application, Journal of semiconductor technology and science, 2015, 15, 267-275

[50] M. Asaduzzaman, A. N. Bahar, M. M. R. Bhuiyan, Dataset Demonstrating the Modeling of a High Performance Cu(In,Ga)Se$_2$ Absorber Based Thin Film Photovoltaic Cell, Data in Brief, 2017,11, 296-300

[51] Y. Zhang, H. Jun, J. Y. Park, S. Y. Park, S. O. Ryu, S. O. Ryu, Deposition and Characterization of CIGS Thin Films Deposited by Chemical Spray Process, Molecular Crystals and Liquid Crystals, 2015, 617, 186-194

[52] H. T. Xue, W. J. Lu, F. L. Tang, X. K. Li, Y. Zhang, Y. D. Feng, Phase diagram of the CuInSe$_2$-CuGaSe$_2$ pseudobinary system studied by combined ab initio density functional theory and thermodynamic calculation, Journal of Applied Physics, 2014 116

[53] M. G. Tsai, H. T. Tung, I. -G. Chen, C. C. Chen, Y. F. Wu, X. -D. Qi, Y. Hwu, C. Lin, P. H. Wu, C. – W. Cheng, Annealing Effect on the Properties of Cu(In$_{0.7}$Ga$_{0.3}$)Se$_2$ Thin Films Grown by Femtosecond Pulsed Laser Deposition, Journal of the American Ceramic Society, 2013, 96, 2419–2423

[54] Y. H. Jo, B. C. Mohanty, Y. S. Cho, Enhancedelectrical properties of pulsed laser-deposited CuIn$_{0.7}$Ga$_{0.3}$Se$_2$ thin films via processing control, Solar Energy, 2010, 84, 2213–2218

[55] T. J. Whittles, T. D. Veal, C. N. Savory, A. W. Welch, F. W. de S. Lucas, J. T. Gibbon, M. Birkett, R. J. Potter, D. O. Scanlon, A. Zakutayev, V. R. Dhanak, Core Levels, Band Alignments, and Valence-Band States in CuSbS$_2$ for Solar Cell Applications, ACS Appl. Mater. Interfaces, 2017, 9, 41916−41926

[56] S.-C. Chen, D.-H. Hsieh, H. Jiang, Y.-K. Liao, F.-I. Lai, C. - H. Chen, C. W. Luo, J. – Y. Juang, Y. – L. Chueh, K. – H. Wu, H. – C. Kuo, Growth and characterization of Cu(In,Ga)Se$_2$ thin films by nanosecond and femtosecond pulsed laser deposition, 2014, 9

[57] R. Bacewicz, P. Zuk, R. Trykozko, Photoluminescence study of ZnO/CdS/Cu(In,Ga)Se$_2$ sollar cells, Opto-electronics review, 2003, 11, 277-280

[58] J. Yang, D. S. Chen, F. Xu, Z. Q. Ma, Photoluminescence study of the defect-induced recombination in Cu(In,Ga)Se$_2$ solar cell, Solar Energy, 2013, 98, 415-421

[59] Y. - K. Liao, S. - Y. Kuo, W. - T. Lin, F. - I. Lai, D. - H. Hsieh, M. - A. Tsai, S. - C. Chen, D. - W. Chiou, J. - C. Chang, K. - H. Wu, S. - J. Cheng, H. - C. Kuo, Observation of unusual optical transitions in thin-film Cu(In,Ga)Se$_2$ solar cells, Optics Express, 2012, 20, A836-A842

[60] J. Ramanujam, U. P. Singh, Copper indium gallium selenide based solar cells - a review, Energy Environ. Sci., 2017, 10, 1306-1319

[61] T. D. Lee, A. U. Ebong, A Review of thin film solar cell technologies and challenges, Renew. Sustain. Energy Rev., 2017, 70, 1286–97

[62] Solar Frontier Achieves World Record Thin-Film Solar Cell Efficiency of 22.9%, SolarFrontier, 2017, (http://solar-frontier.com/eng/ news/2017/1220_press.html)

[63] M. Marudachalam, R. W. Birkmire, H. Hichri, Phases, morphology, and diffusion in $CuIn_xGa_{1-x}Se_2$ thin films, J. Appl. Phys., 1997, 82, 2896-2905

[64] J. A. Frantz, R. Y. Bekele, V. Q. Nguyen, J. S. Sanghera, A. Bruce, S. V. Frolov, M. Cyrus, I. D. Aggarwal, $Cu(In,Ga)Se_2$ thin films and devices sputtered from a single target without additional selenization, Thin Solid Films, 2011, 519, 7763-7765

[65] A. Javed, Preparation and Study of the Structural, Optical and Electrical Properties of $Cu(In,Ga)Se_2$ Thin Films, Turk J Phys, 2007, 31, 287 – 294

[66] C. – C. Chen, X. Qi, W. – C. Chang, M. – G. Tsai, I. – G. Chen, C. – Y. Lin, P. – H. Wu, K. – P. Chang, The effects of pulse repetition rate on the structural, optical, andelectrical properties of CIGS films grown by pulsed laser deposition, Applied Surface Science, 2015, 351, 772–778

[67] G. H. Bauer, R. Brüggemann, S. Tardon, S. Vignoli, R. Kniese, Quasi-Fermi level splitting and identification of recombination losses from room temperature luminescence in $Cu(In_{1-x}Ga_x)Se_2$ thin films versus optical band gap, Thin Solid Films, 2005, 480-481, 410-414

[68] C. Sima, O. Toma, Influence of temperature on the $CuIn_{1-x}Ga_xSe_2$ films deposited by picosecond laser ablation, Appl. Surf. Sci., 2017, 425, 1028–1032

[69] S. Theodoropoulou, D. Papadimitriou, A. Mamalis, D. Manolakos, R. Klenk, M. – Ch. Lux – Steiner, Band-gap energies and strain effects in $CuIn_{1-x}Ga_xS_2$ based solar cells, Semicond. Sci. Technol., 2007, 22, 933

[70] S. Siebentritt, M. Igalson, C. Persson, S. Lany, The electronic structure of chalcopyrites— bands,point defects and grain Boundaries, Prog. Photovolt: Res. Appl., 2010, 18, 390–410

[71] J. Yang, H. W. Du, Y. Li, M. Gao, Y. Z. Wan, F. Xu, Z. Q. Ma, Structural defects and recombination behavior of excited carriers in $Cu(In,Ga)Se_2$ solar cells, AIP Adv., 2016, 6

[72] A. Ghosh, C. Kulsi, D. Banerjee, A. Mondal, Galvanic synthesis of $Cu_{2-x}Se$ thin films and their photocatalytic and thermoelectric Properties, Appl. Surf. Sci., 2016, 369, 525–534

[73] M. Maiberg, T. Hölscher, S. Zahedi-Azad, W. Franzel, R. Scheer, Investigation of long lifetimes in $Cu(In,Ga)Se_2$ by time-resolved photoluminescence, Appl. Phys. Lett., 2015, 107

[74] S. – I. Shimakawa, K. Kitani, S. Hayashi, T. Satoh, Y. Hashimoto, Y. Takahashi, T. Negami, Characterization of $Cu(In,Ga)Se_2$ thin films by time-resolved photoluminescence, Phys. Stat. Sol. (a), 2006, 203, 2630-2633

[75] P. Papagiorgis, A. Stavrinadis, A. Othonos, G. Konstantatos, G. Itskos, The Influence of doping on the optoelectronic properties of PbS colloidal quantum dot solids, Sci. Rep., 2016, 6

[76] M. Maiberg, T. Hölscher, E. Jarzembowski, S. Hartnauer, S. Zahedi-Azad, W. Fränzel, R. Scheer, Verification of minority carrier traps in $Cu(In,Ga)Se_2$ and $Cu_2ZnSnSe_4$ by means of time-resolved photoluminescence, Thin Solid Films, 2017, 633, 208-212

[77] K.-N. Tu, J. W. Mayer, L. C. Feldman, Electronic Thin Film Science for Electrical Engineers and Materials Scientists, 1992, 101-102

[78] Christiana Nicolaou, Anna Zacharia, Andreas Delimitis, Grigorios Itskos, John Giapintzakis, Single-step growth of high quality CIGS/CdS heterojunctions using Pulsed Laser Deposition, Applied Surface Science, 2020, 511

[79] S. Pandya, K. Raval, Investigation of structural, morphological and optical properties of cadmium sulphide (CdS) thin films at different Cd/S concentration deposited by chemical technique, J. Mater. Sci.: Mater. Electron., 2017, 28, 18031–18039

[80] M. N. Ashfold, F. Claeyssens, G. M. Fuge, S. J. Henley, Pulsed laser ablation and deposition of thin films, Chem. Soc. Rev., 2004, 33, 23–31

[81] S. Yu, L. Ding, C. Xue, L. Chen, W. Zhang, Transparent conducting Sb-doped SnO_2 thin films grown by pulsed laser deposition, J. Non-Cryst. Solids, 2012, 358, 3137–3140

[82] J. - L. Zhao, X. - M. Li, J. - M. Bian, W. - D. Yu, X. - D. Gao, Structural, optical and electrical properties of ZnO films grown by pulsed laser deposition (PLD), J. Cryst. Growth, 2005, 276, 507–512

[83] Z. Zhang, F. Zhou, X. Wei, M. Liu, G. Sun, C. Chen, C. Xue, H. Zhuang, B. Man, Effects of oxygen pressures on pulsed laser deposition of ZnO films, Phys. E: Lowdimensional Syst. Nanostruct., 2007, 39, 253–257

[84] L. Sun, J. He, Y. Chen, F. Yue, P. Yang, J. Chu, Comparative study on Cu_2ZnSnS_4 thin films deposited by sputtering and pulsed laser deposition from a single quaternary sulfide target, J. Cryst. Growth, 2012, 361, 147–151

[85] S. Vanalakar, G. Agawane, S. W. Shin, M. Suryawanshi, K. Gurav, K. Jeon, P. Patil, C. Jeong, J. Kim, J. Kim, A review on pulsed laser deposited CZTS thin films for solar cell applications, J. Alloy. Compd., 2015, 619, 109–121

[86] G. Perna, V. Capozzi, M. Ambrico, V. Augelli, T. Ligonzo, A. Minafra, L. Schiavulli, M. Pallara, Structural and optical characterization of undoped and indium-doped CdS films grown by pulsed laser deposition, Thin Solid Films, 2004, 453, 187–194

[87] J. - C. Orlianges, C. Champeaux, P. Dutheil, A. Catherinot, T. M. Mejean, Structural, electrical and optical properties of carbon-doped CdS thin films prepared by pulsed laser deposition, Thin Solid Films, 2011, 519, 7611–7614

[88] K. Acharya, J. Skuza, R. Lukaszew, C. Liyanage, B. Ullrich, CdS thin films formed on flexible plastic substrates by pulsed-laser deposition, J. Phys.: Condens. Matter, 2007, 19

[89] M. Arif, Siddhartha, Z. R. Khan, V. Gupta, A. Singh, Effect of substrates temperature on structural and optical properties of thermally evaporated CdS nanocrystalline thin films, 2014, 52, 699-703

[90] J. K. Cooper, J. Cao, J. Z. Zhang, Exciton dynamics of CdS thin films produced by chemical bath deposition and DC pulse sputtering, ACS Appl. Mater. Interfaces, 2013, 5, 7544–7551

[91] O. Yarema, M. Yarema, D. Bozyigit, W. M. M Lin, V. Wood, Independent Composition and Size Control for Highly Luminescent Indium-Rich Silver Indium Selenide Nanocrystals, ACS Nano., 2015, 9, 11134-11142

[92] M. A. Langevin, A. M. Ritcey, C. N. Allen, Air-Stable Near-Infrared $AgInSe_2$ Nanocrystals, ACS Nano., 2014, 8, 3476-3482

[93] D. Deng, L. Qua, Y. Gu, Near-infrared broadly emissive $AgInSe_2$/ZnS quantum dots for biomedical optical imaging, J. Mater. Chem. C, 2014, 2, 7077-7085

[94] S. P. Hong, H. K. Park, J. H. Oh, H. Yang, Y. R. Do, Comparisons of the Structural and Optical Properties of o-$AgInS_2$, t-$AgInS_2$, and c-$AgIn_5S_8$ Nanocrystals and Their Solid-Solution Nanocrystals with ZnS, J. Mater. Chem., 2012, 22, 18939-18949

[95] R. Xie, M. Rutherford, X. Peng, Formation of High-Quality IIIIVI Semiconductor Nanocrystals by Tuning Relative Reactivity of Cationic Precursors, J. Am. Chem. Soc., 2009, 131, 5691-5697

[96] P. M. Allen, M. G. Bawendi, Ternary IIIIVI Quantum Dots Luminescent in the Red to Near-Infrared, J. Am. Chem. Soc., 2008, 130, 9240-9241

[97] T. Bai, C. Li, F. Li, L. Zhao, Z. Wang, H. Huang, C. Chen, Y. Han, Z. Shi, S. Fenga, A simple solution-phase approach to synthesize high quality ternary $AgInSe_2$ and band gap tunable quaternary $AgIn(S_{1-x}Se_x)_2$ nanocrystals, Nanoscale, 2014, 6, 6782-6789

[98] M. Yarema, S. Pichler, M. Sytnyk, R. Seyrkammer, R. T. Lechner, G. Fritz-Popovski, D. Jarzab, K. Szendrei, R. Resel, O. Korovyanko, M. A. Loi, O. Paris, G. Hesser, W. Heiss, W, Infrared

Emitting and Photoconducting Colloidal Silver Chalcogenide Nanocrystal Quantum Dots from a Silylamide-Promoted Synthesis, ACS Nano., 2011, 5, 3758-3765

[99] T. Kameyama, Y. Douke, H. Shibakawa, M. Kawaraya, H. Segawa, S. Kuwabata, T. W. Torimoto, Controllable Electronic Energy Structure of ZnSeAgInSe$_2$ Solid Solution Nanocrystals for Quantum-Dot-Sensitized Solar Cells, J. Phys. Chem. C, 2014, 118, 29517-29524

[100] D. Pathak, R. K. Bedi, D. Kaur, Characterization of AgInSe$_2$ Films Deposited by Hot-Wall Vacuum Evaporation Method, Materials and Manufacturing Processes, 2010, 25, 1012–1017

[101] D. Aldakov, A. Lefrançois, P. Reiss, Ternary and quaternary metal chalcogenide nanocrystals: synthesis, properties and applications, J. Mater. Chem. C, 2013, 24, 3756–3776

[102] D. Pathak, R. K. Bedi, D. Kaur, Effect of Substrate Temperature on the Structural, Optical, and Electrical Properties of Silver-indium-selenide Films Prepared by Using Laser Ablation, Journal of the Korean Physical Society, 2010, 56, 836-841

[103] Atti Della Fondazione Giorgio Ronchi Anno LXIV N.5 Book, p. 717

[104] P. P. Martin, J. Lyding, A. Rockett, Scanning tunneling spectroscopy of epitaxial silver indium diselenide, Surface Science, 2015, 636, 8-12

[105] D. Yao, H. Liu, Y. Liu, C. Dong, K. Zhang, Y. Sheng, J. Cui, H. Zhang, B. Yang, Phosphine-free synthesis of Ag–In–Se alloy nanocrystals with visible emissions, Nanoscale, 2015, 7, 18570-18578

[106] O. Yarema, M. Yarema, V. Wood, Tuning the Composition of Multicomponent Semiconductor Nanocrystals: The Case of I−III−VI Materials, Chem. Mater., 2018, 30, 1446-1461

[107] Y. J. Park, J. H. Oh, N. S. Han, H. C. Yoon, S. M. Park, Y. R. Do, J. K. Song, Photoluminescence of Band Gap States in AgInS$_2$ Nanoparticles, The Journal of Physical Chemistry C, 2014, 118, 25677-25683

[108] L. Li, A. Pandey, D. J. Werder, B. P. Khanal, J. M. Pietryga, V. I. Klimov, Efficient Synthesis of Highly Luminescent Copper Indium Sulfide-Based Core/Shell Nanocrystals with Surprisingly Long-Lived Emission, J. Am. Chem. Soc., 2011, 133, 1176−11

[109] Y. Hamanaka, T. Ogawa, M. Tsuzuki, T. Kuzuya, Photoluminescence Properties and Its Origin of AgInS$_2$ Quantum Dots with Chalcopyrite Structure, J. Phys. Chem. C, 2011, 115, 1786–1792

[110] M. Luisier, A. Schenk, W. Fichtner, G. Klimeck, Atomistic simulation of nanowires in the sp^3d^5s* tight-binding formalism: from boundary conditions to strain calculations. Phys. Rev. B, 2006, 74